

EMBRY-RIDDLE

Aeronautical University™

SCHOLARLY COMMONS

Publications


8-2003

Computational Models for Diffusion of Second Messengers in Visual Transduction

Harihar Khanal

The University of Tennessee, Knoxville, khana66a@erau.edu

Follow this and additional works at: <https://commons.erau.edu/publication>

 Part of the [Medical Biochemistry Commons](#), [Numerical Analysis and Computation Commons](#), and the [Partial Differential Equations Commons](#)

Scholarly Commons Citation

Khanal, H. (2003). Computational Models for Diffusion of Second Messengers in Visual Transduction. , (). Retrieved from <https://commons.erau.edu/publication/817>

This Dissertation is brought to you for free and open access by Scholarly Commons. It has been accepted for inclusion in Publications by an authorized administrator of Scholarly Commons. For more information, please contact commons@erau.edu.

To the Graduate Council:

I am submitting herewith a dissertation written by Harihar Khanal entitled "Computational Models for Division of Second Messengers in Visual Transduction." I have examined the final electronic copy of this dissertation for form and content and recommend that it be accepted in partial fulfillment of the requirements for the degree of Doctor of Philosophy, with a major in Mathematics.

Vasilios Alexiades, Major Professor

We have read this dissertation and recommend its acceptance:

Ohannes Karakashian, Charles Collins, Solon Georghiou

Accepted for the Council:

Dixie L. Thompson

Vice Provost and Dean of the Graduate School

(Original signatures are on file with official student records.)

To the Graduate Council:

I am submitting herewith a dissertation written by Harihar Khanal entitled “ Computational models for diffusion of second messengers in visual transduction”. I have examined the final electronic copy of this dissertation for form and content and recommend that it be accepted in partial fulfillment of the requirements for the degree of Doctor of Philosophy, with a major in Mathematics.

Vasilios Alexiades

Major Professor

We have read this dissertation
and recommend its acceptance:

Ohannes Karakashian

Charles Collins

Solon Georghiou

Accepted for the Council:

Dr. Anne Mayhew

Vice Provost and Dean of
Graduate Studies

Original signatures are on file with official student records.

Computational Models for Diffusion of Second Messengers in Visual Transduction

A Dissertation
Presented for the
Doctor of Philosophy
Degree
The University of Tennessee, Knoxville

Harihar Khanal
August 2003

Dedication

This dissertation is dedicated to my respected brother

Mr. Babu Ram Khanal

who lost his eye sight at the age of 32 years

due to Retinitis Pigmentosa.

Acknowledgements

I would like to express my most sincere gratitude to my advisor, Professor Vasilios Alexiades for many stimulating discussions, for his guidance, time and patience. His clear and sharp intellect have helped me to appreciate more fully the rich interaction between mathematics and computations.

I would also like to thank my Dissertation Committee: Professor Charles Collins, Professor Ohannes Karakashian, and Professor Solon Georghiou for their assistance and advice.

Thanks are also given to Prof. E. Benedetto (Department of Mathematics, Vanderbilt University) and Prof. H. Hamm (Department of Pharmacology, Medical Center, Vanderbilt University) for their helpful suggestions.

I sincerely thank the concerned authorities at the Oak Ridge National Laboratory, Oak Ridge, Tennessee, for providing access to the IBM pSeries cluster computer to perform all the computations.

I would also like to thank the concerned authorities at the Tribhuban University, Kathmandu, Nepal for providing me a long study leave to complete my degree.

Finally, I wish to express my deep sense of gratitude to my wife and my family members for their inspiration and moral support.

Abstract

The process of phototransduction, whereby light is converted into an electrical response in retinal rod and cone photoreceptors, involves, as a crucial step, the diffusion of cytoplasmic signaling molecules, termed **second messengers**. A barrier to mathematical and computational modeling is the complex geometry of the rod outer segment which contains about 1000 thin discs. Most current investigations on the subject assume a well-stirred bulk aqueous environment thereby avoiding such geometrical complexity. We present theoretical and computational spatio-temporal models for phototransduction in vertebrate rod photoreceptors, which are pointwise in nature and thus take into account the complex geometry of the rod outer segment. We consider both the full model and two forms (strong and weak) of a homogenized limit model which involves simplified geometry. These, spatially resolved, models reduce to simpler (longitudinal and lumped) models proposed by physiologists. We establish well-posedness of the model problems using upper and lower solutions and their associated monotone iterations. Computational models of the mathematical problems have been developed, based on Finite Volume discretization of the partial differential equations and boundary conditions, and implemented in Fortran. Convergence of the finite difference system to the solution of the continuous problem for a similar problem is shown in [41]. Due to the intricate geometry of the cytosol, the

full model involves very intensive computations. This is achieved via parallelization for distributed memory clusters of processors. The homogenized limit problem is also tested and the computational model based on its **weak** form is found to produce qualitatively similar results as from the full model. We also tested a spatially adaptive mesh for the homogenized problem and numerical experiments convinced us that we could get the same qualitative solutions with much less computational effort. Numerical experiments are presented, simulating the single photon response for **salamander**, with certain activation parameters chosen to produce the experimental 0.8% peak suppression of dark current, kindly communicated by Fred Rieke [45]. The model exhibits highly localized response about the activation site, with longitudinal spread of about 172 discs out of 800 discs. The radial profiles of cGMP become progressively steeper during activation and recede back during recovery. Thus radial diffusion is not negligible.

Contents

1	Introduction	1
2	Mathematical Models	5
2.1	Phototransduction Process	5
2.2	Geometry of the Domain	7
2.3	Basic Equations of Diffusion with Interaction	9
2.4	Simpler Models	14
2.4.1	1D Longitudinal Model	14
2.4.2	Bulk (ODE) Model	15
2.5	Activation Models	16
2.5.1	Activation by a Gaussian	17
2.5.2	Activation via a Lumped Model	17
2.6	Homogenized Limit Problem	19
2.7	Undimensionalization	22
2.7.1	Full Model	22
2.7.2	1D Longitudinal Model	24
2.7.3	Homogenized Model	25
2.7.4	Homogenized Model in Weak Form	27

2.8	Well-posedness of the Model Problems	28
3	Finite Volume Models	35
3.1	Full Model	36
3.1.1	Discretization of the PDEs	37
3.1.2	Discretization of the Boundary Conditions	40
3.1.3	Explicit-Implicit Method	42
3.1.4	1D Longitudinal Model	44
3.2	Homogenized Model	46
3.2.1	Discretization Based on PDEs	47
3.2.2	Discretization Based on the Weak Form	56
3.3	Stability	68
3.4	Convergence	70
3.4.1	The Finite Difference System	70
3.4.2	Construction of Monotone Iterative Scheme	72
3.4.3	Convergence of Finite Difference Solutions	73
3.5	Parallelization via Domain Decomposition	74
3.5.1	Speedup	75
3.5.2	Efficiency	77
3.5.3	Runtime Tests	77
4	Numerical Simulations	81
4.1	Choosing Parameters and Scales	82
4.1.1	Parameters	82
4.1.2	Dark Steady-State	86
4.1.3	PDE Activation - Setting the Light Source	87

4.1.4	Choice of Time and Space Scales	90
4.2	Validation of the Models	93
4.2.1	Experiment to be Simulated	93
4.2.2	Simulations	94
5	Results and Discussion	95
5.1	Single Photon Response	95
5.1.1	Results from the Full Model	96
5.1.2	Results from Other Models	102
5.2	Higher Intensity Stimulus	108
5.3	Conclusions	110
5.4	Further Directions	112
	Bibliography	113
	Vita	120

List of Tables

2.1	Nomenclature	8
3.1	Speedup and Efficiency on colt with 100 discs	78
3.2	Speedup and Efficiency on various machines with 200 discs	78
3.3	Speedup and Efficiency on various machines with 400 discs	78
4.1	Parameters of the model (for salamander rod)	83
5.1	Spread of single photon response in various species	110

List of Figures

1.1	The photoreceptor retinal rod cells, from [44]	2
2.1	The geometry of cytosol for the full model	10
2.2	The simplified geometry for the homogenized problem	19
3.1	Finite volume (r, z) mesh	38
3.2	Parallel implementation scheme	75
3.3	Speedup and CPU time (on colt) for 100, 200 and 400 discs.	80
4.1	Activated rhodopsin and PDE molecules versus time	90
5.1	Single photon response from the full model: histories of response and normalized response	98
5.2	Single photon response from the full model: histories of concentrations of cGMP and Ca^{2+} at a fixed location in the cytosol in the vicinity of the activated disc.	99
5.3	Single photon response from the full model: z -profiles of the depletion of relative concentrations at various times	100
5.4	Single photon response from the full model: z -profiles of (local) relative response and r -profiles of Ca^{2+} concentration at various times	101

5.5	Single photon response from the full model: radial profiles of cGMP concentration	102
5.6	Bulk model simulation: normalized response versus time	103
5.7	Longitudinal model simulation: normalized response versus time . . .	104
5.8	Normalized response from homogenized model and full model	105
5.9	Longitudinal spread of cGMP and Ca ²⁺ concentrations from homogenized model and full model, at times 100, 200, 400 and 1000 ms . . .	105
5.10	Histories of the normalized response from all models	106
5.11	Histories of cGMP concentration (at activated disc) from all models .	107
5.12	Histories of Ca ²⁺ concentration (at activated disc) from all models . .	107
5.13	Bulk model simulations reproducing Fig. 10, p.234 of Pugh-Lamb [44]	108
5.14	Longitudinal spread and histories of normalized responses with different arrangement of activation sites for $\Phi = 52$ photoisomerizations . .	109

Chapter 1

Introduction

We are able to see because photoreceptors in the eye convert (transduce) light into electrical signals and send to the brain. When the conversion fails, as it does in hereditary retinal degenerations, a willing brain is left unable to see. Photoreceptors are found in the retina, which lines the back of the eye. The retina contains two types of photoreceptors: rods and cones. Rod cells are highly sensitive to light, function primarily under dim lighting conditions, and are important in peripheral vision. Cone cells are less sensitive to light and function under normal and bright lighting conditions; they are responsible for color vision. In order to maximize their sensitivity, rods have more pigments allowing them to absorb more of the incident light. The photoreceptor cell is divided into two specialized subcellular compartments: an outer segment that contains the machinery of phototransduction, and an inner segment (closer to the eye) which contains the mitochondria, nucleus, and endoplasmic reticulum, and connects to the synaptic terminal (see Fig 1.1). In addition to its function in providing energy and performing protein synthesis, the inner segment also acts as a miniature light guide, trapping light that propagates parallel to the cell's long axis,

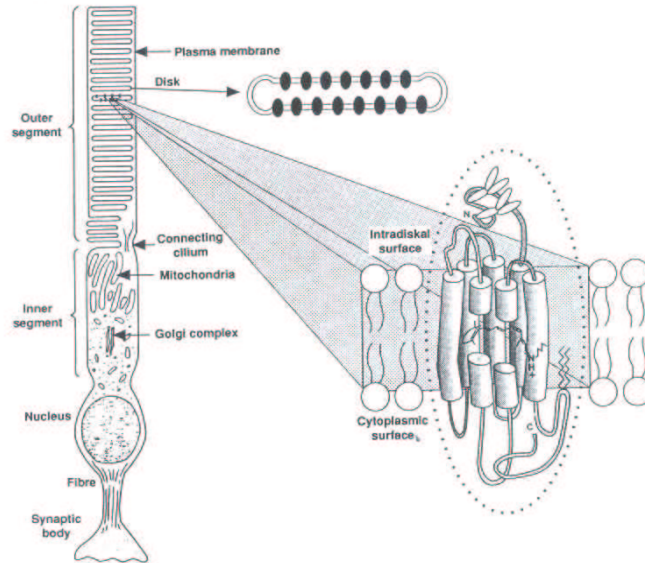


Figure 1.1: The photoreceptor retinal rod cells, from [44]

and guiding it to the outer segment where photon capture and transduction take place. The outer segment comprises a stack of ‘disc’ membranes, spaced uniformly at intervals of about 14 nm. Each disc is made up of two functionally independent layers of lipidic membranes with a viscosity approximately that of olive oil. Therefore all of the protein molecules involved in transduction can diffuse within the plane of the membrane as a result of thermal vibrations. This motion is very important because it is the cause of the rod’s high sensitivity, one of the key features of transduction in rods [25].

Despite being one of the best understood *signal transduction* processes, its formal mathematical description is less developed. Classically the basic signaling processes are investigated in terms of bulk averaged quantities using Michaelis-Menten type kinetics [44], and ordinary differential equations provide solutions which average con-

centrations within the volume of the cell. However, it is becoming increasingly clear from recent investigations that several signaling molecules reside on specific sites within cells or their membrane and depend on their localization effects in a significant manner [30]. Therefore to analyse the regulation process quantitatively, it is necessary to take into account the local concentration, and time-dependent diffusion of second messengers and protein cascades. These processes can be modeled with the help of evolution partial differential equations.

We present numerical simulations of phototransduction in vertebrate rod cells. The simulations build on a mathematical model presented in [4] whose main feature is the inclusion of spatio-temporal variations of the concentration of cGMP and Ca^{2+} . The second messengers cGMP and Ca^{2+} , instead of being bulk quantities, are regarded as pointwise functions of space and time. Our model extends the existing model of [27, 35, 44] (which assumes bulk/lumped quantities of cGMP and Ca^{2+} and is based on ordinary differential equations) by incorporating diffusion effects, thereby giving a pointwise description of the phenomenon by means of evolution partial differential equations. The source terms are correctly modeled as surface–volume reactions occurring on the faces of the discs where cGMP is hydrolyzed. The model incorporates all the mechanisms presently known to operate in phototransduction, and it reduces to simpler models proposed by physiologists: to the longitudinal (one-dimensional) model of [18] by assuming radially uniform concentrations, and to the lumped model [34, 35, 44] under the assumption of uniform (bulk) concentrations (see §2.3).

The numerical simulations trace the space–time evolution of cGMP and Ca^{2+} , in terms of which the current J through the plasma membrane can be computed. Thus, the simulation also provides the distribution of current as a space–time function defined on the lateral boundary of the rod outer segment. It exhibits localization

of the response about the activation site and enables us to quantify the longitudinal spread at any particular time (§4). We tested numerically some facts put forth in the biological literature about the spread of a single photon response [18, 26], and began the process of determining a consistent set of parameters for salamander rods.

The organization of the remaining Chapters is as follows. In Chapter 2 the mathematical models are presented: the Full model in general form (3-dimensional, light may activate any number of discs), the homogenized limit model, the longitudinal model, and the bulk (ODE) model, in physical as well as dimensionless form. This Chapter also addresses the wellposedness issue of the mathematical models. In Chapter 3 we describe in detail the discretization of the mathematical models and parallelization of the numerical schemes. Issues of convergence and stability of the schemes are also addressed there. In Chapter 4 we describe in detail how various parameters of the model were determined from the literature. This chapter also describes briefly the setup for carrying out the numerical simulations and contains the simulation results. The results and further directions are discussed in Chapter 5.

Chapter 2

Mathematical Models

In this Chapter, we present mathematical models for phototransduction in retinal rod cells, one of the best known signal transduction processes, whereby light is converted into an electrical response. Visual transduction has been studied extensively in recent years, and the basic mechanism is now understood at a molecular level [6, 7]. The diffusion-based model presented below (§2.3) was recently developed by Andreucci et al [4], and its homogenized limit was derived by Andreucci et al [5].

2.1 Phototransduction Process

The rod outer segment (ROS) of vertebrates comprises a stack of equispaced *disc* membranes of thickness about 14 nm and at mutual distance of about 14 nm (for the salamander).

The process of phototransduction, whereby light triggers a neural response in the photoreceptor(rod or cone) cells, is effected by a ‘G-protein cascade’, a sequence of reactions initiated by a G-protein-coupled receptor protein. The three principal

proteins of the cascade that are embedded in the disc membrane are: 1. Photopigment Rhodopsin (Rh) also called **receptor**, 2. Heterotrimeric G-protein (G) also called **transducine** and 3. Phosphodiesterase (PDE) also referred to as **effector**. These membrane associated proteins can diffuse on the face of the disc where they are located, but cannot abandon the disc. The lateral (plasma) membrane of the rod contains cGMP-gated channels of small radius. In absence of light these channels are open and allow a positive influx of sodium and calcium (Ca^{2+}) ions. The space within the rod, that is not occupied by the discs, is filled with cytosol, in which cyclic-guanosine monophosphate (cGMP) and Ca^{2+} diffuse.

When a rhodopsin (Rh) absorbs a photon, its 11-*cis*-retinal chromophore rapidly isomerizes, causing the cytoplasmic surface of the protein to become catalytically active. In this state, rhodopsin activates the GTP-binding protein transducin (G). Within a fraction of a second a single active rhodopsin (R^*) causes hundreds of transducins to exchange bound GDP for GTP, forming active TGTP complexes. A highly amplified signal now passes to a third protein, cGMP PDE, which is activated by TGTP. Each of the activated G proteins (G^*) is capable of activating one and only one catalytic subunit of PDE on the activated disc by binding to it upon contact. The bound pair so generated is denoted by PDE^* . This cascade takes place only on the activated disc. The next cascade, involving cGMP and Ca^{2+} , takes place in the cytosol.

Active PDE^* hydrolyzes cGMP to 5'-GMP in the cytoplasm, thereby lowering its concentration. The decrease in concentration of the cGMP causes closure of some of the cGMP-gated channels of the plasma membrane, resulting in a lowering of the influx of positive ions, and thus a lowering of the local current J across the outer membrane. Because of the $\text{Na}^+/\text{K}^+/\text{Ca}^{2+}$ exchanger which continues to remove Ca^{2+}

from the cytoplasm, there is a decrease in the calcium concentration, which in turn results in an increase in cGMP production by stimulation of Ca^{2+} -inhibited guanylyl cyclase, and thus a consequent reopening of the channels. The same decrease of calcium closes the cycle by causing deactivation of rhodopsin through stimulation of rhodopsin kinase. The latter ceases activating new G protein. Thus PDE^* decays to its base value, ending depletion of cGMP.

This cascade is well known and it is supported by a sizable amount of published experimental data [44, 10, 31, 18]. However, despite being one of the best understood *signal transduction* processes, its formal mathematical description, is less developed. The classical methods used to describe signal transduction processes assume a well-stirred aqueous environment, and ordinary differential equations provide solutions which average concentrations within the volume of the cell. Recent investigations [9, 33] suggest that these methods are not adequate to describe the precisely regulated signal transduction processes emanating from these highly localized structures, sometimes called “signalsomes” [9]. The spatio-temporal model presented below addresses localization effects.

The meaning of all variables and parameters entering the mathematical model are listed in Table 2.1.

2.2 Geometry of the Domain

The outer segment of a rod receptor can be considered as a right circular cylinder $\tilde{\Omega}$ of height H and radius R_{rod} , housing a vertical stack of N_{disc} equispaced parallel discs C_i , $i = 1, 2, \dots, N_{\text{disc}}$, each of radius R_{disc} , thickness ϵ , and mutually separated by a distance δ . Each of the discs C_i , $i = 1, 2, \dots, N_{\text{disc}}$, carrying the rhodopsin, is assumed

Table 2.1: Nomenclature

Symbol	Units [‡]	Definition	Reference
$\alpha, \alpha_{\min}, \alpha_{\max}$	$\mu\text{M s}^{-1}$	Rate of synthesis of cGMP by guanylyl cyclase	(2.7), §2.2
B_{Ca}, B_{cG}	-	Buffering power of the cytoplasm for Ca^{2+} , cGMP	(2.4b)
β_{dark}	s^{-1}	Rate constant of cGMP hydrolysis in darkness	(4.2)
β_{sub}	s^{-1}	Rate constant of cGMP hydrolysis per E^* subunit	(4.2)
$[\text{Ca}], [\text{cG}]$	μM	Concentration of Calcium ions, cGMP	(2.1)
C_0, \dots	-	Dimensionless constants ($C_0, C_1, C_2, C_{\min}, C_{\text{ratio}}$)	(2.36)
d	μm	Ratio of cytosol volume to area of the discs	(2.2), §2.2
D_a	$\mu\text{m}^2 \text{s}^{-1}$	Diffusivity of activation of PDE on the disc surface	(2.20)
D_{Ca}, D_{cG}	$\mu\text{m}^2 \text{s}^{-1}$	Diffusion coefficient for Ca, cGMP	(2.1)
D_{ur}, \dots	-	Dimensionless diffusion constants (D_{ur}, D_{wr} , etc.)	(2.36)
δ, ϵ	μm	Interdiscal space, Height of a disc	§2.2
E^*	subunits	Number of activated PDE molecules per rod	(2.22), §2.5, §4.1.3
f_{Ca}	-	Fraction of cGMP-activated current carried by Ca^{2+}	(2.4b)
\mathcal{F}	$\mathcal{C} \text{ mol}^{-1}$	Faraday's constant	(2.4b)
Φ	isom.	Intensity of brief flash	§2.5
H_i, H	μm	Height of one disc unit, Height of the rod	§2.2
I	isom. s^{-1}	Light intensity	(2.22), §2.5
J	pA	Total circulating current ($J = J_{\text{ex}} + J_{\text{cG}}$)	(2.3)
J_{dark}	pA	Dark current	§4.2.2
$J_{\text{dark}} - J$	pA	Response	§4.2.2
$1 - J/J_{\text{dark}}$	pA	Normalized response	§4.2.2
$j_{\text{ex}}^{\text{sat}}$	pA	Saturation exchange current as $[\text{Ca}] \rightarrow \infty$	(2.13)
$j_{\text{cG}}^{\text{max}}$	pA	Maximal exchange current as $[\text{cG}] \rightarrow \infty$	(2.13)
k_{cat}/K_m	$\mu\text{M}^{-1} \text{s}^{-1}$	Hydrolytic efficacy of fully-activated PDE dimer	§4.1
k_E	s^{-1}	Rate constant for inactivation of PDE* molecules	(2.22), §2.5
k_{hyd}	$\mu\text{M}^{-1} \text{s}^{-1}$	Hydrolysis rate of cGMP by dark-activated PDE	(2.8a), §4.1
k_{hyd}^*	$\mu\text{M}^{-1} \text{s}^{-1}$	Hydrolysis rate of cGMP by light-activated PDE	(2.8a), §4.1
k_R	s^{-1}	Rate constant for inactivation of R^* molecules	(2.22), §2.5
K_{cyc}	μM	Ca^{2+} concentration that achieves half max. rate	(2.7), §2.3
K_{cG}	μM	cGMP concentration for half max. channel opening	(2.12), §2.3
K_{ex}	μM	Ca^{2+} concentration for half max. channel opening	(2.13), §2.3
$m_{\text{cyc}}, m_{\text{cG}}$	-	Experimental Hill's exponents	(2.7), (2.13), §2.3
ν_{RE}	s^{-1}	Rate of E^* formation per fully activated R^*	(2.22), §2.5
$N_{\text{active}}, N_{\text{disc}}$	-	Number of light activated discs, Total discs	§2.5
N_{AV}	mol^{-1}	Avagardo Number	§4.1.1
P_0	$\# \text{ disc}^{-1}$	Number of activated phosphodiesterase molecules	(2.20), §2.3
$[\text{PDE}]_s$	$\# \mu\text{m}^{-2}$	Surface density of phosphodiesterase	(2.8a)
$[\text{PDE}^*]_s$	$\# \mu\text{m}^{-2}$	Surface density of activated phosphodiesterase	(2.8a), §2.5, §4.1.3
R^*	$\# \text{ rod}^{-1}$	Number of activated rhodopsin molecules	§2.3
$R_{\text{disc}}, R_{\text{rod}}$	μm	Radius of a disc membrane, Radius of the rod	§2.2
σ_1	μm^2	Area of one disc membrane (πR_{disc}^2)	§2.2
$\sigma_{\text{active}}, \sigma_{\text{disc}}$	μm^2	Area of the activated discs, Total area ($2\sigma_1 N_{\text{disc}}$)	§2.2
Σ_{rod}	μm^2	Lateral surface area of the rod outer segment	§4.1.3
t_{RGE}	s	Delay time for activation	(2.22), §2.3
V_{cyto}	μm^3	Volume of the cytosol in the rod outer segment	§2.2
Ω	-	Domain occupied by the cytosol in the rod	§2.2

[‡]The symbol # denotes number of molecules, isom. denotes number of photoisomerization and “-” signifies dimensionless quantity.

to be a thin cylinder, coaxial with the rod $\tilde{\Omega}$, of radius R_{disc} and height $\epsilon \ll H$. The C_i are equally spaced, i.e., the upper face of C_i has distance δ from the lower face of C_{i+1} . The first C_1 has distance $\delta/2$ from the lower face of the rod $\tilde{\Omega}$ and the last $C_{N_{\text{disc}}}$ has distance $\delta/2$ from the upper face of the rod. The domain of cytosol where diffusion of second messengers takes place is a subset $\Omega \subset \tilde{\Omega}$ not occupied by the cylinders C_i , i.e.,

$$\Omega = \tilde{\Omega} - \bigcup_{i=1}^{N_{\text{disc}}} \bar{C}_i. \quad (2.1)$$

We denote by F_i^\pm the upper/lower disc faces, and by $\partial_o\Omega$ the plasma membrane or the lateral outer boundary (see Fig 2.1). We define σ_1 as the surface area of one face of a disc, $\sigma_{\text{disc}} = 2\sigma_1 N_{\text{disc}}$ the total surface area of the N_{disc} discs, and V_{cyto} the volume of the cytosol. We also introduce the following geometric parameters: $R_o = R_{\text{rod}} - R_{\text{disc}}$, the outer shell thickness, d , the ratio of volume of the cytosol to the area of all discs, and ν , the ratio of volume of all discs to volume of the rod outer segment, thus

$$d = \frac{V_{\text{cyto}}}{\sigma_{\text{disc}}} \approx \frac{\delta}{2}, \quad \nu = \frac{\text{vol}\left(\bigcup_{i=1}^{N_{\text{disc}}} C_i\right)}{\text{vol}(\Omega)} \quad (2.2)$$

2.3 Basic Equations of Diffusion with Interaction

The diffusion of second messengers in the outer segment cytoplasm is essential for communication between the disc and plasma membrane. Derivation of the general diffusion equations for the concentrations $[cG]$ of cGMP and $[Ca]$ of Ca^{2+} in the fluid cytosol is based on mass balance in an elementary volume which states:

$$[\text{Ca}](x, 0) = [\text{Ca}]_{\text{init}}(x) \quad (2.4b)$$

Boundary Conditions for [cG]: We interpret the boundary values of volumic quantities ($[\text{cG}]$, $[\text{Ca}]$) by the standard mathematical notion of *traces* of functions in Sobolov spaces, on lower dimensional manifolds.

We assume that a small beam of photons hits a disc C_{i_o} on one of its faces, say for example the lower one, at coordinate z_o along the axis of the rod. The beam is thought of as uniformly distributed within on the lower face of C_{i_o} . Contribution and removal of free cGMP concentration in the cytoplasm occurs through binding phenomena on the lower and upper faces of each of the disc C_i .

Activation of G-protein cascade causes stimulation of the Phosphodiesterase (PDE) and hence increased hydrolysis of cGMP to 5'-GMP in the cytoplasm, so that the cytoplasmic concentration of cGMP is reduced in the vicinity of the absorbed photon. The rate of depletion (per unit area of disc surface) of cGMP on the faces, as it binds to dark-activated PDE, is given by $k_{\text{hyd}}[\text{PDE}]_s[\text{cG}]$, where k_{hyd} is the catalytic rate of dark-activated PDE and $[\text{PDE}]_s$ is the surface density of PDE, assumed uniformly distributed on the entire area of the faces of the discs C_i ,

$$\{\text{rate of depletion of [cG] on the disc faces}\} = k_{\text{hyd}}[\text{PDE}]_s[\text{cG}]. \quad (2.5)$$

The rate of depletion of $[\text{cG}]$ on the lower face F_i^- of C_{i_o} (where the photon hits), due to PDE* is given by $k_{\text{hyd}}^*[\text{cG}] [\text{PDE}^*]_s$, where k_{hyd}^* is the catalytic rate of the light-activated PDE, and $[\text{PDE}^*]_s$ is the surface density of activated Phosphodiesterase. The final stage of the cascade, the cooperative gating of the channels by cGMP, contributes a component of amplification of cGMP concentration in the cytoplasm modulated by Ca^{2+} . The rate of production of $[\text{cG}]$ on the faces of the discs C_i has

been found to follow the Hill type relation:

$$\{\text{rate of production of [cG] on disc faces}\} = \alpha d, \quad (2.6)$$

with d the volume to area ratio as described in (2.2) and

$$\alpha = \alpha_{\min} + \frac{\alpha_{\max} - \alpha_{\min}}{1 + ([\text{Ca}]/K_{\text{Ca}})^{m_{\text{Ca}}}}, \quad (2.7)$$

the rate of synthesis of cGMP by guanylyl cyclase. The quantity α_{\min} is the residual component of cyclase activity at very high calcium concentrations, $(\alpha_{\max} - \alpha_{\min})$ is the calcium sensitive component of cyclase activity, K_{Ca} is the Ca^{2+} density that achieves half of the maximum rate, and m_{Ca} is a Hill's constant.

We also assume that there are no sources/sinks on the lateral part L_i of the boundary of the discs C_i , nor on the boundary of the rod, $\partial\Omega$. Combining all these, the boundary conditions for [cG] take the form:

$$-D_{\text{cG}} \frac{\partial[\text{cG}]}{\partial z} \Big|_{F_i^\pm} = \pm \alpha d \mp k_{\text{hyd}} [\text{PDE}]_s [\text{cG}] + \delta_{i0} k_{\text{hyd}}^* [\text{PDE}^*]_s [\text{cG}], \quad (2.8a)$$

$$-D_{\text{cG}} \frac{\partial[\text{cG}]}{\partial z} = 0 \quad \text{on } \{z = 0\} \cup \{z = H\}, \quad (2.8b)$$

$$-D_{\text{cG}} \nabla[\text{cG}] \cdot \mathbf{n}_i = 0 \quad \text{on } L_i, \quad (2.8c)$$

$$-D_{\text{cG}} \nabla[\text{cG}] \cdot \mathbf{n} = 0 \quad \text{on } \partial_o\Omega, \quad (2.8d)$$

where

$$\delta_{i0} = \begin{cases} 1 & \text{if } i = i_0 \text{ on the lower face of the active disc,} \\ 0 & \text{otherwise.} \end{cases} \quad (2.9)$$

Boundary Conditions for [Ca]: Calcium does not penetrate the disc C_i carrying rhodopsin. Thus

$$-D_{\text{Ca}} \nabla[\text{Ca}] \cdot \mathbf{n}_i = 0 \quad \text{on } L_i, \quad (2.10)$$

where \mathbf{n}_i is the unit inner normal to C_i .

We assume that calcium enters or leaves the cytoplasm only via the cGMP-gated channels and the electrogenic exchange. Physiologists [34, 35, 44] have related the rate of change of (free) Ca^{2+} directly to the currents,

$$\{\text{total rate of change of } [\text{Ca}]\} = \frac{1}{B_{\text{Ca}} \mathcal{F}} \left(\frac{1}{2} f_{\text{Ca}} J_{\text{cG}} - J_{\text{ex}} \right), \quad (2.11)$$

where J_{cG} is the current carried by the cGMP-gated channel, J_{ex} is the electrogenic current carried by the exchanger, f_{Ca} is the fraction of cGMP-activated current carried by Ca^{2+} , B_{Ca} is the buffering power (the ratio of the increment in total concentration by the increment in the free concentration) of the cytoplasm for calcium and \mathcal{F} is the Faraday constant (the charge carried by a mole of monovalent cations).

By convention, current flowing inward across the membrane is regarded positive, i.e., both J_{cG} and J_{ex} are positive. The factor multiplying $f_{\text{Ca}} J_{\text{cG}}$ is $\frac{1}{2}$ because each Ca^{2+} ion carries two charges, while the factor multiplying J_{ex} is unity because the extrusion of each Ca^{2+} ion is accompanied by the net movement inward of single positive charge ($4\text{Na}^+ - (\text{Ca}^{2+} + \text{K}^+)$ [44, pp 44]).

The current J_{ex} at the boundary of the rod, due to electrogenic exchange may be described by the Michaelis-Menten type relation [35, 44]

$$J_{\text{ex}} = \frac{j_{\text{ex}}^{\text{sat}}}{1 + K_{\text{ex}}/[\text{Ca}]}, \quad (2.12)$$

where $j_{\text{ex}}^{\text{sat}}$ is the maximal or saturation exchange current (as $\text{Ca}^{2+} \rightarrow \infty$) and K_{ex} is the half-saturating Ca^{2+} concentration of the exchanger.

The current J_{cG} , carried by the cGMP-gated channels (at a fixed membrane voltage), has been found to follow the Hill type relation [35, 44]

$$J_{\text{cG}} = \frac{j_{\text{cG}}^{\text{max}}}{1 + (K_{\text{cG}}/[\text{cG}])^{m_{\text{cG}}}}, \quad (2.13)$$

where j_{cG}^{\max} is its maximum (saturation) value at high concentration of cGMP, K_{cG} is the half maximum constant for cGMP, and m_{Ca} is a (dimensionless) Hill's constant. Since (2.11) represents the flow rate of [Ca] across the plasma membrane of area Σ_{rod} of the rod outer segment, the flux of [Ca] (per unit area of plasma membrane) is obtained by dividing (2.11) by the area Σ_{rod} . Thus, the boundary conditions for [Ca] take the form:

$$-D_{Ca} \frac{\partial [Ca]}{\partial z} = 0 \quad \text{on } F_i^\pm, \quad (2.14a)$$

$$-D_{Ca} \frac{\partial [Ca]}{\partial z} = 0 \quad \text{on } \{z = 0\} \cup \{z = H\}, \quad (2.14b)$$

$$-D_{Ca} \nabla [Ca] \cdot \mathbf{n}_i = 0 \quad \text{on } L_i, \quad (2.14c)$$

$$-D_{Ca} \nabla [Ca] \cdot \mathbf{n} = \frac{1}{B_{Ca} \mathcal{F} \Sigma_{\text{rod}}} \left(J_{\text{ex}} - \frac{1}{2} f_{Ca} J_{cG} \right) \quad \text{on } \partial_o \Omega. \quad (2.14d)$$

Summarizing, the full model consists of (2.3), (2.4), (2.8), (2.14). The local current at a point of the plasma membrane (with local concentrations [cG], [Ca]) is the sum $J_{cG} + J_{\text{ex}}$ of (2.12) and (2.13).

2.4 Simpler Models

2.4.1 1D Longitudinal Model

A simplified, one-dimensional model along the longitudinal (z) direction, can be obtained by assuming that the problem has axial symmetry with respect to the angular coordinate θ and uniform spatial distribution in the radial (r) direction. Indeed, (2.14d) gives the flow rate of per unit area of lateral rod surface. Thus, integrating (2.14d) over the lateral surface Σ_{rod} of the rod outer segment, we obtain the total flow rate of [Ca] in the entire rod. Under the assumption of spatially uniform concen-

trations in the radial (r) direction, the total flow rates must be considered as source terms. The longitudinal model takes the following form.

$$[\text{cG}](z, 0) = [\text{cG}]_{\text{init}}(z), \quad [\text{Ca}](z, 0) = [\text{Ca}]_{\text{init}}(z), \quad (2.15)$$

$$\frac{\partial[\text{cG}]}{\partial t} - D_{\text{cG}} \frac{\partial^2[\text{cG}]}{\partial z^2} = 0, \quad (2.16a)$$

$$\frac{\partial[\text{Ca}]}{\partial t} - D_{\text{Ca}} \frac{\partial^2[\text{Ca}]}{\partial z^2} = \frac{1}{B_{\text{Ca}} \mathcal{F} V_{\text{cyto}}} \left(J_{\text{ex}} - \frac{1}{2} f_{\text{Ca}} J_{\text{cG}} \right), \quad (2.16b)$$

for $0 < z < H$ and $t > 0$, and the boundary conditions given by

$$- D_{\text{cG}} \frac{\partial[\text{cG}]}{\partial z} = 0 \quad \text{on} \quad \{z = 0\} \cup \{z = H\}, \quad (2.17a)$$

$$- D_{\text{cG}} \frac{\partial[\text{cG}]}{\partial z} \Big|_{F_i^\pm} = \pm \alpha d \mp k_{\text{hyd}} [\text{PDE}]_s[\text{cG}] + \delta_{i0} k_{\text{hyd}}^* [\text{PDE}^*]_s[\text{cG}], \quad (2.17b)$$

$$- D_{\text{Ca}} \frac{\partial[\text{Ca}]}{\partial z} = 0 \quad \text{on} \quad F_i^\pm \cup \{z = 0\} \cup \{z = H\}. \quad (2.17c)$$

Note that the quantity V_{cyto} on the right side of (2.16b) comes from the conversion of the boundary source of (2.14d) to a volumic source.

2.4.2 Bulk (ODE) Model

The one-dimensional longitudinal model (§2.5.1) reduces to the lumped model of [35, 44] under the assumption of uniform concentrations. The total flow rate of $[\text{cG}]$ in the entire rod, obtained by integrating (2.8a) over the surface of all the discs, becomes a source term for the rate of change of bulk $[\text{cG}]$. The rate of change of $[\text{Ca}]$ is simply given by the source term in (2.16b). Thus, the bulk (ordinary differential equations) model obtained by further reduction of the one dimensional longitudinal model described above takes the form

$$[\text{cG}](0) = [\text{cG}]_{\text{init}}, \quad [\text{Ca}](0) = [\text{Ca}]_{\text{init}}, \quad (2.18)$$

and for $t > 0$

$$\frac{\partial[\text{cG}]}{\partial t} = \alpha - \frac{1}{d} (k_{\text{hyd}} [\text{PDE}]_s + \delta_{i_0} k_{\text{hyd}}^* [\text{PDE}^*]_s) [\text{cG}], \quad (2.19\text{a})$$

$$\frac{\partial[\text{Ca}]}{\partial t} = \frac{1}{B_{\text{Ca}} \mathcal{F} V_{\text{cyto}}} \left(J_{\text{ex}} - \frac{1}{2} f_{\text{Ca}} J_{\text{cG}} \right). \quad (2.19\text{b})$$

Note that the total $[\text{Ca}]$ flow rate is identical to that of [35], while the matching of the $[\text{cG}]$ flow rate is shown in §4.1.1.

2.5 Activation Models

Light activation is embodied in the term $[\text{PDE}^*]_s$ which needs to be specified. In lieu of a detailed model of the rhodopsin to PDE^* cascade taking place on activated discs, we need to account for the activated PDE by expressing the surface density $[\text{PDE}^*]_s$ as some function of space $x = (r, z, \theta)$ and time t , and possibly also of concentrations. A satisfactory full modeling of the function $[\text{PDE}^*]_s(x, t)$, for x ranging over a face $F_{i_0}^-$ hit by a photon, is a major open problem and one of the future goals of our investigation. The literature contains various attempts to describe such a quantity (see [44, 22, 35, 4]). The function $[\text{PDE}^*]_s(x, t)$ should exhibit the following features:

- (a) a time dependent mechanism, accounting for recovery and/or inactivation of the receptor and of the effector,
- (b) a space decay behavior, away from the activation site, accounting for the diffusion of the receptor, transducin and effector, on the disc surface.

There may be various different ways of arriving at such a function. Some possibilities are described below. Determination of activation parameter values is described in §4.1.

2.5.1 Activation by a Gaussian

We consider the activation of PDE as the response to a Dirac delta source of strength P_0 at $r = 0$ and at $t = t_{\text{on}}$ diffusing radially on the disc surface. Thus, $[\text{PDE}^*]_s(t)$ could be described by a gaussian, the fundamental solution of two-dimensional diffusion on a surface, as

$$[\text{PDE}^*]_s(r, t) = \frac{P_0}{4\pi D_a(t - t_{\text{on}})} \exp\left(-\frac{r^2}{4D_a(t - t_{\text{on}})}\right), \quad (2.20)$$

with P_0 the number of activated PDE* molecules on a disc, D_a a diffusivity of activation of PDE by transducin on the disc surface, and t_{on} the time at which light strikes the disc.

2.5.2 Activation via a Lumped Model

Here we consider a simple activation method with a lumped deterministic model, by taking the surface density of activated PDE molecules as

$$[\text{PDE}^*]_s(t) = E^*(t) / (\sigma_1 \cdot N_{\text{active}}), \quad (2.21)$$

where $E^*(t)$ is the number of activated PDE molecules in the entire rod and $N_{\text{active}} \cdot \sigma_1$ is the surface area of activated N_{active} discs.

Following [34, 44], the quantity $E^*(t)$ is approximated in terms of two first-order rate constants k_R , k_E representing R^* decay and concurrent $G^* - \text{PDE}^*$, decay respectively, as

$$E^*(t) = \Phi \cdot \left(\frac{\nu_{\text{RE}}}{k_R - k_E}\right) (e^{-k_E(t-t_{\text{RGE}})} - e^{-k_R(t-t_{\text{RGE}})}), \quad t > t_{\text{RGE}}, \quad (2.22)$$

where Φ is the number of photoisomerizations per rod per flash, ν_{RE} is the effective rate with which a single R^* triggers activation of PDE*, and t_{RGE} is the sum of delay

time constants, $t_{\text{R}} + t_{\text{G}} + t_{\text{E}}$. The rate constant ν_{RE} depends on diffusion coefficients and the probability of successful encounters [44]. The quantity $E^*(t)$ in (2.21) can also be obtained by solving the following set of ordinary differential equations [35] for activated rhodopsin, $R^*(t)$, and activated PDE, $E^*(t)$,

$$\frac{dR^*}{dt} = I - k_{\text{R}}R^*, \quad \frac{dE^*}{dt} = \nu_{\text{RE}}R^* - k_{\text{E}}E^*. \quad (2.23)$$

Here I is the intensity of the light flash in photoisomerisations per second, ν_{RE} is the rate of E^* formation per fully activated R^* and k_{R} , k_{E} are the rate constants for inactivation R^* , E^* respectively. Let t_{on} and Δt_{flash} denote the starting time and the duration of the flash, in seconds, respectively. A flash of duration Δt_{flash} , delivering Φ photoisomerizations to the rod, results in light intensity

$$I(t) = \begin{cases} \Phi/\Delta t_{\text{flash}}, & t_{\text{on}} < t < t_{\text{on}} + \Delta t_{\text{flash}}, \\ 0, & t > t_{\text{on}} + \Delta t_{\text{flash}}. \end{cases}$$

Assuming constant decay rate k_{R} , the system of ordinary differential equations in (2.23) can be solved analytically for $t > t_{\text{on}}$ giving $R^*(t) = 0$, $E^*(t) = 0$ for $t < t_{\text{on}}$,

$$R^*(t) = I \cdot \frac{1}{k_{\text{R}}} (1 - e^{k_{\text{R}}t}), \quad (2.24a)$$

$$E^*(t) = I \cdot \frac{\nu_{\text{RE}}}{k_{\text{E}} k_{\text{R}} (k_{\text{R}} - k_{\text{E}})} [k_{\text{R}} (1 - e^{-k_{\text{E}}t}) - k_{\text{E}} (1 - e^{-k_{\text{R}}t})], \quad (2.24b)$$

for $t_{\text{on}} < t < t_{\text{on}} + \Delta t_{\text{flash}}$, and

$$R^*(t) = I \cdot \frac{1}{k_{\text{R}}} (1 - e^{k_{\text{R}}\Delta t_{\text{flash}}}) e^{k_{\text{R}}t}, \quad (2.25a)$$

$$E^*(t) = I \cdot \frac{\nu_{\text{RE}}}{k_{\text{E}} k_{\text{R}} (k_{\text{R}} - k_{\text{E}})} [k_{\text{R}} (1 - e^{-k_{\text{E}}\Delta t_{\text{flash}}}) - k_{\text{E}} (1 - e^{-k_{\text{R}}\Delta t_{\text{flash}}}) - k_{\text{E}} (1 - e^{-k_{\text{R}}\Delta t_{\text{flash}}}) (e^{-k_{\text{R}}t} - e^{-k_{\text{E}}t})], \quad (2.25b)$$

for $t > t_{\text{on}} + \Delta t_{\text{flash}}$. We can see that the $E^*(t)$ given by (2.22) agrees with that given by (2.25b) in the asymptotic limit as $\Delta t_{\text{flash}} \rightarrow 0$.

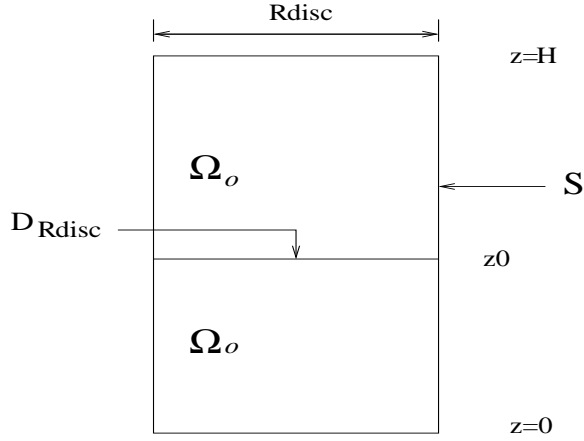


Figure 2.2: The simplified geometry for the homogenized problem

2.6 Homogenized Limit Problem

Utilizing the mathematical theories of Homogenization and Concentrated Capacity, Andreucci et al in [5] have developed the Homogenized Limit of the model problem ((2.3), (2.4), (2.8), (2.14)) described above in a simplified geometry (see Fig 2.2).

The geometry of the rod outer segment exhibits two thin compartments, available to diffusion: the interdiscal spaces and the outer shell surrounding the stack of discs. The diffusion within the interdiscal spaces appears to be prevalent in the transversal directions and it cannot be neglected in view of the reaction terms acting on the faces of the discs. The longitudinal diffusion along the outer shell cannot be neglected because it regulates the opening and closing of the ionic channels. The numerical values of ϵ and R_{rod} indicate that $\epsilon \ll R_{\text{rod}}$ i.e., the thickness of the interdiscal spaces and that of the outer shell are negligible with respect to the radius R_{rod} . This suggests that ϵ can be regarded as a homogenization parameter to be let go to zero. In doing so the discs C_i within the rod become thinner. We visualize such a process to be carried out in such a way that as $\epsilon \rightarrow 0$ the number of discs increases so that the

ratio between the volume occupied by the discs and the volume of the rod, remains a fixed fraction of 1.

On the other hand, the width of outer shell is comparable to the mutual distance of adjacent discs. Thus, as $\epsilon \rightarrow 0$ the thickness of the outer shell also vanishes and, roughly speaking, the outer shell tends to a cylindrical surface. A suitable device to preserve information on diffusion in the increasingly thinner outer shell is to concentrate the capacities. For this, the coefficients in the diffusion equation should be changed to compensate the geometrical alteration of the domain, so that the total mass contained in the outer shell stays fixed in the limit.

We describe the problem in cylindrical coordinates (r, θ, z) . Let $\bar{x} = (r, \theta)$ and $x = (\bar{x}, z)$. As the homogenization parameter ϵ (thickness of the disc) $\rightarrow 0$, the computational domain of the original problem (see §2.2) $\Omega (= \Omega_\epsilon) = \tilde{\Omega}_\epsilon - \bigcup_{i=1}^{N_{\text{disc}}} \bar{C}_i$ tends to the cylinder $\Omega_0 = D_{R_{\text{disc}}} \times (0, H)$, where $D_{R_{\text{disc}}}$ is a disc, centered at the origin of \mathbb{R}^2 , and of radius R_{disc} . An interdiscal space, adjacent to a photon-activated disc at height z_0 tends to the disc $D_{R_{\text{disc}}} \times \{z_0\}$. Similarly, the outer shell tends to the cylindrical surface $S = \{r = R_{\text{disc}}\} \times (0, H)$.

Let $\{[cG]_\epsilon, [Ca]_\epsilon\}$ be the family of ϵ -approximate solution of the original problem ((2.3), (2.4), (2.8), (2.14)). The functions $[cG]_\epsilon(x, t)$ and $[Ca]_\epsilon(x, t)$ generate three pairs of limiting functions, each representing $[cG]$ and $[Ca]$ in different parts of the rod outer segment.

- $\{[cG], [Ca]\}$ defined in Ω_o , called the interior limit,
- $\{[c\bar{G}], [C\bar{a}]\}$ defined in $D_{R_{\text{disc}}} \times \{z = z_0\}$, called the special level z_0 ,
- $\{[\widehat{cG}], [\widehat{Ca}]\}$ defined on S , called the limit on the outer shell.

The interior limits $[cG]$ and $[Ca]$ are defined on a volumic domain and their physical dimension is unchanged, while the last two limits are defined as limits of averages over the surfaces, keeping the dimensions same as that of the interior limits e.g.,

$$[\widehat{cG}](\theta, z, t) = \lim_{\epsilon \rightarrow 0} \frac{1}{R_o} \int_{R_{\text{disc}}}^{R_{\text{rod}}} [cG]_{\epsilon}(r, \theta, z, t) dr. \quad (2.26)$$

This formula implies that $[\widehat{cG}]$, while defined on the surface $(0, 2\pi] \times (0, H)$, keeps its physical dimensions in μM .

The homogenized limit problem has the following form:

1. The interior limit (in Ω_o , $t > 0$)

$$\frac{\partial [cG]}{\partial t} - D_{cG} \nabla_{\bar{x}}^2 [cG] = \alpha + \frac{1}{d} k_{\text{hyd}} [\text{PDE}]_s [cG], \quad (2.27a)$$

$$\frac{\partial [Ca]}{\partial t} - D_{Ca} \nabla_{\bar{x}}^2 [Ca] = 0. \quad (2.27b)$$

2. The limit on the activated level z_o (on $D_{R_{\text{disc}}}$, $t > 0$)

$$\frac{\partial [c\bar{G}]}{\partial t} - D_{cG} \nabla_{\bar{x}}^2 [c\bar{G}] = \alpha + \frac{1}{d} k_{\text{hyd}} [\text{PDE}]_s [c\bar{G}] - \frac{1}{2d} k_{\text{hyd}}^* [\text{PDE}^*]_s [c\bar{G}], \quad (2.28a)$$

$$\frac{\partial [\bar{Ca}]}{\partial t} - D_{Ca} \nabla_{\bar{x}}^2 [\bar{Ca}] = 0. \quad (2.28b)$$

3. The outer shell limit (on S , $t > 0$)

$$\frac{\partial [\widehat{cG}]}{\partial t} - D_{cG} \nabla_S^2 [\widehat{cG}] = -\frac{(1-\nu)}{R_o} D_{cG} \left. \frac{\partial [cG]}{\partial r} \right|_{r=R_{\text{disc}}} - \delta_{z_o} \frac{2d}{R_o} D_{cG} \left. \frac{\partial [cG]}{\partial r} \right|_{r=R_{\text{disc}}}, \quad (2.29a)$$

$$\begin{aligned} \frac{\partial [\widehat{Ca}]}{\partial t} - D_{Ca} \nabla_S^2 [\widehat{Ca}] = & -\frac{(1-\nu)}{R_o} D_{Ca} \left. \frac{\partial [Ca]}{\partial r} \right|_{r=R_{\text{disc}}} - \delta_{z_o} \frac{2d}{R_o} D_{Ca} \left. \frac{\partial [Ca]}{\partial r} \right|_{r=R_{\text{disc}}} \\ & - \frac{1}{B_{Ca} \mathcal{F} R_o \Sigma_{\text{rod}}} \left(\frac{j_{\text{ex}}^{\text{sat}}}{1 + K_{\text{ex}}/[\widehat{Ca}]} \right) \\ & + \frac{1}{B_{Ca} \mathcal{F} R_o \Sigma_{\text{rod}}} \frac{1}{2} f_{Ca} \left(\frac{j_{cG}^{\text{max}}}{1 + (K_{cG}/[\widehat{cG}])^{m_{cG}}} \right), \quad (2.29b) \end{aligned}$$

where ∇_S^2 is the Laplace-Beltrami Operator on the cylindrical surface S , namely,

$$\nabla_S^2 = \frac{1}{R_{\text{disc}}^2} \frac{\partial^2}{\partial \theta^2} + \frac{\partial^2}{\partial z^2}. \quad (2.30)$$

For the limit in the outer shell problem, we have the following homogeneous Neumann boundary conditions:

$$\frac{\partial}{\partial z}[\widehat{\text{cG}}](\theta, 0, t) = \frac{\partial}{\partial z}[\widehat{\text{cG}}](\theta, H, t) = 0, \quad (2.31a)$$

$$\frac{\partial}{\partial z}[\widehat{\text{Ca}}](\theta, 0, t) = \frac{\partial}{\partial z}[\widehat{\text{Ca}}](\theta, H, t) = 0. \quad (2.31b)$$

The above three pairs of concentration functions $\{[\text{cG}], [\text{Ca}]\}$, $\{[\text{c}\bar{\text{G}}], [\bar{\text{Ca}}]\}$ and $\{[\widehat{\text{cG}}], [\widehat{\text{Ca}}]\}$ are related by the following continuity requirements:

$$[\text{c}\bar{\text{G}}](\bar{x}, t) = [\text{cG}](\bar{x}, z, t)|_{z=z_0}, \quad [\widehat{\text{cG}}](\theta, z, t) = [\text{cG}](\bar{x}, z, t)|_{r=R_{\text{disc}}}, \quad (2.32a)$$

$$[\bar{\text{Ca}}](\bar{x}, t) = [\text{Ca}](\bar{x}, z, t)|_{z=z_0}, \quad [\widehat{\text{Ca}}](\theta, z, t) = [\text{Ca}](\bar{x}, z, t)|_{r=R_{\text{disc}}}. \quad (2.32b)$$

For the complete mathematical descriptions of the homogenization process we refer to the original work [5], where Andreucci et al have established the uniqueness of the solutions of the limit homogenization problem in its weak formulation. The undimensionalized weak form of the homogenized limit problem is presented in §2.7.4.

2.7 Undimensionalization

2.7.1 Full Model

We employ cylindrical coordinates to describe the model. Introduce the dimensionless variables: $u = \frac{[\text{cG}]}{\tilde{u}}$ and $w = \frac{[\text{Ca}]}{\tilde{w}}$, with $\tilde{u} = K_{\text{cG}}$, the half maximum constant for cGMP, and $\tilde{w} = K_{\text{ex}}$, the half maximum constant for Ca^{2+} appearing in (2.12),

(2.13). The independent variables r , z and t are rescaled respectively by \tilde{r} , \tilde{z} and \tilde{t} . The proper choice of time and space scales will be discussed in detail in §4.1.4. The usual length scales $\tilde{r} = R_{\text{rod}}$, $\tilde{z} = H$, and $\tilde{t} = \tilde{z}^2/D$, where $D = \max(D_{\text{cG}}, D_{\text{Ca}})$, makes the axial flux of calcium at the lateral boundary very small. Thus, special attention has been given to rescale the boundary condition (2.14d). The time scale \tilde{t} is chosen so as to make the coefficients 1 and C_{ratio} on the right hand side of (2.34c). The problem can be restated in dimensionless form as:

Given $u(r, z, \theta, 0) = u_{\text{init}}(r, z, \theta)$, $w(r, z, \theta, 0) = w_{\text{init}}(r, z, \theta)$, find $u(r, z, \theta, t)$, $w(r, z, \theta, t)$ for $0 < t < T$, such that

$$\frac{\partial u}{\partial t} + \nabla \cdot \mathbf{F}_u = 0 \quad \text{in } \Omega, t > 0, \quad (2.33a)$$

$$\frac{\partial w}{\partial t} + \nabla \cdot \mathbf{F}_w = 0 \quad \text{in } \Omega, t > 0, \quad (2.33b)$$

$$F_{ur} = 0 \quad \text{on } L_i \cup \partial\Omega, t > 0, \quad (2.34a)$$

$$F_{wr} = 0 \quad \text{on } L_i, t > 0, \quad (2.34b)$$

$$F_{wr} = g_1(w) - C_{\text{ratio}} g_2(u) \quad \text{on } \partial\Omega, t > 0, \quad (2.34c)$$

$$F_{uz} = 0 \quad \text{on } \{z = 0\} \cup \{z = H\}, t > 0, \quad (2.34d)$$

$$F_{uz} = \pm (C_{\text{min}} + C_1 f_1(w)) \mp C_2 u + \delta_{io} C_0 P(r, t) u \quad \text{on } F_i^\pm, t > 0, \quad (2.34e)$$

$$F_{wz} = 0 \quad \text{on } F_i^\pm \cup \{z = 0\} \cup \{z = H\}, t > 0. \quad (2.34f)$$

The fluxes $\mathbf{F}_u = (F_{ur}, F_{uz}, F_{u\theta})$ and $\mathbf{F}_w = (F_{wr}, F_{wz}, F_{w\theta})$ are given by

$$\begin{aligned} F_{ur} &= -D_{ur} \frac{\partial u}{\partial r}, & F_{uz} &= -D_{uz} \frac{\partial u}{\partial z}, & F_{u\theta} &= -D_{u\theta} \frac{1}{r} \frac{\partial u}{\partial \theta}, \\ F_{wr} &= -D_{wr} \frac{\partial w}{\partial r}, & F_{wz} &= -D_{wz} \frac{\partial w}{\partial z}, & F_{w\theta} &= -D_{w\theta} \frac{1}{r} \frac{\partial w}{\partial \theta}. \end{aligned} \quad (2.35)$$

The dimensionless constants and the functions f_1 , g_1 , g_2 , P are defined as

$$\begin{aligned}
D_{ur} &= \frac{\tilde{t}}{\tilde{r}^2} D_{cG}, & D_{u\theta} &= \frac{\tilde{t}}{\tilde{r}^2} D_{cG}, & D_{uz} &= \frac{\tilde{t}}{\tilde{z}^2} D_{cG}, \\
D_{wr} &= \frac{\tilde{t}}{\tilde{r}^2} D_{Ca}, & D_{w\theta} &= \frac{\tilde{t}}{\tilde{r}^2} D_{Ca}, & D_{wz} &= \frac{\tilde{t}}{\tilde{z}^2} D_{Ca}, \\
C_{\min} &= \frac{\tilde{t} d}{\tilde{z} \tilde{u}} \alpha_{\min}, & C_{\text{ratio}} &= \frac{1}{2} f_{Ca} \frac{j_{cG}^{\max}}{j_{\text{ex}}^{\text{sat}}}, & C_0 P &= \frac{\tilde{t}}{\tilde{z}} k_{\text{hyd}}^* [\text{PDE}^*]_s, \\
C_1 &= \frac{\tilde{t} d}{\tilde{z} \tilde{u}} (\alpha_{\max} - \alpha_{\min}), & C_2 &= \frac{\tilde{t}}{\tilde{z}} k_{\text{hyd}} [\text{PDE}]_s, \\
f_1(w) &= \frac{1}{1 + (\gamma w)^{m_{Ca}}}, & \gamma &= \frac{\tilde{w}}{K_{Ca}}, & g_1(w) &= \frac{w}{1 + w}, & g_2(u) &= \frac{u^{m_{cG}}}{1 + u^{m_{cG}}}.
\end{aligned} \tag{2.36}$$

All quantities are now dimensionless. The quantity $P = [\text{PDE}^*]_s$ represents the strength of PDE*-cGMP interaction, and thus the effect of activation by light.

2.7.2 1D Longitudinal Model

A similar undimensionalization (as in §2.7.1) of (2.17) leads to the following problem. Given $u(z, 0) = u_{\text{init}}(z)$, $w(z, 0) = w_{\text{init}}(z)$, find $u(z, t)$, $w(z, t)$ for $0 < z < H$ and $0 < t < T$, such that

$$\frac{\partial u}{\partial t} + \frac{\partial F_{uz}}{\partial z} = 0, \tag{2.37a}$$

$$\frac{\partial w}{\partial t} + \frac{\partial F_{wz}}{\partial z} = g_1(w) - C_{\text{ratio}} g_2(u), \tag{2.37b}$$

$$F_{uz} = 0 \quad \text{on} \quad \{z = 0\} \cup \{z = H\}, \tag{2.38a}$$

$$F_{uz} = \pm (C_{\min} + C_1 f_1(w)) \mp C_2 u + \delta_{io} C_0 P(r, t) u \quad \text{on} \quad F_i^\pm, \tag{2.38b}$$

$$F_{wz} = 0 \quad \text{on} \quad F_i^\pm \cup \{z = 0\} \cup \{z = H\}. \tag{2.38c}$$

2.7.3 Homogenized Model

Introduce the dimensionless variables: $u = \frac{[\text{cG}]}{\tilde{u}}$, $w = \frac{[\text{Ca}]}{\tilde{w}}$, $\bar{u} = \frac{[\text{cG}]}{\tilde{u}}$, $\bar{w} = \frac{[\text{Ca}]}{\tilde{w}}$, $\hat{u} = \frac{[\widehat{\text{cG}}]}{\tilde{u}}$, $\hat{w} = \frac{[\widehat{\text{Ca}}]}{\tilde{w}}$, with $\tilde{u} = K_{\text{cG}}$, $\tilde{w} = K_{\text{ex}}$, as in §2.7.1. Here we use the same lengths and time scale as in the Full Model, i.e., \tilde{r} , \tilde{z} and \tilde{t} are as given in (4.32) with a slight change (Σ_{disc} instead of Σ_{rod}) since in the homogenized geometry the surface area of the lateral boundary is Σ_{disc} .

Using the above mentioned dimensionless variables and scales, and realizing that $\bar{u} \equiv u(z_o)$, $\bar{w} \equiv w(z_o)$, we rewrite the homogenized version of the model problem in dimensionless form as follows.

Find $u(r, z, \theta, t)$ and $w(r, z, \theta, t)$ such that

$$\frac{\partial u}{\partial t} + \nabla_{r,\theta} \cdot \Phi_u = S_{\min} + S_1 f_1(w) - S_2 u - \delta_{z_0} S_0 u P(r, t), \quad (2.39a)$$

$$\frac{\partial w}{\partial t} + \nabla_{r,\theta} \cdot \Phi_w = 0, \quad (2.39b)$$

with fluxes

$$\left\{ \begin{array}{l} \Phi_u = (\Phi_{ur}, \Phi_{u\theta}), \quad \Phi_{ur} = -D_{ur} \frac{\partial u}{\partial r}, \quad \Phi_{u\theta} = -D_{u\theta} \frac{1}{r} \frac{\partial u}{\partial \theta}, \\ \Phi_w = (\Phi_{wr}, \Phi_{w\theta}), \quad \Phi_{wr} = -D_{wr} \frac{\partial w}{\partial r}, \quad \Phi_{w\theta} = -D_{w\theta} \frac{1}{r} \frac{\partial w}{\partial \theta}, \end{array} \right. \quad (2.40)$$

for $0 < r < R_{\text{disc}}$, $0 \leq \theta < 2\pi$, $t > 0$, where the function P is as defined in (2.36); and satisfying the following boundary conditions:

$$\left\{ \begin{array}{l} \text{At } r = 0 : \quad \Phi_{ur} = 0 = \Phi_{wr}, \\ \text{At } r = R_{\text{disc}} : \quad u(r, z, \theta, t) = \hat{u}(z, \theta, t), \quad w(r, z, \theta, t) = \hat{w}(z, \theta, t), \\ \text{At } \theta = 0, 2\pi : \quad u(r, z, 0, t) = u(r, z, 2\pi, t), \quad w(r, z, 0, t) = w(r, z, 2\pi, t), \\ \quad \quad \quad \Phi_{u\theta}|_{\theta=0} = \Phi_{u\theta}|_{\theta=2\pi}, \quad \Phi_{w\theta}|_{\theta=0} = \Phi_{w\theta}|_{\theta=2\pi}, \end{array} \right. \quad (2.41)$$

where $\hat{u}(z, \theta, t)$, $\hat{w}(z, \theta, t)$ are the solutions of the following system of partial differential equations defined on the lateral surface $S = \{r = R_{\text{disc}}\} \times (0, H)$,

$$\frac{\partial \hat{u}}{\partial t} + \nabla_{z,\theta} \cdot \Psi_{\hat{u}} = (b + \delta_{z_0} b_o) \Phi_{ur}|_{r=R_{\text{disc}}}, \quad (2.42a)$$

$$\frac{\partial \hat{w}}{\partial t} + \nabla_{z,\theta} \cdot \Psi_{\hat{w}} = S_{\text{ratio}} g_2(\hat{u}) - \frac{1}{R_o} g_1(\hat{w}) + (b + \delta_{z_0} b_o) \Phi_{wr}|_{r=R_{\text{disc}}}, \quad (2.42b)$$

with fluxes

$$\left\{ \begin{array}{l} \Psi_{\hat{u}} = (\Psi_{\hat{u}z}, \Psi_{\hat{u}\theta}), \quad \Psi_{\hat{u}z} = -D_{\hat{u}z} \frac{\partial \hat{u}}{\partial z}, \quad \Psi_{\hat{u}\theta} = -D_{\hat{u}\theta} \frac{1}{r} \frac{\partial \hat{u}}{\partial \theta}, \\ \Psi_{\hat{w}} = (\Psi_{\hat{w}z}, \Psi_{\hat{w}\theta}), \quad \Psi_{\hat{w}z} = -D_{\hat{w}z} \frac{\partial \hat{w}}{\partial z}, \quad \Psi_{\hat{w}\theta} = -D_{\hat{w}\theta} \frac{1}{r} \frac{\partial \hat{w}}{\partial \theta}, \end{array} \right. \quad (2.43)$$

for $0 < z < H$, $0 \leq \theta < 2\pi$, $t > 0$, where the functions g_1 , g_2 are as defined in the (2.36), and the boundary conditions

$$\left\{ \begin{array}{l} \text{At } z = 0 : \quad \Psi_{\hat{u}z} = 0 = \Psi_{\hat{w}z}, \\ \text{At } z = H : \quad \Psi_{\hat{u}z} = 0 = \Psi_{\hat{w}z}, \\ \text{At } \theta = 0, 2\pi : \quad \hat{u}(z, 0, t) = \hat{u}(z, 2\pi, t), \quad \hat{w}(z, 0, t) = \hat{w}(z, 2\pi, t), \\ \Psi_{\hat{u}\theta}|_{\theta=0} = \Psi_{\hat{u}\theta}|_{\theta=2\pi}, \quad \Psi_{\hat{w}\theta}|_{\theta=0} = \Psi_{\hat{w}\theta}|_{\theta=2\pi}. \end{array} \right. \quad (2.44)$$

The dimensionless constants are defined as

$$\begin{aligned} D_{ur} &= \frac{\tilde{t}}{\tilde{r}^2} D_{\text{cG}}, & D_{uz} &= \frac{\tilde{t}}{\tilde{z}^2} D_{\text{cG}}, & D_{u\theta} &= \frac{\tilde{t}}{\tilde{r}^2} D_{\text{cG}}, \\ D_{wr} &= \frac{\tilde{t}}{\tilde{r}^2} D_{\text{Ca}}, & D_{wz} &= \frac{\tilde{t}}{\tilde{z}^2} D_{\text{Ca}}, & D_{w\theta} &= \frac{\tilde{t}}{\tilde{r}^2} D_{\text{Ca}}, \\ S_0 &= \frac{1}{2} \frac{\tilde{t}}{\text{d}} k_{\text{hyd}}^*, & S_{\text{min}} &= \frac{\tilde{t}}{\tilde{u}} \alpha_{\text{min}}, & S_1 &= \frac{\tilde{t}}{\tilde{u}} (\alpha_{\text{max}} - \alpha_{\text{min}}), \\ S_2 &= \frac{\tilde{t}}{\text{d}} k_{\text{hyd}} [\text{PDE}]_s, & S_{\text{ratio}} &= \frac{1}{R_o} \frac{f_{\text{Ca}}}{2} \frac{j_{\text{cG}}^{\text{max}}}{j_{\text{ex}}^{\text{sat}}}, \\ R_o &= \frac{1}{\tilde{r}} (R_{\text{rod}} - R_{\text{disc}}), & b_o &= \frac{1}{R_o}, & b &= (1 - \nu) b_o. \end{aligned} \quad (2.45)$$

2.7.4 Homogenized Model in Weak Form

A similar undimensionalization (as in §2.7.3) of the weak form of the homogenized problem ((2.27) - (2.32)) leads to the following problem.

$$\begin{aligned}
& (1 - \nu) \int_0^\tau \int_0^\eta \int_0^\rho \int_0^{2\pi} \psi \left\{ \frac{\partial u}{\partial t} + \nabla_{r,\theta} \cdot \Phi_u - S_{\min} - S_1 f_1(w) + S_2 u \right\}_{z \neq z_0} r d\theta dr dz dt \\
& \quad + \rho_o \int_0^\tau \int_0^\eta \int_0^{2\pi} \psi \left\{ \frac{\partial \hat{u}}{\partial t} + \nabla_{z,\theta} \cdot \Psi_{\hat{u}} - \frac{(1 - \nu)}{\rho_o} \Phi_{ur} \right\}_{r=\rho} \rho d\theta dz dt \\
& + \zeta \int_0^\tau \int_0^\rho \int_0^{2\pi} \psi \left\{ \frac{\partial \bar{u}}{\partial t} + \nabla_{r,\theta} \cdot \Phi_{\bar{u}} - S_{\min} - S_1 f_1(\bar{w}) + S_2 \bar{u} + S_0 \bar{u} P \right\}_{z=z_0, r \neq \rho} r d\theta dr dt \\
& \quad - \zeta \int_0^\tau \int_0^{2\pi} \{ \psi \Phi_{\bar{u}r} \}_{z=z_0, r=\rho} \rho d\theta dt = 0, \tag{2.46a}
\end{aligned}$$

$$\begin{aligned}
& (1 - \nu) \int_0^\tau \int_0^\eta \int_0^\rho \int_0^{2\pi} \psi \left\{ \frac{\partial w}{\partial t} + \nabla_{r,\theta} \cdot \Phi_w \right\}_{z \neq z_0} r d\theta dr dz dt \\
& + \rho_o \int_0^\tau \int_0^\eta \int_0^{2\pi} \psi \left\{ \frac{\partial \hat{w}}{\partial t} + \nabla_{z,\theta} \cdot \Psi_{\hat{w}} - \frac{(1 - \nu)}{\rho_o} \Phi_{wr} + S_{\text{ex}} g_1(\hat{w}) - S_{\text{cG}} g_2(\hat{w}) \right\}_{r=\rho} \rho d\theta dz dt \\
& \quad + \zeta \int_0^\tau \int_0^\rho \int_0^{2\pi} \psi \left\{ \frac{\partial \bar{w}}{\partial t} + \nabla_{r,\theta} \cdot \Phi_{\bar{w}} \right\}_{z=z_0, r \neq \rho} r d\theta dr dt \\
& \quad - \zeta \int_0^\tau \int_0^{2\pi} \{ \psi \Phi_{\bar{w}r} \}_{z=z_0, r=\rho} \rho d\theta dt = 0. \tag{2.46b}
\end{aligned}$$

where ψ is a test function and the fluxes are given by

$$\begin{aligned}
\Phi_u &= (\Phi_{ur}, \Phi_{u\theta}), & \Phi_{ur} &= -D_{ur} \frac{\partial u}{\partial r}, & \Phi_{u\theta} &= -D_{u\theta} \frac{1}{r} \frac{\partial u}{\partial \theta}, \\
\Phi_w &= (\Phi_{wr}, \Phi_{w\theta}), & \Phi_{wr} &= -D_{wr} \frac{\partial w}{\partial r}, & \Phi_{w\theta} &= -D_{w\theta} \frac{1}{r} \frac{\partial w}{\partial \theta}, \\
\Psi_{\hat{u}} &= (\Psi_{\hat{u}z}, \Psi_{\hat{u}\theta}), & \Psi_{\hat{u}z} &= -D_{uz} \frac{\partial \hat{u}}{\partial z}, & \Psi_{\hat{u}\theta} &= -D_{u\theta} \frac{1}{r} \frac{\partial \hat{u}}{\partial \theta}, \\
\Psi_{\hat{w}} &= (\Psi_{\hat{w}z}, \Psi_{\hat{w}\theta}), & \Psi_{\hat{w}z} &= -D_{wz} \frac{\partial \hat{w}}{\partial z}, & \Psi_{\hat{w}\theta} &= -D_{w\theta} \frac{1}{r} \frac{\partial \hat{w}}{\partial \theta}.
\end{aligned}$$

The dimensionless constants are defined as

$$\begin{aligned}
\tau &= \frac{T}{\tilde{t}}, \quad \rho_o = \frac{R_{\text{rod}} - R_{\text{disc}}}{\tilde{r}}, \quad \zeta = \frac{d}{\tilde{z}}, \quad \rho = \frac{R_{\text{disc}}}{\tilde{r}}, \quad \eta = \frac{H}{\tilde{z}}, \\
D_{ur} &= \frac{\tilde{t}}{\tilde{r}^2} D_{\text{cG}}, \quad D_{uz} = \frac{\tilde{t}}{\tilde{z}^2} D_{\text{cG}}, \quad D_{u\theta} = \frac{\tilde{t}}{\tilde{r}^2} D_{\text{cG}}, \\
D_{wr} &= \frac{\tilde{t}}{\tilde{r}^2} D_{\text{Ca}}, \quad D_{wz} = \frac{\tilde{t}}{\tilde{z}^2} D_{\text{Ca}}, \quad D_{w\theta} = \frac{\tilde{t}}{\tilde{r}^2} D_{\text{Ca}}, \\
S_0 &= \frac{\tilde{t}}{d} k_{\text{hyd}}^*, \quad S_{\min} = \frac{\tilde{t}}{\tilde{u}} \alpha_{\min}, \quad S_1 = \frac{\tilde{t}}{\tilde{u}} (\alpha_{\max} - \alpha_{\min}), \quad S_2 = \tilde{t} k_{\text{hyd}} [\text{PDE}], \\
S_{\text{ex}} &= \frac{\tilde{t} j_{\text{ex}}^{\text{sat}}}{\tilde{r}^2 \tilde{z} \tilde{w} \rho_o B_{\text{Ca}} \mathcal{F} \Sigma}, \quad S_{\text{cG}} = \frac{\tilde{t} \frac{1}{2} f_{\text{Ca}} j_{\text{cG}}^{\text{max}}}{\tilde{r}^2 \tilde{z} \tilde{w} \rho_o B_{\text{Ca}} \mathcal{F} \Sigma}, \quad \Sigma = \frac{\Sigma_{\text{disc}}}{\tilde{r} \tilde{z}}.
\end{aligned} \tag{2.47}$$

2.8 Well-posedness of the Model Problems

Parabolic systems with nonlinear boundary conditions arising in certain reaction diffusion systems have been studied by several researchers e.g. Alikakos [2], Amann H. [3], Pao [38], Ruan [47], and the existence and regularity of the local solution has been established. Properties of solutions, such as existence and boundedness, stability of the steady-state solutions, and asymptotic behavior have been investigated by various researchers. A detailed exposition of the general theory of nonlinear parabolic systems, with historical notes, can be found in [39].

Let Ω be a bounded open domain in \mathbb{R}^3 , and let $\partial\Omega$ be the boundary of Ω . For each $T > 0$, let $\Omega_T = \Omega \times (0, T)$ and $\partial\Omega_T = \partial\Omega \times (0, T)$. Consider the following system of parabolic partial differential equations

$$(u_i)_t - D_i \nabla^2 u_i = p_i(x, t, u_i), \quad (x, t) \in \Omega_T, \tag{2.48a}$$

$$\frac{\partial u_i}{\partial \nu} + \beta_i u_i = q_i(x, t, u_1, u_2), \quad (x, t) \in \partial\Omega_T, \tag{2.48b}$$

$$u_i(x, 0) = u_{i,0}(x), \quad x \in \Omega, \tag{2.48c}$$

for $i = 1, 2$, where D_1, D_2 are positive constants, and u_1, u_2 are concentrations.

Note that our full model problem ((2.27), (2.28)) is a special case of the system (2.48), when $p_i(x, t, u_i) \equiv 0$ (see (2.56), (2.57)). The homogenized limit problems can also be put into the above form with different boundary and source functions.

Assumption 2.8.1. (1) The boundary $\partial\Omega$ is sufficiently smooth and $\beta_i \geq 0$. (2) The functions $p_i(x, t, \xi_i)$ are continuous in $\bar{\Omega} \times \bar{\mathbb{R}}_+ \times \mathbb{R}$. $\frac{\partial p_i}{\partial \xi_j}$ exists for $(x, t) \in \Omega \times \bar{\mathbb{R}}_+$, $(\xi_1, \xi_2) \in \mathbb{R}^2$ and $i, j = 1, 2$. For each $(\xi_1, \xi_2) \in \mathbb{R}^2$ and $T > 0$, $p_i \in C^{\delta, \delta/2}(\bar{\Omega} \times [0, T])$, $\delta > 0$. (3) The functions $q_i(x, t, \xi_1, \xi_2)$ are continuous in $\partial\Omega \times \bar{\mathbb{R}}_+ \times \mathbb{R}^2$. $\frac{\partial q_i}{\partial \xi_j}$ exists for $(x, t) \in \partial\Omega \times \bar{\mathbb{R}}_+$, $(\xi_1, \xi_2) \in \mathbb{R}^2$ and $i, j = 1, 2$. For each $(\xi_1, \xi_2) \in \mathbb{R}^2$ and $T > 0$, $q_i \in C^{2+\delta, 1+\delta/2}(\partial\Omega_T)$. (4) $u_{i,0} \in C^\delta(\bar{\Omega})$ and $u_{i,0}$ satisfy the boundary conditions

$$\frac{\partial u_{i,0}}{\partial \nu} + \beta_i u_{i,0} = q_i(x, 0, u_{1,0}, u_{2,0}), \quad \text{for } x \in \partial\Omega, \quad i = 1, 2.$$

Under the above assumptions the system (2.48) has unique local solution u_1, u_2 , where $u_1, u_2 \in C^{2+\delta, 1+\delta/2}(\bar{\Omega} \times [0, T])$ (see [38]).

We will obtain the well-posedness of our model problems by using the ‘‘Comparison-Existence Theorem’’ from [39, pp. 393, 468]. The result is based on upper and lower solutions and their associated monotone iteration. This method is applicable only to a certain class of boundary conditions and source terms, namely quasimonotone functions.

Definition 2.8.1. A function $q_i = q_i(u_1, \dots, u_n)$ is said to be quasimonotone nondecreasing (resp. nonincreasing) if for fixed u_i , the function q_i is nondecreasing (resp. nonincreasing) in u_j for $j \neq i$.

Definition 2.8.2. A function $\mathbf{q} = (q_1, q_2)$ is called quasimonotone nondecreasing (resp. nonincreasing) in $J_1 \times J_2$ if both q_1 and q_2 are quasimonotone nondecreasing (resp. nonincreasing) for $(u_1, u_2) \in J_1 \times J_2$.

Since the functions $\mathbf{p} = (p_1, p_2)$, $\mathbf{q} = (q_1, q_2)$ in our model problem are quasimonotone nondecreasing, we confine our discussion for the quasimonotone nondecreasing functions only.

Definition 2.8.3. *When p_i, q_i are quasimonotone nondecreasing functions, a pair of functions $(\bar{u}_1, \bar{u}_2), (\underline{u}_1, \underline{u}_2)$ in $C(\bar{\Omega}_T) \cap C^{1,2}(\Omega_T)$ are called ordered upper and lower solutions of (2.48a,b,c) if they satisfy the relation $\bar{u}_i \geq \underline{u}_i$ and for $i = 1, 2$*

$$(\bar{u}_i)_t - D_i \nabla^2 \bar{u}_i - p_i(x, t, \bar{u}_i) \geq 0 \geq (\underline{u}_i)_t - D_i \nabla^2 \underline{u}_i - p_i(x, t, \underline{u}_i), \quad (x, t) \in \Omega_T, \quad (2.49a)$$

$$\frac{\partial \bar{u}_i}{\partial \nu} - q_i(x, t, \bar{u}_1, \bar{u}_2) \geq 0 \geq \frac{\partial \underline{u}_i}{\partial \nu} - q_i(x, t, \underline{u}_1, \underline{u}_2), \quad (x, t) \in \partial\Omega_T, \quad (2.49b)$$

$$\bar{u}_i(x, 0) \geq u_{i,0}(x) \geq \underline{u}_i(x, 0), \quad x \in \Omega. \quad (2.49c)$$

Note: If p_i, q_i are not both quasimonotone nondecreasing, then the conditions (2.49a,b) in the above definition need to be changed (see [39]).

Definition 2.8.4. *For a given pair of ordered upper and lower solutions $\bar{\mathbf{u}} = (\bar{u}_1, \bar{u}_2)$, $\underline{\mathbf{u}} = (\underline{u}_1, \underline{u}_2)$, we define a sector*

$$\langle \underline{\mathbf{u}}, \bar{\mathbf{u}} \rangle = \{(u_1, u_2) \in C(\bar{\Omega}) : \underline{u}_i \leq u_i \leq \bar{u}_i, \quad i = 1, 2\}. \quad (2.50)$$

For a given set of ordered upper and lower solutions $(\bar{u}_1, \bar{u}_2), (\underline{u}_1, \underline{u}_2)$, we assume that there exist nonnegative functions $\underline{c}_i \in C^\alpha(\bar{\Omega} \times [0, T])$, $\underline{b}_i \in C^{1+\alpha}(\partial\Omega_T)$, such that for any $(u_1, u_2), (v_1, v_2) \in \langle \underline{\mathbf{u}}, \bar{\mathbf{u}} \rangle$, the functions p_i, q_i satisfy one sided Lipschitz condition

$$p_i(x, t, u_i) - p_i(x, t, v_i) \geq -\underline{c}_i(u_i - v_i), \quad i = 1, 2, \quad (2.51a)$$

$$q_1(x, t, u_1, u_2) - q_1(x, t, v_1, v_2) \geq -b_1(u_1 - v_1), \quad (2.51b)$$

$$q_2(x, t, u_1, u_2) - q_2(x, t, u_1, v_2) \geq -b_2(u_2 - v_2), \quad (2.51c)$$

when $u_i \geq v_i$, for $i = 1, 2$. To ensure the uniqueness of the solution, we also assume that there exist bounded nonnegative functions $K_i \equiv K_i(x, t)$, $K'_i \equiv K'_i(x, t)$ such that for any $(u_1, u_2), (v_1, v_2) \in \langle \mathbf{u}, \bar{\mathbf{u}} \rangle$

$$|p_i(x, t, u_i) - p_i(x, t, v_i)| \geq -K_i|u_i - v_i|, \quad i = 1, 2, \quad (2.52a)$$

$$|q_i(x, t, u_1, u_2) - q_i(x, t, v_1, v_2)| \geq -K'_i(|u_1 - v_1| + |u_2 - v_2|), \quad i = 1, 2. \quad (2.52b)$$

Define

$$P_i(x, t, u_i) = \mathfrak{c}_i u_i + p_i(x, t, u_i), \quad (2.53a)$$

$$Q_i(x, t, u_1, u_2) = \mathfrak{b}_i u_i + q_i(x, t, u_1, u_2). \quad (2.53b)$$

By the above assumptions (2.51) and (2.52), the functions P_i and Q_i are monotone nondecreasing in u_i for each $i = 1, 2$, and satisfy the Lipschitz condition as in (2.52). By the hypothesis on p_i and q_i , P_i is Hölder continuous in $\Omega_T \times \langle \mathbf{u}, \bar{\mathbf{u}} \rangle$ and Q_i is continuous on $\partial\Omega_T \times \langle \mathbf{u}, \bar{\mathbf{u}} \rangle$.

Let $(u_1^{(0)}, u_2^{(0)})$ be any initial iterate in $C^\alpha(\Omega_T)$ and construct a sequence $\{u_1^{(k)}, u_2^{(k)}\}$ from the iteration process

$$(u_i^{(k)})_t - D_i \nabla^2 u_i^{(k)} + \mathfrak{c}_i u_i^{(k)} = P_i(x, t, u_i^{(k-1)}), \quad (x, t) \in \Omega_T, \quad (2.54a)$$

$$\frac{\partial u_i^{(k)}}{\partial \nu} + \mathfrak{b}_i u_i^{(k)} = Q_i(x, t, u_1^{(k-1)}, u_2^{(k-1)}), \quad (x, t) \in \partial\Omega_T, \quad (2.54b)$$

$$u_i^{(k)}(x, 0) = u_{i,0}(x), \quad x \in \Omega. \quad (2.54c)$$

Since for fixed k problem (2.54) is linear and uncoupled, the sequence $\{u_1^{(k)}, u_2^{(k)}\}$ is well defined.

The existence and uniqueness of the solutions of the problem (2.48) is then guaranteed by the following Existence - Comparison Theorem (see [39, p. 468]).

Theorem 2.8.1. *Let $\bar{\mathbf{u}} = (\bar{u}_1, \bar{u}_2)$, $\mathbf{u} = (u_1, u_2)$ be ordered upper and lower solutions of (2.48a,b,c) and let (q_1, q_2) be quasimonotone nondecreasing in $\langle \mathbf{u}, \bar{\mathbf{u}} \rangle$ and satisfy the conditions (2.51) and (2.52). Then the problem (2.48) has a unique solution $(u_1, u_2) \in \langle \mathbf{u}, \bar{\mathbf{u}} \rangle$. Moreover, the sequences $\{\bar{u}_1^{(k)}, \bar{u}_2^{(k)}\}$, $\{u_1^{(k)}, u_2^{(k)}\}$ obtained from (2.54) with $(\bar{u}_1^{(0)}, \bar{u}_2^{(0)}) = (\bar{u}_1, \bar{u}_2)$ and $(u_1^{(0)}, u_2^{(0)}) = (u_1, u_2)$ converge monotonically to (u_1, u_2) and satisfy the relation*

$$(u_1, u_2) \leq (u_1^{(k)}, u_2^{(k)}) \leq (u_1, u_2) \leq (\bar{u}_1^{(k)}, \bar{u}_2^{(k)}) \leq (\bar{u}_1, \bar{u}_2) \quad \text{in } \Omega_T, \quad (2.55)$$

for every $k = 1, 2, \dots$.

Next, we verify that our mathematical models satisfy the assumptions of this theory.

Full Model: Let $\partial\Omega = \partial\Omega_1 \cup \partial\Omega_2 \cup \partial\Omega_3 \cup \partial\Omega_4 \cup \partial\Omega_5 \cup \partial\Omega_6$, where $\partial\Omega_1, \partial\Omega_2, \partial\Omega_5$ and $\partial\Omega_3, \partial\Omega_4, \partial\Omega_6$ denote the top, bottom and lateral boundary of the rod and the disc respectively. Consider the following system for $i = 1, 2$,

$$(u_i)_t - D_i \nabla^2 u_i = 0, \quad (x, t) \in \Omega_T, \quad (2.56a)$$

$$\frac{\partial u_i}{\partial \nu} = q_i(x, t, u_1, u_2), \quad (x, t) \in \partial\Omega_T, \quad (2.56b)$$

$$u_i(x, 0) = u_{i,0}(x), \quad x \in \Omega, \quad (2.56c)$$

where D_i are positive constants, and the boundary functions q_i are defined as follows

$$q_1(x, t, u_1, u_2) = \begin{cases} 0, & x \in \partial\Omega_1, \\ 0, & x \in \partial\Omega_2, \\ a + \frac{b}{1 + (\gamma u_2)^2} - c u_1, & x \in \partial\Omega_3, \\ a + \frac{b}{1 + (\gamma u_2)^2} - \tilde{c}(x, t) u_1, & x \in \partial\Omega_4, \\ 0, & x \in \partial\Omega_5, \\ 0, & x \in \partial\Omega_6, \end{cases} \quad (2.57a)$$

$$q_2(x, t, u_1, u_2) = \begin{cases} 0, & x \in \partial\Omega_1, \\ 0, & x \in \partial\Omega_2, \\ 0, & x \in \partial\Omega_3, \\ 0, & x \in \partial\Omega_4, \\ \frac{u_1^2 d}{1 + u_1^2} - \frac{u_2 e}{1 + u_2}, & x \in \partial\Omega_5, \\ 0, & x \in \partial\Omega_6, \end{cases} \quad (2.57b)$$

with $a = C_{\min}/Du_z$, $b = C_1/Du_z$, $C = C_2/Du_z$, $\tilde{c}(x, t) = c + \delta_{i, i_0} C_0 P(x, t)/Du_z$,
 $d = C_{\text{ratio}}/Dw_r$, $e = 1/Dw_r$. Thus

$$a, b, c, d, e > 0, \quad \tilde{c}(x, t) \geq c > 0, \quad d > e. \quad (2.58)$$

With slightly smoothing the lower and upper edges of the cylinder Ω , it can be easily verified that all the assumptions in **Assumption 2.8.1** are satisfied for the model problem (2.56).

Also note that $\frac{\partial q_1}{\partial u_2} \geq 0$, $\frac{\partial q_2}{\partial u_1} \geq 0$. Thus both functions q_1, q_2 in (2.57) are quasimonotone nondecreasing.

Now, to apply the Existence - Comparison Theorem (2.8.1) for (2.56) we need to show existence of some ordered upper and lower solutions for (2.56). Our particular

interest in application is the existence of nonnegative upper and lower solutions, so that the problem under consideration (2.56) will have a nonnegative solution.

Since we have

$$q_1(x, t, 0, \xi) \geq 0, \quad q_2(x, t, \xi, 0) \geq 0, \quad \text{for } \xi \geq 0, \quad (2.59)$$

we can choose $(\underline{u}_1, \underline{u}_2) = (0, 0)$ as the lower solution.

In §4.1.2, we obtain the uniform steady state solution $U_1 > 0, U_2 > 0$ for the above system (2.56a), making $q_i(x, t, U_1, U_2) \equiv 0$ for $i = 1, 2$.

Choose $(\bar{u}_1, \bar{u}_2) = (U_1, U_2)$. Then (U_1, U_2) and $(0, 0)$ clearly satisfy conditions (2.49) when $p_i \equiv 0$, for the upper and lower solutions for the problem (2.56). Thus a unique nonnegative solution $\mathbf{u} = (u_1, u_2)$ for (2.56) is guaranteed by Theorem 2.8.1.

To show the positive property of the solution \mathbf{u} , with the condition (2.55), we observe from the iteration process (2.54) that the first iteration for $(\underline{u}_1^{(k)}, \underline{u}_2^{(k)})$ is guaranteed positive, by the Maximum Principle, in $\bar{\Omega}_T$ unless $u_i \equiv 0$. It follows from $(u_1, u_2) \geq (\underline{u}_1^{(1)}, \underline{u}_2^{(1)})$ that the solution $\mathbf{u} = (u_1, u_2)$ must be positive in $\bar{\Omega}_T$ unless $u_i \equiv 0$.

Homogenized Model: The interior limit problem ((2.27), (2.32)), the limit on the special level z_o ((2.28), (2.32)) and the limit on the outer shell ((2.29), (2.31)) all are special cases of the nonlinear system (2.48). The nonlinear functions on the source terms $(p_i(x, t, u_1, u_2), i = 1, 2)$ are almost identical with the functions $(q_i(x, t, u_1, u_2), i = 1, 2)$ of the full model (2.57) satisfying the quasimonotone property. Thus all the hypotheses of the theorem (2.8.1) are satisfied and hence the wellposedness of the problem is established.

Andreucci et al in [4] have established the uniqueness of the solutions of the limit homogenization problem in its weak form.

Chapter 3

Finite Volume Models

In this section we develop computational models based on finite volume discretization for the mathematical models discussed in Chapter 2.

The finite volume method is a standard approach to construct approximate solutions of various types (elliptic, parabolic or hyperbolic) of conservation laws. It is very popular and has been extensively used for the numerical simulation of many industrial problems. There are several numerical methods with different names (e.g., control volume finite element methods, multi-element balancing method, integrated finite difference method, generalized finite difference methods etc.) which can be viewed as finite volume methods. From the numerical analysis point of view, these methods are basically regarded as integral interpolation methods. Some of the nice features of finite volume methods are similar to those of the finite element method: it may be used on arbitrary geometries, using structured or nonstructured meshes, natural boundary conditions are easy to deal with, and it leads to robust schemes. The best feature of the finite volume method is that it maintains the conservation law at the discrete level because it is based on the “balance” approach. A local balance

equation is written on each discretized “finite volume” and an integral formulation of the fluxes over the boundary (faces) of the finite volume is then obtained using the Divergence Theorem. Then the fluxes are discretized in terms of the discrete unknowns. Despite its popularity in various applications, the mathematical theory of finite volume methods is very recent and still not as well developed as that of finite element methods [13, 46].

3.1 Full Model

For simplicity, we assume axial symmetry to reduce the problem to two space dimensions in (r, z) coordinates. The 3-dimensional case would be entirely analogous. Let $N_{\text{disc}} \in \mathbb{N}, I_f \in \mathbb{N}, I_m \in \mathbb{N}, J_f \in \mathbb{N}$ and $J_m \in \mathbb{N}$ be some mesh dimensioning numbers. Let $I_{mf} = I_m + I_f$, $J_{mf} = J_m + J_f$, $J_{fmf} = J_f + J_m + J_f$ and $JN_{fmf} = N_{\text{disc}} \cdot J_{fmf}$. We set up $\mathcal{M} = (V_{i,j})_{i=1,\dots,I_{mf};j=1,\dots,JN_{fmf}}$ a two dimensional (r, z) mesh for an axisymmetric problem in Ω by subdividing the length $[0, R_{\text{disc}}]$ into I_m subintervals of width $\Delta r = R_{\text{disc}}/I_m$; $[R_{\text{disc}}, R_{\text{rod}}]$ into I_f subintervals of width $\Delta r = (R_{\text{rod}} - R_{\text{disc}})/I_f$; $[0, \epsilon]$ into J_m subintervals of width $\Delta z = \epsilon/J_m$; and $[0, \delta]$ into $2J_f$ subintervals of width $\Delta z = \delta/(2J_f)$. The mesh \mathcal{M} for the computational domain Ω is defined as

$$\mathcal{M} = \tilde{\mathcal{M}} - \bigcup_{N=1}^{N=N_{\text{disc}}} \mathcal{M}_N, \quad (3.1)$$

where

$$\mathcal{M}_N = \{V_{i,j} \in \mathcal{M}, i = 1, \dots, I_m, j = NJ_{fmf} - J_{mf} + 1, \dots, NJ_{fmf} - J_f\}.$$

Thus the total number of control volumes in Ω is

$$N_{\text{disc}} \times (I_m + I_f) \times (J_m + 2J_f) . \quad (3.2)$$

We assign one node to each of these control volumes $V_{i,j}$.

Let $\Delta r_0 = 0$, $\Delta r_{I_{mf}+1} = 0$, $\Delta z_0 = 0$, $\Delta z_{JN_{f_{mf}}+1} = 0$. For $i = 1, \dots, I_{mf}$, let $r_{\frac{1}{2}} = 0$, $r_{i+\frac{1}{2}} = r_{i-\frac{1}{2}} + \Delta r_i$, (so that $r_{I_{mf}+\frac{1}{2}} = R_{\text{disc}}$ and $r_{I_{mf}+\frac{1}{2}} = R_{\text{rod}}$), and for $j = 1, \dots, JN_{f_{mf}}$, $z_{\frac{1}{2}} = 0$, $z_{j+\frac{1}{2}} = z_{j-\frac{1}{2}} + \Delta z_j$, (so that $z_{J_{f+\frac{1}{2}}} = \frac{\delta}{2}$, $z_{J_{f_{mf}}+\frac{1}{2}} = \delta + \epsilon, \dots$, and $z_{JN_{f_{mf}}+\frac{1}{2}} = \sum_{i=1}^{N_{\text{disc}}} H_i = H$), and the volume $V_{i,j}$ is given by

$$V_{i,j} = 2\pi \int_{r_{i-\frac{1}{2}}}^{r_{i+\frac{1}{2}}} \int_{z_{j-\frac{1}{2}}}^{z_{j+\frac{1}{2}}} dz r dr = \pi \left(r_{i+\frac{1}{2}}^2 - r_{i-\frac{1}{2}}^2 \right) \Delta z_j. \quad (3.3)$$

The area of the radial ($A_{i-\frac{1}{2},j}$) and axial ($A_{i,j-\frac{1}{2}}$) faces are

$$A_{i-\frac{1}{2},j} = 2\pi r \int_{z_{j-\frac{1}{2}}}^{z_{j+\frac{1}{2}}} dz = 2\pi r_{i-\frac{1}{2}} \Delta z_j, \quad A_{i,j-\frac{1}{2}} = 2\pi \int_{r_{i-\frac{1}{2}}}^{r_{i+\frac{1}{2}}} r dr = \pi \left(r_{i+\frac{1}{2}}^2 - r_{i-\frac{1}{2}}^2 \right). \quad (3.4)$$

Let $(r_i)_{i=0,1,\dots,I_{mf}+1}$ and $(z_j)_{j=0,1,\dots,JN_{f_{mf}}+1}$ be such that

$$\begin{aligned} r_{i-\frac{1}{2}} < r_i < r_{i+\frac{1}{2}}, & \quad \text{for } i = 1, 2, \dots, I_{mf}, \quad r_0 = 0, \quad r_{I_{mf}+1} = r_{\text{rod}}, \\ z_{j-\frac{1}{2}} < z_j < z_{j+\frac{1}{2}}, & \quad \text{for } j = 1, 2, \dots, JN_{f_{mf}}, \quad z_0 = 0, \quad z_{JN_{f_{mf}}+1} = H. \end{aligned} \quad (3.5)$$

The 2D axisymmetric (r, z) mesh for a disc unit and for the whole rod outer segment geometries are shown in Fig 3.1 .

Time discretization is performed with variable time steps. Let $T > 0$ be the maximum time of interest, $\{t_0 \dots, t_{N_{\text{max}}}\}$, a partition of $[0, T]$, and $\Delta t_n = t_{n+1} - t_n$ the time step size.

3.1.1 Discretization of the PDEs

Integrating (2.33) over the control volume $V_{i,j}$ and time interval $[t_n, t_n + \Delta t_n]$, we obtain

$$\int_{t_n}^{t_n+\Delta t_n} \frac{\partial}{\partial t} \int_{V_{i,j}} u dV dt = - \int_{t_n}^{t_n+\Delta t_n} \int_{\partial V_{i,j}} F_u \cdot \mathbf{n} dA dt, \quad (3.6a)$$

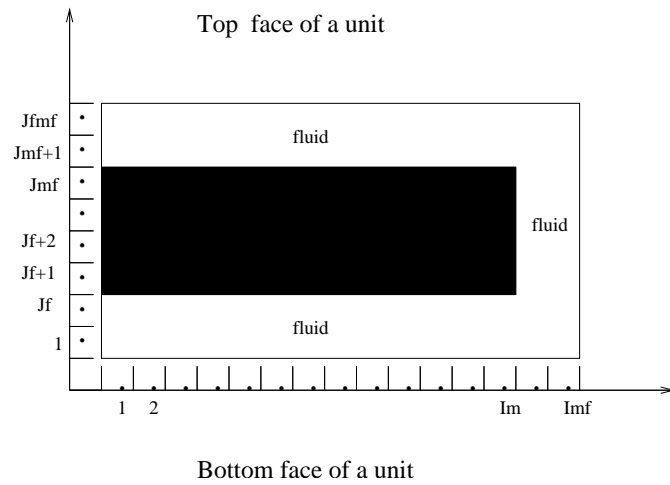
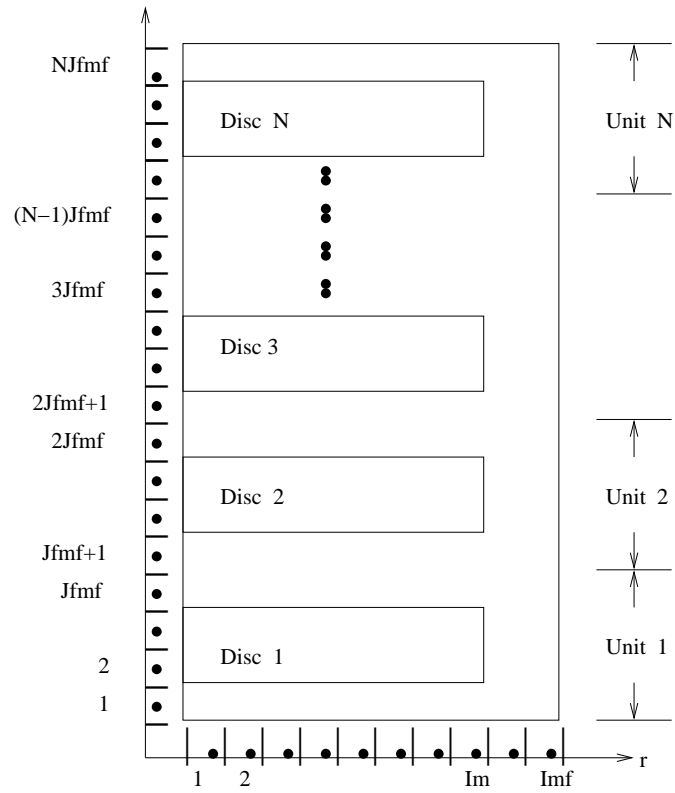


Figure 3.1: Finite volume (r, z) mesh. A disc unit (lower), full rod (upper)

$$\int_{t_n}^{t_n+\Delta t_n} \frac{\partial}{\partial t} \int_{V_{i,j}} w \, dV \, dt = - \int_{t_n}^{t_n+\Delta t_n} \int_{\partial V_{i,j}} F_w \cdot \mathbf{n} \, dA \, dt. \quad (3.6b)$$

Define $U_{i,j}^n \approx u(r_i, z_j, t_n)$, $W_{i,j}^n \approx w(r_i, z_j, t_n)$, as the mean values over the control volume $V_{i,j}$

$$U_{i,j}^n = \frac{1}{V_{i,j}} \int_{V_{i,j}} u(r, z, t_n) \, dV, \quad (3.7a)$$

$$W_{i,j}^n = \frac{1}{V_{i,j}} \int_{V_{i,j}} w(r, z, t_n) \, dV. \quad (3.7b)$$

Also introduce the numerical fluxes as mean values over area and time of $F_u(r, z, t)$, $F_w(r, z, t)$. Then the flux integrals in (3.6) can be computed by $\sum_{\text{faces}} (\text{Area} \times \text{Flux})$, the sum of the flow rates across all the faces of the control volume $V_{i,j}$, where the flow rates across the faces are expressed as

$$(AF)_{i-\frac{1}{2},j}^{u;n} = \frac{1}{\Delta t_n} \int_{t_n}^{t_n+\Delta t_n} \int_{A_{i-\frac{1}{2},j}} F_u(r, z, t) \cdot \mathbf{n} \, dA \, dt \quad (\text{Radial}), \quad (3.8a)$$

$$(AF)_{i,j-\frac{1}{2}}^{u;n} = \frac{1}{\Delta t_n} \int_{t_n}^{t_n+\Delta t_n} \int_{A_{i,j-\frac{1}{2}}} F_u(r, z, t) \cdot \mathbf{n} \, dA \, dt \quad (\text{Axial}), \quad (3.8b)$$

and similarly for w . Let $t_{n+\vartheta} := t_n + \vartheta \Delta t_n = (1 - \vartheta) t_n + \vartheta t_{n+1}$, with $0 \leq \vartheta \leq 1$, be some intermediate time such that $U_{i,j}^{n+\vartheta} \approx u(r_i, z_j, t_{n+\vartheta})$ etc. Then the discretization of (2.33) reads

$$U_{i,j}^{n+1} - U_{i,j}^n = \frac{\Delta t_n}{V_{ij}} \left((AF)_{i-\frac{1}{2},j}^{u;n+\vartheta} + (AF)_{i+\frac{1}{2},j}^{u;n+\vartheta} + (AF)_{i,j-\frac{1}{2}}^{u;n+\vartheta} + (AF)_{i,j+\frac{1}{2}}^{u;n+\vartheta} \right), \quad (3.9a)$$

$$W_{i,j}^{n+1} - W_{i,j}^n = \frac{\Delta t_n}{V_{ij}} \left((AF)_{i-\frac{1}{2},j}^{w;n+\vartheta} + (AF)_{i+\frac{1}{2},j}^{w;n+\vartheta} + (AF)_{i,j-\frac{1}{2}}^{w;n+\vartheta} + (AF)_{i,j+\frac{1}{2}}^{w;n+\vartheta} \right). \quad (3.9b)$$

By Fick's law, the flow rates at the faces are given by

$$(AF)_{i-\frac{1}{2},j}^{u;n+\vartheta} = -A_{i-\frac{1}{2},j} D_{ur} \left(\frac{U_{i,j}^{n+\vartheta} - U_{i-1,j}^{n+\vartheta}}{r_i - r_{i-1}} \right), \quad (3.10a)$$

$$(AF)_{i+\frac{1}{2},j}^{u;n+\vartheta} = A_{i+\frac{1}{2},j} D_{ur} \left(\frac{U_{i+1,j}^{n+\vartheta} - U_{i,j}^{n+\vartheta}}{r_{i+1} - r_i} \right), \quad (3.10b)$$

$$(AF)_{i,j-\frac{1}{2}}^{u;n+\vartheta} = -A_{i,j-\frac{1}{2}} D_{uz} \left(\frac{U_{i,j}^{n+\vartheta} - U_{i,j-1}^{n+\vartheta}}{z_j - z_{j-1}} \right), \quad (3.10c)$$

$$(AF)_{i,j+\frac{1}{2}}^{u;n+\vartheta} = A_{i,j+\frac{1}{2}} D_{uz} \left(\frac{U_{i,j+1}^{n+\vartheta} - U_{i,j}^{n+\vartheta}}{z_{j+1} - z_j} \right), \quad (3.10d)$$

and similarly for w . Note that the unit normal for the faces $A_{i-\frac{1}{2},j}$, $A_{i,j-\frac{1}{2}}$ is (-1) and for the faces $A_{i+\frac{1}{2},j}$, $A_{i,j+\frac{1}{2}}$ is $(+1)$. For each disc unit $N = 1, \dots, N_{\text{disc}}$ the indices i, j run as

- Below the disc: $i = 1, \dots, I_{mf}$; $j = (N-1)J_{fmf} + 1, \dots, (N-1)J_{fmf} + J_f$.
- Right of the disc: $i = I_m + 1, \dots, I_{mf}$; $j = (N-1)J_{fmf} + J_f + 1, \dots, NJ_{fmf} - J_f$.
- Above the disc: $i = 1, 2, \dots, I_{mf}$; $j = NJ_{fmf} - J_f + 1, \dots, NJ_{fmf}$.

3.1.2 Discretization of the Boundary Conditions

On the top of the discs, i.e., $i = 1, 2, \dots, I_m$, $j = J =: (N-1)J_{fmf} + J_f + J_m$, and $N = 1, \dots, N_{\text{disc}}$:

$$F_{i,J-\frac{1}{2}}^{u;n+\vartheta} = -C_{\min} - C_1 f_1(W_{i,J-\frac{1}{2}}^{n+\vartheta}) + C_2 U_{i,J-\frac{1}{2}}^{n+\vartheta}, \quad (3.11a)$$

$$F_{i,J-\frac{1}{2}}^{w;n+\vartheta} = 0. \quad (3.11b)$$

On the bottom of the discs, i.e., $i = 1, 2, \dots, I_m$, $j = J =: (N-1)J_{fmf} + J_f$, and $N = 1, \dots, N_{\text{disc}}$, where a photon may be observed:

$$F_{i,J+\frac{1}{2}}^{u;n+\vartheta} = -C_{\min} - C_1 f_1(W_{i,J+\frac{1}{2}}^{n+\vartheta}) + C_2 U_{i,J+\frac{1}{2}}^{n+\vartheta} + \delta_{io} C_0 U_{i,J+\frac{1}{2}}^{n+\vartheta} P(r_i, t_{n+\vartheta}), \quad (3.12a)$$

$$F_{i,J+\frac{1}{2}}^{w;n+\vartheta} = 0. \quad (3.12b)$$

On the lateral face of the discs, i.e., $i = I =: I_m$, $j = (N-1)J_{fmf} + J_f + 1, \dots, NJ_{fmf} - J_f$, and $N = 1, \dots, N_{\text{disc}}$:

$$F_{I+\frac{1}{2},j}^{u;n+\vartheta} = 0, \quad (3.13a)$$

$$F_{I+\frac{1}{2},j}^{w;n+\vartheta} = 0. \quad (3.13b)$$

On the lateral side of the rod, i.e., $i = I =: I_{mf}$ and $j = 1, 2, \dots, JN_{fmf}$:

$$F_{I+\frac{1}{2},j}^{u;n+\vartheta} = 0, \quad (3.14a)$$

$$F_{I+\frac{1}{2},j}^{w;n+\vartheta} = g_1(W_{I+\frac{1}{2},j}^{n+\vartheta}) - C_{\text{ratio}} g_2(U_{I+\frac{1}{2},j}^{n+\vartheta}). \quad (3.14b)$$

On the top of the rod, i.e., $i = 1, 2, \dots, I_{mf}$, and $j = J =: JN_{fmf}$:

$$F_{i,J+\frac{1}{2}}^{u;n+\vartheta} = 0, \quad (3.15a)$$

$$F_{i,J+\frac{1}{2}}^{w;n+\vartheta} = 0. \quad (3.15b)$$

On the bottom of the rod, i.e., $i = 1, 2, \dots, I_{mf}$, and $j = 1$:

$$F_{i,1-\frac{1}{2}}^{u;n+\vartheta} = 0, \quad (3.16a)$$

$$F_{i,1-\frac{1}{2}}^{w;n+\vartheta} = 0. \quad (3.16b)$$

Note: The top and bottom of the disc surface are located at faces of the grid (see Fig 3.1), which is natural for specifying fluxes there. However, we also need the values at the boundary to prescribe the boundary conditions. This is done by also assigning nodal values at the surface and storing them at some other nodes in the grid that are not in use. For example, boundary values along the bottom of the disc are stored at the nodes with $j = (N-1)J_{fmf} + J_f + 1$ (which are not in the computational domain Ω as defined in §2.2).

3.1.3 Explicit-Implicit Method

Choosing $\vartheta = 0$ in (3.9), the fluxes are evaluated at the old time t_n and therefore they are completely known. This amounts to assuming that the values of the fluxes do not change appreciably during the time interval $[t_n, t_{n+1}]$, so that the process at time t_{n+1} is still driven by the fluxes at the time t_n . The time discretization is then the standard **Forward Euler** discretization, and the new values $U_{i,j}^{n+1}$, $W_{i,j}^{n+1}$ are obtained directly by evaluating the right hand sides.

The explicit scheme for $U_{i,j}^{n+1} \approx u(r_i, z_j, t_{n+1})$, $W_{i,j}^{n+1} \approx w(r_i, z_j, t_{n+1})$ takes the form

$$U_{i,j}^0 = U_{\text{init}}(r_i, z_j), \quad W_{i,j}^0 = W_{\text{init}}(r_i, z_j), \quad (3.17)$$

where the indices i, j run over all the nodes (interior and boundary).

The update $U_{i,j}^{n+1}$, $W_{i,j}^{n+1}$ at the internal nodes are determined by

$$U_{i,j}^{n+1} = U_{i,j}^n + \frac{\Delta t_n}{V_{ij}} \left((AF)_{i-\frac{1}{2},j}^{u;n} + (AF)_{i+\frac{1}{2},j}^{u;n} + (AF)_{i,j-\frac{1}{2}}^{u;n} + (AF)_{i,j+\frac{1}{2}}^{u;n} \right), \quad (3.18a)$$

$$W_{i,j}^{n+1} = W_{i,j}^n + \frac{\Delta t_n}{V_{ij}} \left((AF)_{i-\frac{1}{2},j}^{w;n} + (AF)_{i+\frac{1}{2},j}^{w;n} + (AF)_{i,j-\frac{1}{2}}^{w;n} + (AF)_{i,j+\frac{1}{2}}^{w;n} \right), \quad (3.18b)$$

where the flow rate at the faces are as in (3.10). The values at the boundary nodes are computed **implicitly** in terms of the imposed boundary fluxes (3.11) - (3.16). The boundary values at the lower and upper disc faces $U_{i,j \pm \frac{1}{2}}^{n+1}$ and $W_{i,j \pm \frac{1}{2}}^{n+1}$ are actually stored at unused nodes as mentioned at the end of the previous section. e.g., $U_{i,J_f + \frac{1}{2}}$ is stored as U_{i,J_f+1} . They are updated as follows.

At the top face of the disc: $i = 1, 2, \dots, I_m$, $j = J := (N-1)J_{fmf} + J_f + J_m + 1$, $N = 1, \dots, N_{\text{disc}}$, from

$$F_{i,J-\frac{1}{2}}^{u;n+1} = D_{uz} \frac{U_{i,J}^{n+1} - U_{i,J-\frac{1}{2}}^{n+1}}{(z_J - z_{J-\frac{1}{2}})}, \quad (3.19a)$$

$$F_{i,J-\frac{1}{2}}^{w;n+1} = D_{wz} \frac{W_{i,J}^{n+1} - W_{i,J-\frac{1}{2}}^{n+1}}{(z_J - z_{J-\frac{1}{2}})}, \quad (3.19b)$$

and (3.11), we obtain

$$W_{i,J-\frac{1}{2}}^{n+1} = W_{i,J}^{n+1}, \quad (3.20a)$$

$$U_{i,J-\frac{1}{2}}^{n+1} = \frac{U_{i,J}^{n+1} + \left(\frac{z_J - z_{J-\frac{1}{2}}}{D_{uz}}\right) \left(C_{\min} + C_1 f_1 \left(W_{i,J-\frac{1}{2}}^{n+1}\right)\right)}{1 + \left(\frac{z_J - z_{J-\frac{1}{2}}}{D_{uz}}\right) C_2}. \quad (3.20b)$$

At the bottom face of the disc: $i = 1, 2, \dots, I_m$, $j = J := (N - 1)J_{f_m f} + J_f$, $N = 1, \dots, N_{\text{disc}}$, from

$$F_{i,J+\frac{1}{2}}^{u;n+1} = -D_{uz} \frac{U_{i,J+\frac{1}{2}}^{n+1} - U_{i,J}^{n+1}}{(z_{J+\frac{1}{2}} - z_J)}, \quad (3.21a)$$

$$F_{i,J+\frac{1}{2}}^{w;n+1} = -D_{wz} \frac{W_{i,J+\frac{1}{2}}^{n+1} - W_{i,J}^{n+1}}{(z_{J+\frac{1}{2}} - z_J)}, \quad (3.21b)$$

and (3.12), we have

$$W_{i,J+\frac{1}{2}}^{n+1} = W_{i,J}^{n+1}, \quad (3.22a)$$

$$U_{i,J+\frac{1}{2}}^{n+1} = \frac{U_{i,J}^{n+1} + \left(\frac{z_{J+\frac{1}{2}} - z_J}{D_{uz}}\right) \left(C_{\min} + C_1 f_1 \left(W_{i,J+\frac{1}{2}}^{n+1}\right)\right)}{1 + \left(\frac{z_{J+\frac{1}{2}} - z_J}{D_{uz}}\right) [C_2 + \delta_{io} C_0 P(r_i, t_n - t_{\text{on}})]}. \quad (3.22b)$$

At the lateral surface of the rod: $i = I := I_m f$; $j = 1, 2, \dots, N_{\text{disc}} J_{f_m f}$, from

$$F_{I+\frac{1}{2},j}^{u;n+1} = -D_{ur} \frac{U_{I+\frac{1}{2},j}^{n+1} - U_{I,j}^{n+1}}{r_{I+\frac{1}{2}} - r_I}, \quad (3.23a)$$

$$F_{I+\frac{1}{2},j}^{w;n+1} = -D_{wr} \frac{W_{I+\frac{1}{2},j}^{n+1} - W_{I,j}^{n+1}}{r_{I+\frac{1}{2}} - r_I}, \quad (3.23b)$$

(3.14), the definition of the functions g_1 from (2.36) and the safe quadratic formula from [43], we have

$$U_{I+\frac{1}{2},j}^{n+1} = U_{I,j}^{n+1}, \quad (3.24a)$$

$$W_{I+\frac{1}{2},j}^{n+1} = \frac{C}{Q}, \quad Q = \frac{1}{2} \left(B + \text{sign}(B) \sqrt{B^2 + 4C} \right), \quad (3.24b)$$

where

$$\begin{aligned} B &= 1 - W_{I,j}^{n+1} + \left(\frac{r_{I+\frac{1}{2}} - r_I}{D_{wr}} \right) \left[1 - C_{\text{ratio}} g_2 \left(U_{I+\frac{1}{2},j}^{n+1} \right) \right], \\ C &= \left(\frac{r_{I+\frac{1}{2}} - r_I}{D_{wr}} \right) C_{\text{ratio}} g_2 \left(U_{I+\frac{1}{2},j}^{n+1} \right) + W_{I,j}^{n+1}. \end{aligned}$$

At the top of the rod: $i = 1, 2, \dots, I_{mf}$; $j = J := N_{\text{disc}} J_{fmf}$, from (3.15),

$$U_{i,J+\frac{1}{2}}^{n+1} = U_{i,J}^{n+1}, \quad (3.25a)$$

$$W_{i,J+\frac{1}{2}}^{n+1} = W_{i,J}^{n+1}. \quad (3.25b)$$

At the bottom of the rod: $i = 1, 2, \dots, I_{mf}$; $j = 1$, from (3.16),

$$U_{i,1-\frac{1}{2}}^{n+1} = U_{i,1}^{n+1}, \quad (3.26a)$$

$$W_{i,1-\frac{1}{2}}^{n+1} = W_{i,1}^{n+1}. \quad (3.26b)$$

A Note on Coupling: The system of parabolic PDEs given by (2.33) is coupled via the nonlinear boundary conditions (2.34). An explicit time update algorithm would simply use old time level information to make all updates and the order of computation is irrelevant. Since we are treating the nonhomogeneous boundary conditions **implicitly**, a proper algorithm to link the two problems must be devised. To link the coupled system properly, we update $U_{i,j}^{n+1}$ and $W_{i,j}^{n+1}$ in the order described in (3.20), (3.22), (3.24).

3.1.4 1D Longitudinal Model

Consider a rod of length H with periodically varying cross sectional area. As in the full model, let $N_{\text{disc}} \in \mathbb{N}$, $J_f \in \mathbb{N}$ and $J_m \in \mathbb{N}$ be some mesh dimensioning

numbers. Let $J_{mf} = J_m + J_f$, $J_{fmf} = J_f + J_m + J_f$, $JN_{fmf} = N_{\text{disc}} \cdot J_{fmf}$. We set up $\mathcal{M} = (V_j)_{j=1,2,\dots,JN_{fmf}}$ a one dimensional (z) mesh for the axially symmetric and radially uniform problem in Ω by subdividing the length $[0, \epsilon]$ into J_m subintervals, and $[0, \delta]$ into $2J_f$ subintervals, as before. We assign one node to each of these control volumes V_j .

Let $\Delta z_0 = 0$, $\Delta z_{JN_{fmf}+1} = 0$. For $j = 1, \dots, JN_{fmf}$, $z_{\frac{1}{2}} = 0$, $z_{j+\frac{1}{2}} = z_{j-\frac{1}{2}} + \Delta z_j$, (so that $z_{J_f+\frac{1}{2}} = \frac{\delta}{2}$, $z_{J_{fmf}+\frac{1}{2}} = \delta + \epsilon, \dots$, and $z_{JN_{fmf}+\frac{1}{2}} = H$), and the volume V_j is given by

$$V_j = A_{j-\frac{1}{2}} \cdot \Delta z_j, \quad j = 1, 2, \dots, JN_{fmf}, \quad (3.27)$$

where $A_{j-\frac{1}{2}}$, the surface area of the face $z_{j-\frac{1}{2}}$, is given by

$$A_{j-\frac{1}{2}} = \begin{cases} \pi R_{\text{rod}}^2, & \text{for } 0 \leq j \leq J_f, J_{mf} + 1 \leq j \leq J_{fmf}, \\ \pi (R_{\text{rod}}^2 - R_{\text{disc}}^2), & \text{for } J_f + 1 \leq j \leq J_{mf} + 2. \end{cases} \quad (3.28)$$

Denote U_j^n, W_j^n the mean values of u, w over V_j ; the values U_j^n, W_j^n are numerical approximations of $u(x_j, t_n)$ and $w(x_j, t_n)$ respectively.

Integrating (2.37) and (2.38) over the control volume V_j and time interval $[t_n, t_n + \Delta t_n]$, and using the Explicit-Implicit strategy as in the full model, we obtain the following scheme

$$U_j^{n+1} = U_j^n + \frac{\Delta t_n}{V_j} \left((AF)_{j-\frac{1}{2}}^{u;n} + (AF)_{j+\frac{1}{2}}^{u;n} \right), \quad (3.29a)$$

$$W_j^{n+1} = W_j^n + \frac{\Delta t_n}{V_j} \left((AF)_{j-\frac{1}{2}}^{w;n} + (AF)_{j+\frac{1}{2}}^{w;n} \right) + \Delta t_n (C_{\text{ex}} g_1(W_j^{n+1}) - C_{\text{cG}} g_1(U_j^{n+1})), \quad (3.29b)$$

for $j = 1, 2, \dots, JN_{fmf}$. The nonzero flux boundary condition (2.38b) takes the form

$$F_{J_f+\frac{1}{2}}^{u;n+1} = -C_{\text{min}} - C_1 f_1(W_{J_f+\frac{1}{2}}^{n+1}) + C_2 U_{J_f+\frac{1}{2}}^{n+1} + \delta_{i,i_0} C_0 P U_{J_f+\frac{1}{2}}^{n+1}, \quad (3.30a)$$

$$F_{J_{mf}+\frac{1}{2}}^{u;n+1} = C_{\text{min}} + C_1 f_1(W_{J_{mf}+\frac{1}{2}}^{n+1}) - C_2 U_{J_{mf}+\frac{1}{2}}^{n+1}. \quad (3.30b)$$

The flow rates through all but the boundary faces (i.e., for $j \neq J_f + 1$, and $j \neq J_{mf} + 1$) are computed by the relations

$$(AF)_{j-\frac{1}{2}}^{u;n} = -A_{j-\frac{1}{2}} D_{uz} \left(\frac{U_j^n - U_{j-1}^n}{z_j - z_{j-1}} \right), \quad (AF)_{j+\frac{1}{2}}^{u;n} = A_{j+\frac{1}{2}} D_{uz} \left(\frac{U_{j+1}^n - U_j^n}{z_{j+1} - z_j} \right), \quad (3.31)$$

and similarly for w . Note that the unit normal for the face $A_{j-\frac{1}{2}}$ is (-1) and for the face $A_{j+\frac{1}{2}}$ is $(+1)$. The boundary values $U_{J_f+\frac{1}{2}}$, $W_{J_f+\frac{1}{2}}$, $U_{J_{mf}+\frac{1}{2}}$ and $W_{J_{mf}+\frac{1}{2}}$ are obtained by solving

$$\pi R_{\text{rod}}^2 \cdot \left(-D_{uz} \left(\frac{U_{J_f+\frac{1}{2}}^n - U_{J_f}^n}{z_{J_f+\frac{1}{2}} - z_{J_f}} \right) \right) = \pi R_{\text{disc}}^2 \cdot F_{J_f+\frac{1}{2}}^{u;n+1} + (AF)_{J_f+\frac{1}{2}}^{u;n}, \quad (3.32a)$$

$$\pi R_{\text{rod}}^2 \cdot \left(-D_{wz} \left(\frac{W_{J_f+\frac{1}{2}}^n - W_{J_f}^n}{z_{J_f+\frac{1}{2}} - z_{J_f}} \right) \right) = (AF)_{J_f+\frac{1}{2}}^{w;n}, \quad (3.32b)$$

$$\pi R_{\text{rod}}^2 \cdot \left(-D_{uz} \left(\frac{U_{J_{mf}+1}^n - U_{J_{mf}+\frac{1}{2}}^n}{z_{J_{mf}+1} - z_{J_{mf}+\frac{1}{2}}} \right) \right) = \pi R_{\text{disc}}^2 \cdot F_{J_{mf}+\frac{1}{2}}^{u;n+1} + (AF)_{J_{mf}+\frac{1}{2}}^{u;n}, \quad (3.32c)$$

$$\pi R_{\text{rod}}^2 \cdot \left(-D_{wz} \left(\frac{W_{J_{mf}+1}^n - W_{J_{mf}+\frac{1}{2}}^n}{z_{J_{mf}+1} - z_{J_{mf}+\frac{1}{2}}} \right) \right) = (AF)_{J_{mf}+\frac{1}{2}}^{w;n}. \quad (3.32d)$$

3.2 Homogenized Model

Let $I_p \in \mathbb{N}$, $J_p \in \mathbb{N}$ and $M_p \in \mathbb{N}$. We set up a three dimensional (r, z, θ) mesh $\mathcal{M} = (V_{i,j,m})_{i=1,2,\dots,I_p; j=1,2,\dots,J_p; m=1,2,\dots,M_p}$ of the cylindrical domain $0 < r < R_{\text{disc}}$, $0 < z < H$, $0 \leq \theta < 2\pi$ with $I_p \times J_p \times M_p$ nodes.

Let us consider the uniform grid with $\Delta r = \frac{R_{\text{disc}}}{I_p}$, $\Delta z = \frac{H}{J_p}$, and $\Delta \theta = \frac{2\pi}{M_p}$. For $i = 1, \dots, I_p$, let $r_{1/2} = 0$, $r_{i+1/2} = r_{i-1/2} + \Delta r$, $r_{I_p+1/2} = R_{\text{disc}}$, and for $j = 1, \dots, J_p$, let $z_{1/2} = 0$, $z_{j+1/2} = z_{j-1/2} + \Delta z$ and $z_{J_p+1/2} = H$, and for $m = 2, \dots, M_p - 1$, let $\theta_{1/2} = \theta_{M_p+1/2} = 2\pi - \frac{\Delta \theta}{2}$, $\theta_{\frac{3}{2}} = \frac{\Delta \theta}{2}$, $\theta_{m+1/2} = \theta_{m-1/2} + \Delta \theta$, and the control volume

$$V_{i,j,m} = \int_{r_{i-1/2}}^{r_{i+1/2}} \int_{z_{j-1/2}}^{z_{j+1/2}} \int_{\theta_{m-1/2}}^{\theta_{m+1/2}} r \, d\theta \, dz \, dr. \quad (3.33)$$

The areas of the radial ($Ar_{i-1/2,j,m}$), axial ($Az_{i,j-1/2,m}$) and angular ($A\theta_{i,j,m-1/2}$) faces are respectively

$$\int_{z_{j-1/2}}^{z_{j+1/2}} \int_{\theta_{m-1/2}}^{\theta_{m+1/2}} r \, d\theta \, dz, \quad \int_{r_{i-1/2}}^{r_{i+1/2}} \int_{\theta_{m-1/2}}^{\theta_{m+1/2}} r \, d\theta \, dr, \quad \text{and} \quad \int_{r_{i-1/2}}^{r_{i+1/2}} \int_{z_{j-1/2}}^{z_{j+1/2}} dz \, dr. \quad (3.34)$$

Let $(r_i)_{i=0,1,\dots,I_p+1}$, $(z_j)_{j=0,1,\dots,J_p+1}$, and $(\theta_m)_{m=0,1,\dots,M_p+1}$, such that

$$\begin{aligned} r_{i-1/2} < r_i < r_{i+1/2}, & \quad \text{for } i = 1, 2, \dots, I_p, \quad r_0 = 0, \quad r_{I_p+1} = R_{\text{disc}}, \\ z_{j-1/2} < z_j < z_{j+1/2}, & \quad \text{for } j = 1, 2, \dots, J_p, \quad z_0 = 0, \quad z_{J_p+1} = H, \\ \theta_{m-1/2} < \theta_m < \theta_{m+1/2}, & \quad \text{for } m = 1, 2, \dots, M_p, \quad \theta_0 = \theta_{M_p}, \quad \theta_1 = \theta_{M_p+1} = 0, \end{aligned} \quad (3.35)$$

and let $x_{i,j,m} = (r_i, z_j, \theta_m)$, for $i = 1, 2, \dots, I_p$; $j = 1, 2, \dots, J_p$; $m = 1, 2, \dots, M_p$. We also define $I_b = I_p + 1$, $J_b = J_p + 1$, $M_b = M_p + 1$ for the indices at the boundary nodes.

Let \mathcal{N}_h denote the set of all nodes in the mesh \mathcal{M} . Denote

$$\{U_{i,j,m}^n, W_{i,j,m}^n : (i, j, m) \in \mathcal{N}_h\},$$

the mean values of u , w over $V_{i,j,m}$; the values $U_{i,j,m}^n$, $W_{i,j,m}^n$ are numerical approximations of $u(x_{i,j,m}, t_n)$ and $w(x_{i,j,m}, t_n)$ respectively.

Time discretization is performed with variable time steps. Let $T > 0$ be the time, $\{t_0, \dots, t_{N_{\max}}\}$, a partition of $[0, T]$, and $\Delta t_n = t_{n+1} - t_n$ the time step size.

3.2.1 Discretization Based on PDEs

In order to obtain the numerical scheme, we integrate formally equations (2.39a) and (2.39b) over each control volume $V_{i,j,m}$ and time interval $[t_n, t_n + \Delta t_n]$, $n = 0, 1, \dots, N_{\max}$

$$\int_{V_{i,j,m}} (u(t_{n+1}) - u(t_n)) \, dV + \int_{t_n}^{t_n + \Delta t_n} \int_{\partial V_{i,j,m}} \Phi_u \cdot \mathbf{n}_{i,j,m} \, dA \, dt$$

$$= \int_{t_n}^{t_n+\Delta t_n} \int_{\partial V_{i,j,m}} S_{\min} + S_1 f_1(w) - S_2 u - \delta_{z_0} S_0 u P(r, t) dV dt, \quad (3.36a)$$

$$\int_{V_{i,j,m}} (w(t_{n+1}) - w(t_n)) dV + \int_{t_n}^{t_n+\Delta t_n} \int_{\partial V_{i,j,m}} \Phi_w \cdot \mathbf{n}_{i,j,m} dA dt = 0. \quad (3.36b)$$

where $\mathbf{n}_{i,j,m}$ is the outward unit normal to the control volume $V_{i,j,m}$. Let us define $t_{n+\vartheta} := t_n + \vartheta \Delta t_n = (1 - \vartheta) t_n + \vartheta t_{n+1}$, with $0 \leq \vartheta \leq 1$ to be some intermediate time. Then (3.36a), (3.36b) takes the form:

$$\begin{aligned} & \frac{1}{\Delta t_n} \int_{V_{i,j,m}} (u(t_{n+1}) - u(t_n)) dV + \int_{\partial V_{i,j,m}} \Phi_u(t_{n+\vartheta}) \cdot \mathbf{n}_{i,j,m} dA dt \\ &= \int_{\partial V_{i,j,m}} S_{\min} + S_1 f_1(w(t_{n+\vartheta})) - S_2 u(t_{n+\vartheta}) - \delta_{z_0} S_0 u(t_{n+\vartheta}) P(r, (t_{n+\vartheta})) dV, \end{aligned} \quad (3.37a)$$

$$\frac{1}{\Delta t_n} \int_{V_{i,j,m}} (w(t_{n+1}) - w(t_n)) dV + \int_{\partial V_{i,j,m}} \Phi_w(t_{n+\vartheta}) \cdot \mathbf{n}_{i,j,m} dA = 0. \quad (3.37b)$$

Discrete (r, θ) Problem: Since the system of equations (2.39a) and (2.39b) has z as a parameter, we discretize this as a two dimensional problem (r, θ) for each z_j . The discretized versions of (2.39a) and (2.39b) take the form

$$\begin{aligned} U_{i,j,m}^{n+1} &= U_{i,j,m}^n + \frac{\Delta t_n}{V_{i,m}} \left[(A\Phi)_{i-1/2,j,m}^{u;n+\vartheta} + (A\Phi)_{i+1/2,j,m}^{u;n+\vartheta} + (A\Phi)_{i,j,m-1/2}^{u;n+\vartheta} \right. \\ &\quad \left. + (A\Phi)_{i,j,m+1/2}^{u;n+\vartheta} \right] + \Delta t_n \left[S_1 f_1(W_{i,j,m}^{n+\vartheta}) - S_2 U_{i,j,m}^{n+\vartheta} - \delta_{j_0} S_0 P(r_i, t_{n+1}) U_{i,j,m}^{n+\vartheta} \right], \end{aligned} \quad (3.38a)$$

$$\begin{aligned} W_{i,j,m}^{n+1} &= W_{i,j,m}^n + \frac{\Delta t_n}{V_{i,m}} \left[(A\Phi)_{i-1/2,j,m}^{w;n+\vartheta} + (A\Phi)_{i+1/2,j,m}^{w;n+\vartheta} \right. \\ &\quad \left. + (A\Phi)_{i,j,m-1/2}^{w;n+\vartheta} + (A\Phi)_{i,j,m+1/2}^{w;n+\vartheta} \right]. \end{aligned} \quad (3.38b)$$

for $i = 1, \dots, I_p$, $j = 1, \dots, j_0, \dots, J_p$, $m = 1, \dots, M_p$, $n = 0, 1, \dots, N_{\max}$, where j_0 denotes light-activated disc(s). The flow rates are given by

$$(A\Phi)_{i-1/2,j,m}^{u;n+\vartheta} = -\alpha_{i-1/2,m} D_{ur} \left(\frac{U_{i,j,m}^{n+\vartheta} - U_{i-1,j,m}^{n+\vartheta}}{r_i - r_{i-1}} \right), \quad (3.39a)$$

$$\begin{aligned}
& i = 1, \dots, I_p + 1, j = 1, \dots, J_p, m = 1, \dots, M_p, \\
(A\Phi)_{i+1/2,j,m}^{u;n+\vartheta} &= \alpha_{i+1/2,m} D_{ur} \left(\frac{U_{i+1,j,m}^{n+\vartheta} - U_{i,j,m}^{n+\vartheta}}{r_{i+1} - r_i} \right), \tag{3.39b}
\end{aligned}$$

$$\begin{aligned}
& i = 1, \dots, I_p + 1, j = 1, \dots, J_p, m = 1, \dots, M_p, \\
(A\Phi)_{i,j,m-1/2}^{u;n+\vartheta} &= -\alpha_{i,m-1/2} \frac{D_{u\theta}}{r_i} \left(\frac{U_{i,j,m}^{n+\vartheta} - U_{i,j,m-1}^{n+\vartheta}}{\theta_m - \theta_{m-1}} \right), \tag{3.39c} \\
& i = 1, \dots, I_p, j = 1, \dots, J_p, m = 1, \dots, M_p + 1,
\end{aligned}$$

$$\begin{aligned}
(A\Phi)_{i,j,m+1/2}^{u;n} &= \alpha_{i,m+1/2} \frac{D_{u\theta}}{r_i} \left(\frac{U_{i,j,m+1}^{n+\vartheta} - U_{i,j,m}^{n+\vartheta}}{\theta_{m+1} - \theta_m} \right), \tag{3.39d} \\
& i = 1, \dots, I_p, j = 1, \dots, J_p, m = 1, \dots, M_p + 1,
\end{aligned}$$

and similar expressions for w , where

$$\alpha_{i-1/2,m} = r_{i-1/2} \Delta\theta, \quad \alpha_{i,m-1/2} = \Delta r, \tag{3.40}$$

are the 2-dimensional (r, θ) “areas”, and

$$V_{i,m} = A_{i,j-1/2,m} = \frac{1}{2} (r_{i+1/2}^2 - r_{i-1/2}^2) \Delta\theta, \tag{3.41}$$

is the 2-dimensional (r, θ) “volumes”. Note that the unit normal for the faces $\alpha_{i-1/2,m}$, $\alpha_{i,m-1/2}$ is (-1) and for the faces $\alpha_{i+1/2,m}$, $\alpha_{i,m+1/2}$ is $(+1)$.

The discrete boundary conditions (2.41) take the form

$$\begin{aligned}
\Phi_{1/2,j,m}^{u;n} &= 0, & \Phi_{1/2,j,m}^{w;n} &= 0, \\
U_{i,j,0}^n &:= U_{i,j,M_p}^n, & W_{i,j,0}^n &:= W_{i,j,M_p}^n, \\
U_{i,j,1}^n &:= U_{i,j,M_p+1}^n, & W_{i,j,1}^n &:= W_{i,j,M_p+1}^n, \\
U_{I_b,j,m}^n &= \widehat{U}_{I_b,j,m}^n, & W_{I_p+1,j,m}^n &= \widehat{W}_{I_p+1,j,m}^n,
\end{aligned} \tag{3.42}$$

where $\widehat{U}_{I_b,j,m}^n$ and $\widehat{W}_{I_b,j,m}^n$ are to be supplied from the solution of the (z, θ) problem.

Discrete (z, θ) Problem: Since the system of equations (2.42a) and (2.42b) are defined only on the lateral surface of the cylinder, we discretize this as a two dimensional (z, θ) problem. The discretized versions of (2.42a) and (2.42b) take the form

$$\begin{aligned} \widehat{U}_{I_b, j, m}^{n+1} = \widehat{U}_{I_b, j, m}^n + \frac{\Delta t_n}{V_{j, m}} & \left[(A\Psi)_{I_b, j-1/2, m}^{\widehat{u}; n+\vartheta} + (A\Psi)_{I_b, j+1/2, m}^{\widehat{u}; n+\vartheta} + (A\Psi)_{I_b, j, m-1/2}^{\widehat{u}; n+\vartheta} \right. \\ & \left. + (A\Psi)_{I_b, j, m+1/2}^{\widehat{u}; n+\vartheta} \right] + \Delta t_n \left[\frac{(b + \delta_{j_0} b_0)}{\alpha_{I_b, m}} (A\Phi)_{I_b, j, m}^{u; n+\vartheta} \right], \end{aligned} \quad (3.43a)$$

$$\begin{aligned} \widehat{W}_{I_b, j, m}^{n+1} = \widehat{W}_{I_b, j, m}^n + \frac{\Delta t_n}{V_{j, m}} & \left[(A\Psi)_{I_b, j-1/2, m}^{\widehat{w}; n+\vartheta} + (A\Psi)_{I_b, j+1/2, m}^{\widehat{w}; n+\vartheta} + (A\Psi)_{I_b, j, m-1/2}^{\widehat{w}; n+\vartheta} \right. \\ & \left. + (A\Psi)_{I_b, j, m+1/2}^{\widehat{w}; n+\vartheta} \right] + \Delta t_n \left[\frac{(b + \delta_{j_0} b_0)}{\alpha_{I_b, m}} (A\Phi)_{I_b, j, m}^{w; n+\vartheta} \right. \\ & \left. + S_{\text{ratio}} g_2(\widehat{U}_{I_b, j, m}^{n+\vartheta}) - \frac{1}{R_0} g_1(\widehat{W}_{I_b, j, m}^{n+\vartheta}) \right], \end{aligned} \quad (3.43b)$$

for $j = 1, 2, \dots, j_0, \dots, J_p$, $m = 1, 2, \dots, M_p$, $n = 0, 1, \dots, N_{\text{max}}$, where j_0 denotes light-activated disc(s). The flow rates are given by

$$(A\Psi)_{I_b, j-1/2, m}^{\widehat{u}; n+\vartheta} = -\beta_{j-1/2, m} D_{uz} \left(\frac{\widehat{U}_{I_b, j, m}^{n+\vartheta} - \widehat{U}_{I_b, j-1, m}^{n+\vartheta}}{z_j - z_{j-1}} \right), \quad (3.44a)$$

$$j = 1, \dots, J_p + 1, m = 1, \dots, M_p,$$

$$(A\Psi)_{I_b, j+1/2, m}^{\widehat{u}; n+\vartheta} = \beta_{j+1/2, m} D_{uz} \left(\frac{\widehat{U}_{I_b, j+1, m}^{n+\vartheta} - \widehat{U}_{I_b, j, m}^{n+\vartheta}}{z_{j+1} - z_j} \right), \quad (3.44b)$$

$$j = 1, \dots, J_p + 1, m = 1, \dots, M_p,$$

$$(A\Psi)_{I_b, j, m-1/2}^{\widehat{u}; n+\vartheta} = -\beta_{j, m-1/2} \frac{D_{u\theta}}{r_{I_b}} \left(\frac{\widehat{U}_{I_b, j, m}^{n+\vartheta} - \widehat{U}_{I_b, j, m-1}^{n+\vartheta}}{\theta_m - \theta_{m-1}} \right), \quad (3.44c)$$

$$j = 1, \dots, J_p, m = 1, \dots, M_p + 1,$$

$$(A\Psi)_{I_b, j, m+1/2}^{\widehat{u}; n} = \beta_{j, m+1/2} \frac{D_{u\theta}}{r_{I_b}} \left(\frac{\widehat{U}_{I_b, j, m+1}^n - \widehat{U}_{I_b, j, m}^n}{\theta_{m+1} - \theta_m} \right), \quad (3.44d)$$

$$j = 1, \dots, J_p, m = 1, \dots, M_p + 1,$$

and similar expressions for \widehat{w} , where

$$\beta_{j-1/2,m} = r_{I_b} \Delta\theta, \quad \beta_{j,m-1/2} = \Delta z \quad (3.45)$$

are the 2-dimensional (z, θ) "areas" and

$$V_{j,m} = A_{I_p+1/2,j,m} = r_{I_b} \Delta z \Delta\theta \quad (3.46)$$

is the 2-dimensional (z, θ) "volumes". Note that the unit normal for the faces $\beta_{j-1/2,m}$, $\beta_{j,m-1/2}$ is (-1) and for the faces $\beta_{j+1/2,m}$, $\beta_{j,m+1/2}$ is (+1).

The flow rates $(A\Phi)_{I_b,j,m}^{w;n+\vartheta}$ and $(A\Phi)_{I_b,j,m}^{w;n+\vartheta}$ are as in (3.39b)-(3.39e). The discrete boundary conditions (2.44) take the form

$$\begin{aligned} \Psi_{I_b,1/2,m}^{\widehat{u};n} &= 0, & \Psi_{I_b,j+1/2,m}^{\widehat{u};n} &= 0, \\ \Psi_{I_b,1/2,m}^{\widehat{w};n} &= 0, & \Psi_{I_b,j+1/2,m}^{\widehat{w};n} &= 0, \\ \widehat{U}_{I_b,j,0}^n &:= \widehat{U}_{I_b,j,M_p}^n, & \widehat{W}_{I_b,j,0}^n &:= \widehat{W}_{I_b,j,M_p}^n, \\ \widehat{U}_{I_b,j,1}^n &:= \widehat{U}_{I_b,j,M_p+1}^n, & \widehat{W}_{I_b,j,1}^n &:= \widehat{W}_{I_b,j,M_p+1}^n. \end{aligned} \quad (3.47)$$

An explicit time update algorithm would simply use old time level information to make all updates. It is appropriate when there is no time dependent source terms or time dependent boundary conditions. It is not appropriate for the problems like (2.39a), (2.39b), (2.42a), (2.42b), with the nonlinear source terms. For this reason we have also developed Explicit-Implicit and Fully Implicit schemes. We assume that all quantities are known at the time level n . When more than one conservation law is involved in the coupling, an algorithm properly linking the equations must be devised. For an explicit scheme the order of the solution of each equation is irrelevant because only old time level data are used but for the Explicit-Implicit and Fully

Implicit Schemes the order of solution is very important. The next three subsections will describe in detail the algorithms for the system of coupled parabolic partial differential equations and the boundary conditions given by (2.39a), (2.39b), (2.41), (2.42a), (2.42b) and (2.44).

Explicit-Implicit Scheme

Choosing $\vartheta = 0$ for the fluxes and $\theta = 1$ for the source terms in (3.38), (3.43), and using the definition of the functions g_1 from (2.36) and after doing some algebra in (3.38), (3.43), we get the following Explicit-Implicit scheme

$$\begin{aligned}
U_{i,j,m}^{n+1} = & \left\{ U_{i,j,m}^n + \frac{\Delta t_n}{V_{i,m}} \left[(A\Phi)_{i-1/2,j,m}^{u;n} + (A\Phi)_{i+1/2,j,m}^{u;n} + (A\Phi)_{i,j,m-1/2}^{u;n} \right. \right. \\
& \left. \left. + (A\Phi)_{i,j,m+1/2}^{u;n} \right] + \Delta t_n S_1 f_1(W_{i,j,m}^{n+1}) \right\} \\
& / [1 + \Delta t_n (S_2 + \delta_{j_0} S_0 P(r_i, t_{n+1}))], \tag{3.48a}
\end{aligned}$$

$$\begin{aligned}
W_{i,j,m}^{n+1} = & W_{i,j,m}^n + \frac{\Delta t_n}{V_{i,m}} \left[(A\Phi)_{i-1/2,j,m}^{w;n} + (A\Phi)_{i+1/2,j,m}^{w;n} + (A\Phi)_{i,j,m-1/2}^{w;n} \right. \\
& \left. + (A\Phi)_{i,j,m+1/2}^{w;n} \right], \tag{3.48b}
\end{aligned}$$

$$\begin{aligned}
\widehat{U}_{I_b,j,m}^{n+1} = & \widehat{U}_{I_b,j,m}^n + \frac{\Delta t_n}{V_{j,m}} \left[(A\Psi)_{I_b,j-1/2,m}^{\widehat{u};n} + (A\Psi)_{I_b,j+1/2,m}^{\widehat{u};n} + (A\Psi)_{I_b,j,m-1/2}^{\widehat{u};n} \right. \\
& \left. + (A\Psi)_{I_b,j,m+1/2}^{\widehat{u};n} \right] + \Delta t_n \frac{(b + \delta_{j_0} b_0)}{\alpha_{I_b,m}} (A\Phi)_{I_b,j,m}^{u;n+1}, \tag{3.48c}
\end{aligned}$$

$$\widehat{W}_{I_b,j,m}^{n+1} = \frac{C}{Q}, \quad Q = \frac{1}{2} \left(B + \text{sign}(B) \sqrt{B^2 + 4C} \right), \tag{3.48d}$$

with

$$C = \widehat{W}_{I_b,j,m}^n + \frac{\Delta t_n}{V_{j,m}} \left[(A\Psi)_{I_b,j-1/2,m}^{\widehat{u};n} + (A\Psi)_{I_b,j+1/2,m}^{\widehat{u};n} + (A\Psi)_{I_b,j,m-1/2}^{\widehat{u};n} \right]$$

$$+(A\Psi)_{I_b,j,m+1/2}^{\widehat{w};n} \Big] + \Delta t_n \left[\frac{(b + \delta_{j_0} b_0)}{\alpha_{I_b,m}} (A\Phi)_{I_b,j,m}^{w;n+1} + S_{\text{ratio}} g_2(\widehat{U}_{I_b,j,m}^{n+1}) \right], \quad (3.49)$$

$$B = 1 + \frac{\Delta t_n}{R_0} - C, \quad (3.50)$$

for $i = 1, \dots, I_p$, $j = 1, \dots, j_0, \dots, J_p$, $m = 1, \dots, M_p$, $n = 0, 1, \dots, N_{\text{max}}$, where j_0 denotes light-activated disc(s).

Algorithm: For $q = 0, 1, \dots$

- Step 1. Compute $(A\Phi)_{I_p+1/2,j,m}^{u;n}$ from (3.39b)-(3.39e) (with currently available value of $\widehat{U}_{I_b,j,m}^n$) and take $(A\Phi)_{I_p+1/2,j,m}^{u;n+1} = (A\Phi)_{I_p+1/2,j,m}^{u;n}$ in (3.48c); find $\widehat{U}_{I_b,j,m}^{n+1}$, and set $\widehat{U}_{I_b,j,m}^{q+1} = \widehat{U}_{I_b,j,m}^{n+1}$.
- Step 2. Compute $(A\Phi)_{I_p+1/2,j,m}^{w;n}$ similarly as in (3.39b)-(3.39e) (with currently available value of $\widehat{W}_{I_b,j,m}^n$) and take $(A\Phi)_{I_p+1/2,j,m}^{w;n+1} = (A\Phi)_{I_p+1/2,j,m}^{w;n}$ and $\widehat{U}_{I_b,j,m}^{n+1} = \widehat{U}_{I_b,j,m}^{q+1}$ in (3.55); find $\widehat{W}_{I_b,j,m}^{n+1}$, and set $\widehat{W}_{I_b,j,m}^{q+1} = \widehat{W}_{I_b,j,m}^{n+1}$.
- Step 3. Take $W_{I_b,j,m}^n = \widehat{W}_{I_b,j,m}^{q+1}$, find $W_{i,j,m}^{n+1}$ from (3.48b) for each j , and set $W_{i,j,m}^{q+1} = W_{i,j,m}^{n+1}$.
- Step 4. Take $U_{I_b,j,m}^n = \widehat{U}_{I_b,j,m}^{q+1}$, $W_{I_b,j,m}^n = \widehat{W}_{I_b,j,m}^{q+1}$, find $U_{i,j,m}^{n+1}$ from (3.48a), for each j , and set $U_{i,j,m}^{q+1} = U_{i,j,m}^{n+1}$.
- Step 5. Test the convergence of the iterative sequences $\{U^q\}$, $\{W^q\}$, $\{\widehat{U}^q\}$, $\{\widehat{W}^q\}$ with some suitable norms (we used sup-norm), set $q = q + 1$, and repeat the steps 1-5 until convergence!
- Step 6. Set $\widehat{U}_{I_b,j,m}^{n+1} = \widehat{U}_{I_b,j,m}^{q+1}$, $\widehat{W}_{I_b,j,m}^{n+1} = \widehat{W}_{I_b,j,m}^{q+1}$, $U_{i,j,m}^{n+1} = U_{i,j,m}^{q+1}$, $W_{i,j,m}^{n+1} = W_{i,j,m}^{q+1}$, take a time step (time = time + Δt_n) and go to step 1.

Fully Implicit Scheme

Choosing $\vartheta = 1$ in (3.38a), (3.38b), (3.43a) and (3.43b), we get the following fully implicit scheme: For each $n = 1, 2, \dots, N_{\max}$, for each $i = 1, 2, \dots, I_p$, for each $j = 1, 2, \dots, j_o, \dots, J_p$, where j_o denotes light-activated disc(s), and for each $m = 1, 2, \dots, M_p$,

$$\begin{aligned} & A_{i,m}^u U_{i-1,j,m}^{n+1} + A_{i+1,m}^u U_{i+1,j,m}^{n+1} - D_{i,m}^u U_{i,j,m}^{n+1} + B_{i,m}^u U_{i,j,m-1}^{n+1} + B_{i,m+1}^u U_{i,j,m+1}^{n+1} \\ &= -\frac{V_{i,m}}{\Delta t_n} (U_{i,j,m}^n + \Delta t_n S_1 f_1(W_{i,j,m}^{n+1})), \end{aligned} \quad (3.51a)$$

$$\begin{aligned} & A_{i,m}^w W_{i-1,j,m}^{n+1} + A_{i+1,m}^w W_{i+1,j,m}^{n+1} - D_{i,m}^w W_{i,j,m}^{n+1} + B_{i,m}^w W_{i,j,m-1}^{n+1} + B_{i,m+1}^w W_{i,j,m+1}^{n+1} \\ &= -\frac{V_{i,m}}{\Delta t_n} U_{i,j,m}^n, \end{aligned} \quad (3.51b)$$

$$\begin{aligned} & \hat{A}_{j,m}^u \hat{U}_{I_b,j-1,m}^{n+1} + \hat{A}_{j+1,m}^u \hat{U}_{I_b,j+1,m}^{n+1} - \hat{D}_{j,m}^u \hat{U}_{I_b,j,m}^{n+1} + \hat{B}_{j,m}^u \hat{U}_{I_b,j,m-1}^{n+1} + \hat{B}_{j,m+1}^u \hat{U}_{I_b,j,m+1}^{n+1} \\ &= -\frac{V_{j,m}}{\Delta t_n} \left(\hat{U}_{I_b,j,m}^n + \Delta t_n \frac{(b + \delta_{j_o} b_0)}{\alpha_{I_b,m}} (A\Phi)_{I_b,j,m}^{u;n+1} \right), \end{aligned} \quad (3.51c)$$

$$\begin{aligned} & \hat{A}_{j,m}^w \hat{W}_{I_b,j-1,m}^{n+1} + \hat{A}_{j+1,m}^w \hat{W}_{I_b,m,j+1}^{n+1} - \hat{D}_{j,m}^w \hat{W}_{I_b,m,j,m}^{n+1} + \hat{B}_{j,m}^w \hat{W}_{I_b,m-1,j,m}^{n+1} \\ &+ \hat{B}_{j,m+1}^w \hat{W}_{I_b,j,m+1}^{n+1} = -\frac{V_{j,m}}{\Delta t_n} \left[\hat{U}_{I_b,j,m}^n + \Delta t_n \left(\frac{(b + \delta_{j_o} b_0)}{\alpha_{I_b,m}} (A\Phi)_{I_b,j,m}^{w;n+1} \right. \right. \\ &\left. \left. + S_{\text{ratio}} g_2(\hat{U}_{I_b,j,m}^{n+1}) - \frac{1}{R_0} g_1(\hat{W}_{I_b,j,m}^{n+1}) \right) \right], \end{aligned} \quad (3.51d)$$

with

$$D_{i,m}^u = C_{i,m}^u + \frac{V_{i,m}}{\Delta t_n} [1 + \Delta t_n (S_2 + \delta_{j_o} S_0 P(r_i, t_{n+1}))], \quad (3.52a)$$

$$D_{i,m}^w = C_{i,m}^w + \frac{V_{i,m}}{\Delta t_n}, \quad \hat{D}_{j,m}^u = \hat{C}_{j,m}^u + \frac{V_{j,m}}{\Delta t_n}, \quad \hat{D}_{j,m}^w = \hat{C}_{j,m}^w + \frac{V_{j,m}}{\Delta t_n}, \quad (3.52b)$$

where $A^u, A^w, B^u, B^w, C^u, C^w, \hat{A}^u, \hat{A}^w, \hat{B}^u, \hat{B}^w, \hat{C}^u, \hat{C}^w$ are defined as

$$A_{i,m}^u = \alpha_{i-1/2,m} Du_r / (r_i - r_{i-1}),$$

$$i = 1, 2, \dots, I_p + 1, \quad m = 1, 2, \dots, M_p; \quad (3.53a)$$

$$A_{i,m}^w = \alpha_{i-1/2,m} Dw_r / (r_i - r_{i-1}),$$

$$i = 1, 2, \dots, I_p + 1, \quad m = 1, 2, \dots, M_p; \quad (3.53b)$$

$$B_{i,m}^u = \alpha_{i,m-1/2} Du_\theta / (r_i \Delta\theta),$$

$$i = 1, 2, \dots, I_p, \quad m = 1, 2, \dots, M_p + 1; \quad (3.53c)$$

$$B_{i,m}^w = \alpha_{i,m-1/2} Dw_\theta / (r_i \Delta\theta),$$

$$i = 1, 2, \dots, I_p, \quad m = 1, 2, \dots, M_p + 1; \quad (3.53d)$$

$$C_{i,m}^u = A_{i,m}^u + A_{i+1,m}^u + B_{i,m}^u + B_{i,m+1}^u,$$

$$i = 1, 2, \dots, I_p, \quad m = 1, 2, \dots, M_p; \quad (3.53e)$$

$$C_{i,m}^w = A_{i,m}^w + A_{i+1,m}^w + B_{i,m}^w + B_{i,m+1}^w,$$

$$i = 1, 2, \dots, I_p, \quad m = 1, 2, \dots, M_p. \quad (3.53f)$$

The boundary conditions are given by

$$U_{i,j,0}^n = U_{i,j,M_p}^n, \quad W_{i,j,0}^n = W_{i,j,M_p}^n, \quad (3.54a)$$

$$U_{i,j,M_p+1}^n = U_{i,j,1}^n, \quad W_{i,j,M_p+1}^n = W_{i,j,1}^n, \quad (3.54b)$$

$$\widehat{U}_{I_p+1,0,m}^n = \widehat{U}_{I_p+1,1,m}^n, \quad \widehat{W}_{I_p+1,0,m}^n = \widehat{W}_{I_p+1,1,m}^n, \quad (3.54c)$$

$$\widehat{U}_{I_p+1,J_p+1,m}^n = \widehat{U}_{I_p+1,J_p,m}^n, \quad \widehat{W}_{I_p+1,J_p+1,m}^n = \widehat{W}_{I_p+1,J_p,m}^n, \quad (3.54d)$$

$$U_{0,j,m}^n = U_{0,j}^n = U_{1,j,m}^n, \quad W_{0,j,m}^n = W_{0,j}^n = W_{1,j,m}^n, \quad (3.54e)$$

$$U_{I_p+1,j,m}^n = \widehat{U}_{I_p+1,j,m}^n, \quad W_{I_p+1,j,m}^n = \widehat{W}_{I_p+1,j,m}^n. \quad (3.54f)$$

Using the definition of the functions g_1 from (2.36) in equation (3.51c) and using the safe quadratic formula from [43], we compute

$$\widehat{W}_{I_b,j,m}^{n+1} = \frac{C}{Q}, \quad Q = \frac{1}{2} \left(B + \text{sign}(B) \sqrt{B^2 + 4AC} \right), \quad (3.55)$$

where

$$C = \widehat{W}_{I_b, j-1, m}^n + \frac{\Delta t_n}{V_{j, m}} \left[\widehat{A}_{j, m}^w \widehat{W}_{I_b, j-1, m}^{n+1} + \widehat{A}_{j+1, m}^w \widehat{W}_{I_b, m, j+1}^{n+1} + \widehat{B}_{j, m}^w \widehat{W}_{I_b, m-1, j, m}^{n+1} \right. \\ \left. + \widehat{B}_{j, m+1}^w \widehat{W}_{I_b, j, m+1}^{n+1} + \frac{(b + \delta_{j_0} b_0)}{\alpha_{I_b, m}} (A\Phi)_{I_b, j, m}^{w; n+1} + S_{\text{ratio}} g_2(\widehat{U}_{I_b, j, m}^{n+1}) \right], \quad (3.56)$$

$$A = 1 + \Delta t_n \widehat{C}_{j, m}^w, \quad (3.57)$$

$$B = A + \frac{\Delta t_n}{R_0} - C. \quad (3.58)$$

3.2.2 Discretization Based on the Weak Form

Consider the following weak form of the homogenized limit problem from §2.7.4.

$$(1 - \nu) \int_0^\tau \int_0^\eta \int_0^\rho \int_0^{2\pi} \psi \left\{ \frac{\partial u}{\partial t} + \nabla_{r, \theta} \cdot \Phi_u - S_{\min} - S_1 f_1(w) + S_2 u \right\}_{z \neq z_0} r d\theta dr dz dt \\ + \rho_o \int_0^\tau \int_0^\eta \int_0^\rho \int_0^{2\pi} \psi \left\{ \frac{\partial \widehat{u}}{\partial t} + \nabla_{z, \theta} \cdot \Psi_{\widehat{u}} - \frac{(1 - \nu)}{\rho_o} \Phi_{ur} \right\}_{r=\rho} \rho d\theta dz dt \\ + \zeta \int_0^\tau \int_0^\rho \int_0^{2\pi} \psi \left\{ \frac{\partial \bar{u}}{\partial t} + \nabla_{r, \theta} \cdot \Phi_{\bar{u}} - S_{\min} - S_1 f_1(\bar{w}) + S_2 \bar{u} + S_0 \bar{u} P \right\}_{z=z_0, r \neq \rho} r d\theta dr dt \\ - \zeta \int_0^\tau \int_0^{2\pi} \left\{ \psi \Phi_{\bar{u}r} \right\}_{z=z_0, r=\rho} \rho d\theta dt = 0, \quad (3.59a)$$

$$(1 - \nu) \int_0^\tau \int_0^\eta \int_0^\rho \int_0^{2\pi} \psi \left\{ \frac{\partial w}{\partial t} + \nabla_{r, \theta} \cdot \Phi_w \right\}_{z \neq z_0} r d\theta dr dz dt \\ + \rho_o \int_0^\tau \int_0^\eta \int_0^\rho \int_0^{2\pi} \psi \left\{ \frac{\partial \widehat{w}}{\partial t} + \nabla_{z, \theta} \cdot \Psi_{\widehat{w}} - \frac{(1 - \nu)}{\rho_o} \Phi_{wr} + S_{\text{ex}} g_1(\widehat{w}) - S_{\text{cG}} g_2(\widehat{u}) \right\}_{r=\rho} \rho d\theta dz dt \\ + \zeta \int_0^\tau \int_0^\rho \int_0^{2\pi} \psi \left\{ \frac{\partial \bar{w}}{\partial t} + \nabla_{r, \theta} \cdot \Phi_{\bar{w}} \right\}_{z=z_0, r \neq \rho} r d\theta dr dt \\ - \zeta \int_0^\tau \int_0^{2\pi} \left\{ \psi \Phi_{\bar{w}r} \right\}_{z=z_0, r=\rho} \rho d\theta dt = 0. \quad (3.59b)$$

Now choose the test function ψ as the characteristic function of the closure of the control volume $\bar{V}_{i, j, m}$, i.e., $\psi(x) = 1$ if $x \in \bar{V}_{i, j, m}$, and 0 otherwise. Let

$\{t_0 \cdots, t_{N_{\max}}\}$, be a partition of $[0, \tau]$, and $\Delta t_n = t_{n+1} - t_n$ the time step size. Then for $n = 0, 1, 2, \dots, N_{\max}$, and for each control volume $V_{i,j,m}$, $i = 1, 2, \dots, I_p$, $j = 1, 2, \dots, j_0, \dots, J_p$, $m = 1, 2, \dots, M_p$ with j_0 the special z -level(s) where light is applied, we get

$$\begin{aligned}
& (1 - \nu) \int_{t_n}^{t_{n+1}} \int_{V_{i,j,m}} \left\{ \frac{\partial u}{\partial t} + \nabla_{r,\theta} \cdot \mathbf{\Phi}_u - S_{\min} - S_1 f_1(w) + S_2 u \right\} r d\theta dr dz dt \\
& + \rho_o \int_{t_n}^{t_{n+1}} \int_{A_{I_p+\frac{1}{2},j,m}} \left\{ \frac{\partial \hat{u}}{\partial t} + \nabla_{z,\theta} \cdot \mathbf{\Psi}_{\hat{u}} - \frac{(1 - \nu)}{\rho_o} \mathbf{\Phi}_{ur} \right\} r d\theta dz dt \\
& + \zeta \int_{t_n}^{t_{n+1}} \int_{A_{i,j_0-\frac{1}{2},m}} \left\{ \frac{\partial \bar{u}}{\partial t} + \nabla_{r,\theta} \cdot \mathbf{\Phi}_{\bar{u}} - S_{\min} - S_1 f_1(\bar{w}) + S_2 \bar{u} + S_0 \bar{u} P \right\} r d\theta dr dt \\
& - \zeta \int_{t_n}^{t_{n+1}} \int_{\beta_{I_b,j_0-\frac{1}{2},m}} \mathbf{\Phi}_{\bar{u}r} R d\theta dt = 0, \tag{3.60a}
\end{aligned}$$

$$\begin{aligned}
& (1 - \nu) \int_{t_n}^{t_{n+1}} \int_{V_{i,j,m}} \left\{ \frac{\partial w}{\partial t} + \nabla_{r,\theta} \cdot \mathbf{\Phi}_w \right\} r d\theta dr dz dt \\
& + \rho_o \int_{t_n}^{t_{n+1}} \int_{A_{I_p+\frac{1}{2},j,m}} \left\{ \frac{\partial \hat{w}}{\partial t} + \nabla_{z,\theta} \cdot \mathbf{\Psi}_{\hat{w}} - \frac{(1 - \nu)}{\rho_o} \mathbf{\Phi}_{wr} + S_{\text{ex}} g_1(\hat{w}) - S_{\text{CG}} g_2(\hat{u}) \right\} r d\theta dz dt \\
& + \zeta \int_{t_n}^{t_{n+1}} \int_{A_{i,j_0-\frac{1}{2},m}} \left\{ \frac{\partial \bar{w}}{\partial t} + \nabla_{r,\theta} \cdot \mathbf{\Phi}_{\bar{w}} \right\} r d\theta dr dt \\
& - \zeta \int_{t_n}^{t_{n+1}} \int_{\beta_{I_b,j_0-\frac{1}{2},m}} \mathbf{\Phi}_{\bar{w}r} R d\theta dt = 0. \tag{3.60b}
\end{aligned}$$

Using the Divergence Theorem, we obtain

$$\begin{aligned}
& (1 - \nu) \left\{ \int_{V_{i,j,m}} \{u(t_{n+1}) - u(t_n)\} dV + \int_{t_n}^{t_{n+1}} \int_{\partial V_{i,j,m}} \mathbf{\Phi}_u \cdot \mathbf{n}_{i,m} dA dt \right. \\
& \quad \left. - \int_{t_n}^{t_{n+1}} \int_{V_{i,j,m}} \{S_{\min} + S_1 f_1(w) - S_2 u\} dV dt \right\} \\
& + \rho_o \left\{ \int_{A_{I_p+\frac{1}{2},j,m}} \{\hat{u}(t_{n+1}) - \hat{u}(t_n)\} dA + \int_{t_n}^{t_{n+1}} \int_{\partial A_{I_p+\frac{1}{2},j,m}} \mathbf{\Psi}_{\hat{u}} \cdot \mathbf{n}_{j,m} dL dt \right.
\end{aligned}$$

$$\begin{aligned}
& - \int_{t_n}^{t_{n+1}} \int_{A_{I_p+\frac{1}{2},j,m}} \left\{ \frac{(1-\nu)}{\rho_o} \Phi_{ur} \right\} dA dt \Bigg\} \\
+ \zeta & \left\{ \int_{A_{i,j_0-\frac{1}{2},m}} \{ \bar{u}(t_{n+1}) - \bar{u}(t_n) \} dA + \int_{t_n}^{t_{n+1}} \int_{\partial A_{i,j_0-\frac{1}{2},m}} \Phi_{\bar{u}} \cdot \mathbf{n}_{i,m} dL dt \right. \\
& - \int_{t_n}^{t_{n+1}} \int_{A_{i,j_0-\frac{1}{2},m}} \{ S_{\min} + S_1 f_1(\bar{w}) - S_2 \bar{u} - S_0 \bar{u} P \} dA dt \\
& \left. - \int_{t_n}^{t_{n+1}} \int_{\beta_{I_b,j_0-\frac{1}{2},m}} \Phi_{\bar{u}r} R d\theta dt \right\} = 0, \tag{3.61a}
\end{aligned}$$

$$\begin{aligned}
(1-\nu) & \left\{ \int_{V_{i,j,m}} \{ w(t_{n+1}) - w(t_n) \} dA + \int_{t_n}^{t_{n+1}} \int_{\partial V_{i,j,m}} \Phi_w \cdot \mathbf{n}_{i,m} dA dt \right\} \\
+ \rho_o & \left\{ \int_{A_{I_p+\frac{1}{2},j,m}} \{ \hat{w}(t_{n+1}) - \hat{w}(t_n) \} dA + \int_{t_n}^{t_{n+1}} \int_{\partial A_{I_p+\frac{1}{2},j,m}} \Psi_{\hat{w}} \cdot \mathbf{n}_{j,m} dL dt \right. \\
& \left. - \int_{t_n}^{t_{n+1}} \int_{A_{I_p+\frac{1}{2},j,m}} \left\{ \frac{(1-\nu)}{\rho_o} \Phi_{wr} - S_{\text{ex}} g_1(\hat{w}) + S_{\text{cG}} g_2(\hat{u}) \right\} dA dt \right\} \\
+ \zeta & \left\{ \int_{A_{i,j_0-\frac{1}{2},m}} \{ \bar{w}(t_{n+1}) - \bar{w}(t_n) \} dV + \int_{t_n}^{t_{n+1}} \int_{\partial A_{i,j_0-\frac{1}{2},m}} \Phi_{\bar{w}} \cdot \mathbf{n}_{i,m} dL dt \right. \\
& \left. - \int_{t_n}^{t_{n+1}} \int_{\beta_{I_b,j_0-\frac{1}{2},m}} \Phi_{\bar{w}r} R d\theta dt \right\} = 0. \tag{3.61b}
\end{aligned}$$

Define $t_{n+\vartheta} := t_n + \vartheta \Delta t_n = (1-\vartheta)t_n + \vartheta t_{n+1}$, with $0 \leq \vartheta \leq 1$. Then

$$\begin{aligned}
(1-\nu) & \left\{ \int_{V_{i,j,m}} \{ u(t_{n+1}) - u(t_n) \} dV + \Delta t_n \int_{\partial V_{i,j,m}} \Phi_u(t_{n+\vartheta}) \cdot \mathbf{n}_{i,m} dA \right. \\
& \left. - \Delta t_n \int_{V_{i,j,m}} \{ S_{\min} + S_1 f_1(w(t_{n+\vartheta})) - S_2 u(t_{n+\vartheta}) \} dV \right\} \\
+ \rho_o & \left\{ \int_{A_{I_p+\frac{1}{2},j,m}} \{ \hat{u}(t_{n+1}) - \hat{u}(t_n) \} dA + \Delta t_n \int_{\partial A_{I_p+\frac{1}{2},j,m}} \Psi_{\hat{u}}(t_{n+\vartheta}) \cdot \mathbf{n}_{j,m} dL \right.
\end{aligned}$$

$$\begin{aligned}
& -\Delta t_n \int_{A_{I_p+\frac{1}{2},j,m}} \left\{ \frac{(1-\nu)}{\rho_o} \Phi_{ur}(t_{n+\vartheta}) \right\} dA \Bigg\} \\
& + \zeta \left\{ \int_{A_{i,j_0-\frac{1}{2},m}} \{\bar{u}(t_{n+1}) - \bar{u}(t_n)\} dA + \Delta t_n \int_{\partial A_{i,j_0-\frac{1}{2},m}} \Phi_{\bar{u}}(t_{n+\vartheta}) \cdot \mathbf{n}_{i,m} dL \right. \\
& - \Delta t_n \int_{A_{i,j_0-\frac{1}{2},m}} \{S_{\min} + S_1 f_1(\bar{w}(t_{n+\vartheta})) - S_2 \bar{u}(t_{n+\vartheta}) - S_0 \bar{u}(t_{n+\vartheta}) P(t_{n+\vartheta})\} dA \\
& \left. - \Delta t_n \int_{\beta_{I_b,j_0-\frac{1}{2},m}} \Phi_{\bar{u}r}(t_{n+\vartheta}) R d\theta \right\} = 0, \tag{3.62a}
\end{aligned}$$

$$\begin{aligned}
& (1-\nu) \left\{ \int_{V_{i,j,m}} \{w(t_{n+1}) - w(t_n)\} dA + \Delta t_n \int_{\partial V_{i,j,m}} \Phi_w(t_{n+\vartheta}) \cdot \mathbf{n}_{i,m} dA \right\} \\
& + \rho_o \left\{ \int_{A_{I_p+\frac{1}{2},j,m}} \{\hat{w}(t_{n+1}) - \hat{w}(t_n)\} dA + \Delta t_n \int_{\partial A_{I_p+\frac{1}{2},j,m}} \Psi_{\hat{w}}(t_{n+\vartheta}) \cdot \mathbf{n}_{j,m} dL \right. \\
& - \Delta t_n \int_{A_{I_p+\frac{1}{2},j,m}} \left\{ \frac{(1-\nu)}{\rho_o} \Phi_{wr}(t_{n+\vartheta}) - S_{\text{ex}} g_1(\hat{w}(t_{n+\vartheta})) + S_{\text{cG}} g_2(\hat{u}(t_{n+\vartheta})) \right\} dA \Bigg\} \\
& + \zeta \left\{ \int_{A_{i,j_0-\frac{1}{2},m}} \{\bar{w}(t_{n+1}) - \bar{w}(t_n)\} dV + \Delta t_n \int_{\partial A_{i,j_0-\frac{1}{2},m}} \Phi_{\bar{w}}(t_{n+\vartheta}) \cdot \mathbf{n}_{i,m} dL \right. \\
& \left. - \Delta t_n \int_{\beta_{I_b,j_0-\frac{1}{2},m}} \Phi_{\bar{w}r}(t_{n+\vartheta}) R d\theta \right\} = 0. \tag{3.62b}
\end{aligned}$$

Define $U_{i,j,m}^n$, $W_{i,j,m}^n$ as the mean values over the control volume $V_{i,j,m}$. Realize that $u(r, z_0, \theta) = \bar{u}(r, \theta)$, $u(\rho, z, \theta) = \hat{u}(z, \theta)$, and similarly for w , \bar{w} and \hat{w} . Computing the integrals of the fluxes as the sum of the flow rates along the faces, we obtain for $n = 0, 1, 2, \dots, N_{\max}$, $i = 1, 2, \dots, I_p$, $j = 1, 2, \dots, j_0, \dots, J_p$, and $m = 1, 2, \dots, M_p$ with j_0 the special z -level(s),

$$\begin{aligned}
& (1-\nu) \left\{ (U_{i,j,m}^{n+1} - U_{i,j,m}^n) V_{i,j,m} - \Delta t_n \left[(A\Phi)_{i-\frac{1}{2},j,m}^{u;n+\vartheta} + (A\Phi)_{i+\frac{1}{2},j,m}^{u;n+\vartheta} \right. \right. \\
& \left. \left. + (A\Phi)_{i,j,m-\frac{1}{2}}^{u;n+\vartheta} + (A\Phi)_{i,j,m+\frac{1}{2}}^{u;n+\vartheta} \right] - \Delta t_n [S_{\min} + S_1 f_1(W_{i,j,m}^{n+\vartheta}) - S_2 U_{i,j,m}^{n+\vartheta}] V_{i,j,m} \right\}
\end{aligned}$$

$$\begin{aligned}
& + \rho_o \left\{ \left(U_{I_p,j,m}^{n+1} - U_{I_p,j,m}^n \right) A_{I_b,j,m} - \Delta t_n \left[(\beta\Psi)_{I_b,j-\frac{1}{2},m}^{u;n+\vartheta} + (\beta\Psi)_{I_b,j+\frac{1}{2},m}^{u;n+\vartheta} \right. \right. \\
& \left. \left. + (\beta\Psi)_{I_b,j,m-\frac{1}{2}}^{u;n+\vartheta} + (\beta\Psi)_{I_b,j,m+\frac{1}{2}}^{u;n+\vartheta} \right] - \Delta t_n \left[\frac{(1-\nu)}{\rho_o} A_{I_b,j,m} \Phi_{I_b,j,m}^{u;n+\vartheta} \right] \right\} \delta_{i,I_p} \\
& + \zeta \left\{ \left(U_{i,j_0,m}^{n+1} - U_{i,j_0,m}^n \right) A_{i,j_0-\frac{1}{2},m} - \Delta t_n \left[(\alpha\Phi)_{i-\frac{1}{2},j_0,m}^{u;n+\vartheta} + (\alpha\Phi)_{i+\frac{1}{2},j_0,m}^{u;n+\vartheta} \right. \right. \\
& \left. \left. + (\alpha\Phi)_{i,j_0,m-\frac{1}{2}}^{u;n+\vartheta} + (\alpha\Phi)_{i,j_0,m+\frac{1}{2}}^{u;n+\vartheta} \right] - \Delta t_n \left[S_{\min} + S_1 f_1(W_{i,j_0,m}^{n+\vartheta}) - S_2 U_{i,j_0,m}^{n+\vartheta} \right. \right. \\
& \left. \left. - S_0 P U_{i,j_0,m}^{n+\vartheta} \right] A_{i,j_0-\frac{1}{2},m} - \Delta t_n \left[\alpha_{I_b,m} \Phi_{I_b,j_0,m}^{u;n+\vartheta} \right] \right\} \delta_{j,j_0} = 0, \quad (3.63a)
\end{aligned}$$

$$\begin{aligned}
& (1-\nu) \left\{ \left(W_{i,j,m}^{n+1} - W_{i,j,m}^n \right) V_{i,j,m} \right. \\
& \left. - \Delta t_n \left[(A\Phi)_{i-\frac{1}{2},j,m}^{w;n+\vartheta} + (A\Phi)_{i+\frac{1}{2},j,m}^{w;n+\vartheta} + (A\Phi)_{i,j,m-\frac{1}{2}}^{w;n+\vartheta} + (A\Phi)_{i,j,m+\frac{1}{2}}^{w;n+\vartheta} \right] \right\} \\
& + \rho_o \left\{ \left(W_{I_p,j,m}^{n+1} - W_{I_p,j,m}^n \right) A_{I_b,j,m} - \Delta t_n \left[(\beta\Psi)_{I_b,j-\frac{1}{2},m}^{w;n+\vartheta} + (\beta\Psi)_{I_b,j+\frac{1}{2},m}^{w;n+\vartheta} \right. \right. \\
& \left. \left. + (\beta\Psi)_{I_b,j,m-\frac{1}{2}}^{w;n+\vartheta} + (\beta\Psi)_{I_b,j,m+\frac{1}{2}}^{w;n+\vartheta} \right] - \Delta t_n \left[S_{cG} g_2(U_{I_p,j,m}^{n+\vartheta}) - S_{ex} g_1(W_{I_p,j,m}^{n+\vartheta}) \right] A_{I_b,j,m} \right. \\
& \left. - \Delta t_n \left[\frac{(1-\nu)}{\rho_o} A_{I_b,j,m} \Phi_{I_b,j,m}^{w;n+\vartheta} \right] \right\} \delta_{i,I_p} \\
& + \zeta \left\{ \left(W_{i,j_0,m}^{n+1} - W_{i,j_0,m}^n \right) A_{i,j_0-\frac{1}{2},m} - \Delta t_n \left[(\alpha\Phi)_{i-\frac{1}{2},j_0,m}^{w;n+\vartheta} + (\alpha\Phi)_{i+\frac{1}{2},j_0,m}^{w;n+\vartheta} \right. \right. \\
& \left. \left. + (\alpha\Phi)_{i,j_0,m-\frac{1}{2}}^{w;n+\vartheta} + (\alpha\Phi)_{i,j_0,m+\frac{1}{2}}^{w;n+\vartheta} \right] - \Delta t_n \left[\alpha_{I_b,m} \Phi_{I_b,j_0,m}^{w;n+\vartheta} \right] \right\} \delta_{j,j_0} = 0, \quad (3.63b)
\end{aligned}$$

where the u -flow rates are given by

$$(A\Phi)_{i\pm\frac{1}{2},j,m}^{u;n+\vartheta} = \mp A_{i-\frac{1}{2},j,m} \Phi_{i-\frac{1}{2},j,m}^{u;n+\vartheta}, \quad (A\Phi)_{i,j,m\pm\frac{1}{2}}^{u;n+\vartheta} = \mp A_{i,j,m-\frac{1}{2}} \Phi_{i,j,m-\frac{1}{2}}^{u;n+\vartheta} \quad (3.64a)$$

$$(\alpha\Phi)_{i\pm\frac{1}{2},j,m}^{u;n+\vartheta} = \mp \alpha_{i-\frac{1}{2},m} \Phi_{i-\frac{1}{2},j,m}^{u;n+\vartheta}, \quad (\alpha\Phi)_{i,j,m\pm\frac{1}{2}}^{u;n+\vartheta} = \mp \alpha_{i,m-\frac{1}{2}} \Phi_{i,j,m-\frac{1}{2}}^{u;n+\vartheta} \quad (3.64b)$$

$$(\beta\Psi)_{I_b,j\pm\frac{1}{2},m}^{u;n+\vartheta} = \mp \beta_{j-\frac{1}{2},m} \Psi_{I_b,j-\frac{1}{2},m}^{u;n+\vartheta}, \quad (\beta\Psi)_{I_b,j\pm\frac{1}{2},m}^{u;n+\vartheta} = \mp \beta_{j-\frac{1}{2},m} \Psi_{I_b,j-\frac{1}{2},m}^{u;n+\vartheta} \quad (3.64c)$$

and similar expressions for the w -flow rates, with the areas

$$\alpha_{i-\frac{1}{2},m} = r_{i-\frac{1}{2}} \Delta\theta, \quad \alpha_{i,m-\frac{1}{2}} = \Delta r, \quad \beta_{j-\frac{1}{2},m} = r_{I_p+1} \Delta\theta, \quad \text{and} \quad \beta_{j,m-\frac{1}{2}} = \Delta z.$$

Note that $\alpha_{I_b,m} = \beta_{j_0-\frac{1}{2},m}$ in the last term of the equations (3.63a) and (3.63b). The u -fluxes are computed as

$$\begin{aligned}\Phi_{i-\frac{1}{2},j,m}^{u;n+\vartheta} &= -D_{ur} \left(\frac{U_{i,j,m}^{n+\vartheta} - U_{i-1,j,m}^{n+\vartheta}}{r_i - r_{i-1}} \right), & \Phi_{i,j,m-\frac{1}{2}}^{u;n+\vartheta} &= -\frac{D_{u\theta}}{r_i} \left(\frac{U_{i,j,m}^{n+\vartheta} - U_{i,j,m-1}^{n+\vartheta}}{\theta_m - \theta_{m-1}} \right), \\ \Psi_{I_b,j-\frac{1}{2},m}^{u;n+\vartheta} &= -D_{uz} \left(\frac{U_{I_p,j,m}^{n+\vartheta} - U_{I_p,j-1,m}^{n+\vartheta}}{z_j - z_{j-1}} \right), & \Psi_{I_b,j,m-\frac{1}{2}}^{u;n+\vartheta} &= -\frac{D_{u\theta}}{r_{I_b}} \left(\frac{U_{I_p,j,m}^{n+\vartheta} - U_{I_p,j,m-1}^{n+\vartheta}}{\theta_m - \theta_{m-1}} \right),\end{aligned}$$

and similarly for the w -fluxes. Using the relations

$$\begin{aligned}A_{I_b,j,m} &= \left(\frac{r_{I_b}}{r_{I_p} \Delta r} \right) V_{I_p,j,m}, & \beta_{I_b,j-\frac{1}{2},m} &= \left(\frac{r_{I_b}}{r_{I_p} \Delta r} \right) A_{I_p,j-\frac{1}{2},m}, \\ A_{i,j_0-\frac{1}{2},m} &= \frac{1}{\Delta z} V_{i,j_0,m}, & \beta_{I_b,j,m-\frac{1}{2}} &= \frac{1}{\Delta r} A_{I_p,j,m-\frac{1}{2}}, \\ \alpha_{i-\frac{1}{2},j_0,m} &= \frac{1}{\Delta z} A_{i-\frac{1}{2},j_0,m}, & \alpha_{i,j_0,m-\frac{1}{2}} &= \frac{1}{\Delta z} A_{i,j_0,m-\frac{1}{2}}, \text{ etc.}\end{aligned}$$

we obtain the following **numerical scheme**.

1. *Internal Nodes*: for $i = 1, 2, \dots, I_p - 1$, and $m = 1, 2, \dots, M_p$.

$$\begin{aligned}& (U_{i,j,m}^{n+1} - U_{i,j,m}^n) V_{i,j,m} \\ & - \Delta t_n \left[(A\Phi)_{i-\frac{1}{2},j,m}^{u;n+\vartheta} + (A\Phi)_{i+\frac{1}{2},j,m}^{u;n+\vartheta} + (A\Phi)_{i,j,m-\frac{1}{2}}^{u;n+\vartheta} + (A\Phi)_{i,j,m+\frac{1}{2}}^{u;n+\vartheta} \right] \\ & - \Delta t_n \{ S_{\min} + S_1 f_1(W_{i,j,m}^{n+\vartheta}) - S_2 U_{i,j,m}^{n+\vartheta} - \delta_{j,j_0} S_0 P U_{i,j,m}^{n+\vartheta} \} V_{i,j,m} = 0, \quad (3.65a)\end{aligned}$$

$$\begin{aligned}& (W_{i,j,m}^{n+1} - W_{i,j,m}^n) V_{i,j,m} \\ & - \Delta t_n \left[(A\Phi)_{i-\frac{1}{2},j,m}^{w;n+\vartheta} + (A\Phi)_{i+\frac{1}{2},j,m}^{w;n+\vartheta} + (A\Phi)_{i,j,m-\frac{1}{2}}^{w;n+\vartheta} + (A\Phi)_{i,j,m+\frac{1}{2}}^{w;n+\vartheta} \right] = 0, \quad (3.65b)\end{aligned}$$

2. *Lateral Boundary Nodes* ($i = I_p$): for $j = 1, 2, \dots, j_0, \dots, J_p$, and $m = 1, 2, \dots, M_p$.

$$\begin{aligned}& \left\{ \delta_{j,j_0} \frac{\zeta}{\Delta z} + (1 - \nu) + \rho_o \left(\frac{r_{I_b}}{r_{I_p} \Delta r} \right) \right\} (U_{I_p,j,m}^{n+1} - U_{I_p,j,m}^n) V_{I_p,j,m} \\ & - \Delta t_n \left\{ \left(\delta_{j,j_0} \frac{\zeta}{\Delta z} + (1 - \delta_{j,j_0})(1 - \nu) \right) \left[(A\Phi)_{I_p-\frac{1}{2},j,m}^{u;n+\vartheta} \right. \right.\end{aligned}$$

$$\begin{aligned}
& + (A\Phi)_{I_p,j,m-\frac{1}{2}}^{u;n+\vartheta} + (A\Phi)_{I_p,j,m+\frac{1}{2}}^{u;n+\vartheta} \Big] \\
+ \frac{\rho_o}{\Delta r} & \left[\left((A\Psi)_{I_b,j-\frac{1}{2},m}^{u;n} + (A\Psi)_{I_b,j+\frac{1}{2},m}^{u;n} \right) \left(\frac{r_{I_b}}{r_{I_p}} \right) + (A\Psi)_{I_b,j,m-\frac{1}{2}}^{u;n+\vartheta} + (A\Psi)_{I_b,j,m+\frac{1}{2}}^{u;n+\vartheta} \right] \Big\} \\
- \Delta t_n & \left(\delta_{j,j_0} \frac{\zeta}{\Delta z} + (1-\nu) \right) \left[S_{\min} + S_1 f_1(W_{I_p,j,m}^{n+\vartheta}) - S_2 U_{I_p,j,m}^{n+\vartheta} \right] V_{I_p,j,m} = 0,
\end{aligned} \tag{3.66a}$$

$$\begin{aligned}
& \left\{ \delta_{j,j_0} \frac{\zeta}{\Delta z} + (1-\nu) + \rho_o \left(\frac{r_{I_b}}{r_{I_p} \Delta r} \right) \right\} \left(W_{I_p,j,m}^{n+1} - W_{I_p,j,m}^n \right) V_{I_p,j,m} \\
- \Delta t_n & \left\{ \left(\delta_{j,j_0} \frac{\zeta}{\Delta z} + (1-\nu) \right) \left[(A\Phi)_{I_p-\frac{1}{2},j,m}^{w;n+\vartheta} + (A\Phi)_{I_p,j,m-\frac{1}{2}}^{w;n+\vartheta} + (A\Phi)_{I_p,j,m+\frac{1}{2}}^{w;n+\vartheta} \right] \right. \\
+ \frac{\rho_o}{\Delta r} & \left[\left((A\Psi)_{I_b,j-\frac{1}{2},m}^{w;n} + (A\Psi)_{I_b,j+\frac{1}{2},m}^{w;n} \right) \left(\frac{r_{I_b}}{r_{I_p}} \right) + (A\Psi)_{I_b,j,m-\frac{1}{2}}^{w;n+\vartheta} + (A\Psi)_{I_b,j,m+\frac{1}{2}}^{w;n+\vartheta} \right] \Big\} \\
- \Delta t_n & \left\{ \rho_o \left(\frac{r_{I_b}}{r_{I_p} \Delta r} \right) \left[S_{\text{cG}} g_2(U_{I_b,j,m}^{n+\vartheta}) - S_{\text{ex}} g_1(W_{I_b,j,m}^{n+\vartheta}) \right] \right\} V_{I_p,j,m} = 0,
\end{aligned} \tag{3.66b}$$

Explicit-Implicit Scheme

Taking $\vartheta = 1$ in the source terms and $\vartheta = 0$ in the flux terms, and solving the resulting equations for $U_{i,j,m}^{n+1}$ and $W_{i,j,m}^{n+1}$, we get the following Explicit-Implicit numerical scheme

1. *Internal Nodes:* for $i = 1, 2, \dots, I_p - 1$, $j = 1, 2, \dots, J_p$, and $m = 1, 2, \dots, M_p$.

$$\begin{aligned}
W_{i,j,m}^{n+1} = W_{i,j,m}^n + \frac{\Delta t_n}{V_{i,j,m}} & \left[(A\Phi)_{i-\frac{1}{2},j,m}^{w;n} + (A\Phi)_{i+\frac{1}{2},j,m}^{w;n} \right. \\
& \left. + (A\Phi)_{i,j,m-\frac{1}{2}}^{w;n} + (A\Phi)_{i,j,m+\frac{1}{2}}^{w;n} \right], \tag{3.67a}
\end{aligned}$$

$$\begin{aligned}
U_{i,j,m}^{n+1} = & \left[U_{i,j,m}^n + \frac{\Delta t_n}{V_{i,j,m}} \left[(A\Phi)_{i-\frac{1}{2},j,m}^{u;n} + (A\Phi)_{i+\frac{1}{2},j,m}^{u;n} \right. \right. \\
& \left. \left. + (A\Phi)_{i,j,m-\frac{1}{2}}^{u;n} + (A\Phi)_{i,j,m+\frac{1}{2}}^{u;n} \right] + \Delta t_n \left[S_{\min} + S_1 f_1(W_{i,j,m}^{n+1}) \right] \right] \\
& / [1 + \Delta t_n (S_2 + \delta_{j,j_0} S_0 P)], \tag{3.67b}
\end{aligned}$$

2. *Lateral Boundary Nodes:* for $j = 1, 2, \dots, J_p$, and $m = 1, 2, \dots, M_p$.

$$W_{I_p, j, m}^{n+1} = C - D g_1(W_{I_b, j, m}^{n+1}) + E g_2(A + B f_1(W_{I_b, j, m}^{n+1})), \quad (3.68a)$$

$$U_{I_p, j, m}^{n+1} = A + B f_1(W_{I_b, j, m}^{n+1}), \quad (3.68b)$$

The constants A, B, C, D and E are as given below.

$$\begin{aligned} A = & \left[\left((1 - \nu) + \left(\frac{r_{I_b}}{r_{I_p} \Delta r} \right) \rho_0 + \delta_{j, j_0} \frac{\zeta}{\Delta z} \right) U_{I_p, j, m}^n \right. \\ & + \frac{\Delta t_n}{V_{i, j, m}} \left\{ \left((1 - \nu) + \delta_{j, j_0} \frac{\zeta}{\Delta z} \right) \left[(A\Phi)_{I_p - \frac{1}{2}, j, m}^{u; n} + (A\Phi)_{I_p, j, m - \frac{1}{2}}^{u; n} + (A\Phi)_{I_p, j, m + \frac{1}{2}}^{u; n} \right] \right. \\ & \left. + \frac{\rho_0}{\Delta r} \left[\left((A\Psi)_{I_b, j - \frac{1}{2}, m}^{u; n} + (A\Psi)_{I_b, j + \frac{1}{2}, m}^{u; n} \right) \left(\frac{r_{I_b}}{r_{I_p}} \right) + (A\Psi)_{I_b, j, m - \frac{1}{2}}^{u; n} + (A\Psi)_{I_b, j, m + \frac{1}{2}}^{u; n} \right] \right\} \\ & \left. + \Delta t_n \left((1 - \nu) + \delta_{j, j_0} \frac{\zeta}{\Delta z} \right) S_{\min} \right] / \left[\left((1 - \nu) + \left(\frac{r_{I_b}}{r_{I_p} \Delta r} \right) \rho_0 + \delta_{j, j_0} \frac{\zeta}{\Delta z} \right) \right. \\ & \left. + \Delta t_n \left\{ \left((1 - \nu) + \delta_{j, j_0} \frac{\zeta}{\Delta z} \right) S_2 + \delta_{j, j_0} \frac{\zeta}{\Delta z} S_0 P \right\} \right], \quad (3.69a) \end{aligned}$$

$$\begin{aligned} B = & \left[\Delta t_n \left((1 - \nu) + \delta_{j, j_0} \frac{\zeta}{\Delta z} \right) S_1 \right] / \left[\left((1 - \nu) + \left(\frac{r_{I_b}}{r_{I_p} \Delta r} \right) \rho_0 \right. \right. \\ & \left. \left. + \delta_{j, j_0} \frac{\zeta}{\Delta z} + \Delta t_n \left\{ \left((1 - \nu) + \delta_{j, j_0} \frac{\zeta}{\Delta z} \right) S_2 + \delta_{j, j_0} \frac{\zeta}{\Delta z} S_0 P \right\} \right] \right], \quad (3.69b) \end{aligned}$$

$$\begin{aligned} C = & W_{I_p, j, m}^n + \frac{\Delta t_n}{V_{i, j, m}} \left\{ \left((1 - \nu) + \delta_{j, j_0} \frac{\zeta}{\Delta z} \right) \left[(A\Phi)_{I_p - \frac{1}{2}, j, m}^{w; n} + (A\Phi)_{I_p, j, m - \frac{1}{2}}^{w; n} \right. \right. \\ & \left. \left. + (A\Phi)_{I_p, j, m + \frac{1}{2}}^{w; n} \right] + \frac{\rho_0}{\Delta r} \left[\left((A\Psi)_{I_b, j - \frac{1}{2}, m}^{w; n} + (A\Psi)_{I_b, j + \frac{1}{2}, m}^{w; n} \right) \left(\frac{r_{I_b}}{r_{I_p}} \right) \right. \right. \\ & \left. \left. + (A\Psi)_{I_b, j, m - \frac{1}{2}}^{w; n} + (A\Psi)_{I_b, j, m + \frac{1}{2}}^{w; n} \right] \right\} / \left[\left((1 - \nu) + \left(\frac{r_{I_b}}{r_{I_p} \Delta r} \right) \rho_0 + \delta_{j, j_0} \frac{\zeta}{\Delta z} \right) \right], \quad (3.69c) \end{aligned}$$

$$D = \left(\frac{\Delta t_n S_{\text{ex}}}{\left((1 - \nu) + \frac{\rho_0}{\Delta r} + \delta_{j, j_0} \frac{\zeta}{\Delta z} \right)} \right) \left(\frac{r_{I_b}}{r_{I_p} \Delta r} \right) \rho_0, \quad (3.69d)$$

$$E = \left(\frac{\Delta t_n S_{\text{cG}}}{\left((1 - \nu) + \frac{\rho_0}{\Delta r} + \delta_{j, j_0} \frac{\zeta}{\Delta z} \right)} \right) \left(\frac{r_{I_b}}{r_{I_p} \Delta r} \right) \rho_0. \quad (3.69e)$$

Fully Implicit Scheme

Taking $\vartheta = 1$ in the source terms and solving the resulting equations for $U_{i,j,m}^{n+1}$ and $W_{i,j,m}^{n+1}$, we get the following Fully Implicit numerical scheme

1. *Internal Nodes:* for $i = 1, 2, \dots, I_p - 1$, $j = 1, 2, \dots, J_p$, and $m = 1, 2, \dots, M_p$.

$$U_{i,j,m}^{n+1} = \left\{ U_{i,j,m}^n + \frac{\Delta t_n}{V_{i,m,j}} [A_{i,j,m}^u U_{i-1,j,m}^{n+1} + A_{i+1,j,m}^u U_{i+1,j,m}^{n+1} + B_{i,j,m}^u U_{i,j,m-1}^{n+1} + B_{i,j,m+1}^u U_{i,j,m+1}^{n+1} + \Delta t_n S_{\min} f_1(W_{i,j,m}^{n+1})] \right\} / \left(1 + \frac{\Delta t_n}{V_{i,m,j}} C_{i,j,m}^u + (S_2 + \delta_{j,j_0} S_0 P) \right), \quad (3.70a)$$

$$W_{i,j,m}^{n+1} = \left\{ W_{i,j,m}^n + \frac{\Delta t_n}{V_{i,m,j}} [A_{i,j,m}^w W_{i-1,j,m}^{n+1} + A_{i+1,j,m}^w W_{i+1,j,m}^{n+1} + B_{i,j,m}^w W_{i,j,m-1}^{n+1} + B_{i,j,m+1}^w W_{i,j,m+1}^{n+1}] \right\} / \left(1 + \frac{\Delta t_n}{V_{i,m,j}} C_{i,j,m}^w \right), \quad (3.70b)$$

where

$$A_{i-1/2,j,m}^u = A_{i-1/2,j,m} D_{ur} / (r_i - r_{i-1}), \quad (3.71a)$$

$$A_{i-1/2,j,m}^w = A_{i-1/2,j,m} D_{wr} / (r_i - r_{i-1}), \quad (3.71b)$$

$$B_{i,j,m-1/2}^u = A_{i,j,m-1/2} D_{u\theta} / (r_i \Delta\theta), \quad (3.71c)$$

$$B_{i,j,m-1/2}^w = A_{i,j,m-1/2} D_{w\theta} / (r_i \Delta\theta), \quad (3.71d)$$

$$C_{i,j,m}^u = A_{i-1/2,j,m}^u + A_{i+1/2,j,m}^u + B_{i,j,m-1/2}^u + B_{i,j,m+1/2}^u, \quad (3.71e)$$

$$C_{i,j,m}^w = A_{i-1/2,j,m}^w + A_{i+1/2,j,m}^w + B_{i,j,m-1/2}^w + B_{i,j,m+1/2}^w, \quad (3.71f)$$

2. *Lateral Boundary Nodes:* for $j = 1, 2, \dots, J_p$, and $m = 1, 2, \dots, M_p$.

$$W_{I_p,j,m}^{n+1} = \tilde{C} - \tilde{D} g_1(W_{I_b,j,m}^{n+1}) + \tilde{E} g_2(\tilde{A} + \tilde{B} f_1(W_{I_b,j,m}^{n+1})), \quad (3.72a)$$

$$U_{I_p,j,m}^{n+1} = \tilde{A} + \tilde{B} f_1(W_{I_b,j,m}^{n+1}), \quad (3.72b)$$

where the constants \tilde{A} , \tilde{B} , \tilde{C} , \tilde{D} and \tilde{E} are given as

$$\begin{aligned}
\tilde{A} = & \left[\left((1 - \nu) + \left(\frac{r_{I_b}}{r_{I_p} \Delta r} \right) \rho_0 + \delta_{j,j_0} \frac{\zeta}{\Delta z} \right) U_{I_p,j,m}^n \right. \\
& + \frac{\Delta t_n}{V_{i,j,m}} \left\{ \left((1 - \nu) + \delta_{j,j_0} \frac{\zeta}{\Delta z} \right) \left[A_{I_p-\frac{1}{2},j,m} U_{I_p-1,j,m}^{n+1} \right. \right. \\
& \quad \left. \left. + B_{I_p,j,m-\frac{1}{2}} U_{I_p,j,m-1}^{n+1} + B_{I_p,j,m+\frac{1}{2}} U_{I_p,j,m+1}^{n+1} \right] \right. \\
& + \frac{\rho_0}{\Delta r} \left(\left(A_{I_b,j-\frac{1}{2},m} U_{I_p,j-1,m}^{n+1} + \frac{D u_r}{\Delta r} A_{I_b,j+\frac{1}{2},m} U_{I_p,j+1,m}^{n+1} \right) \left(\frac{D u_r}{\Delta r} \frac{r_{I_b}}{r_{I_p}} \right) \right. \\
& \quad \left. \left. + A_{I_b,j,m-\frac{1}{2}} U_{I_p,j,m-1}^{n+1} + A_{I_b,j,m+\frac{1}{2}} U_{I_p,j,m+1}^{n+1} \right) \right\} \\
& + \Delta t_n \left((1 - \nu) + \delta_{j,j_0} \frac{\zeta}{\Delta z} \right) S_{\min} \Big] / \left[(1 - \nu) + \left(\frac{r_{I_b}}{r_{I_p} \Delta r} \right) \rho_0 \right. \\
& \quad \left. + \delta_{j,j_0} \frac{\zeta}{\Delta z} + \Delta t_n \left\{ \left((1 - \nu) + \delta_{j,j_0} \frac{\zeta}{\Delta z} \right) S_2 + \delta_{j,j_0} \frac{\zeta}{\Delta z} S_0 P \right\} \right. \\
& + \frac{\Delta t_n}{V_{i,j,m}} \left((1 - \nu) + \delta_{j,j_0} \frac{\zeta}{\Delta z} \right) \left(A_{I_p-\frac{1}{2},j,m} + B_{I_p,j,m-\frac{1}{2}} + B_{I_p,j,m+\frac{1}{2}} \right) \\
& \left. + \frac{\rho_0}{\Delta r} \left\{ \left(A_{I_b,j-\frac{1}{2},m} + A_{I_b,j+\frac{1}{2},m} \right) \left(\frac{D u_r}{\Delta r} \frac{r_{I_b}}{r_{I_p}} \right) + A_{I_b,j,m-\frac{1}{2}} + A_{I_b,j,m+\frac{1}{2}} \right\} \right], \tag{3.73a}
\end{aligned}$$

$$\begin{aligned}
\tilde{B} = & \left[\Delta t_n \left((1 - \nu) + \delta_{j,j_0} \frac{\zeta}{\Delta z} \right) S_1 \right] / \left[(1 - \nu) + \left(\frac{r_{I_b}}{r_{I_p} \Delta r} \right) \rho_0 \right. \\
& \quad \left. + \delta_{j,j_0} \frac{\zeta}{\Delta z} + \Delta t_n \left\{ \left((1 - \nu) + \delta_{j,j_0} \frac{\zeta}{\Delta z} \right) S_2 + \delta_{j,j_0} \frac{\zeta}{\Delta z} S_0 P \right\} \right. \\
& + \frac{\Delta t_n}{V_{i,j,m}} \left((1 - \nu) + \delta_{j,j_0} \frac{\zeta}{\Delta z} \right) \left(A_{I_p-\frac{1}{2},j,m} + B_{I_p,j,m-\frac{1}{2}} + B_{I_p,j,m+\frac{1}{2}} \right) \\
& \left. + \frac{\rho_0}{\Delta r} \left\{ \left(A_{I_b,j-\frac{1}{2},m} + A_{I_b,j+\frac{1}{2},m} \right) \left(\frac{D u_r}{\Delta r} \frac{r_{I_b}}{r_{I_p}} \right) + A_{I_b,j,m-\frac{1}{2}} + A_{I_b,j,m+\frac{1}{2}} \right\} \right], \tag{3.73b}
\end{aligned}$$

$$\begin{aligned}
\tilde{C} = & \left[\left\{ (1 - \nu) + \left(\frac{r_{I_b}}{r_{I_p} \Delta r} \right) \rho_0 + \delta_{j,j_0} \frac{\zeta}{\Delta z} \right\} W_{I_p,j,m}^n \right. \\
& \left. + \frac{\Delta t_n}{V_{i,j,m}} \left\{ \left((1 - \nu) + \delta_{j,j_0} \frac{\zeta}{\Delta z} \right) \left(A_{I_p-\frac{1}{2},j,m} W_{I_p-1,j,m}^{n+1} \right. \right. \right.
\end{aligned}$$

$$\begin{aligned}
& + B_{I_p, j, m - \frac{1}{2}} W_{I_p, j, m - 1}^{n+1} + B_{I_p, j, m + \frac{1}{2}} W_{I_p, j, m + 1}^{n+1} \\
& + \frac{\rho_0}{\Delta r} \left(\left(A_{I_b, j - \frac{1}{2}, m} W_{I_p, j - 1, m}^{n+1} + \frac{D w_r}{\Delta r} A_{I_b, j + \frac{1}{2}, m} W_{I_p, j + 1, m}^{n+1} \right) \left(\frac{D_{wr} r_{I_b}}{\Delta r r_{I_p}} \right) \right. \\
& \quad \left. + A_{I_b, j, m - \frac{1}{2}} W_{I_p, j, m - 1}^{n+1} + A_{I_b, j, m + \frac{1}{2}} W_{I_p, j, m + 1}^{n+1} \right) \Bigg] \\
& \quad / \left[(1 - \nu) + \left(\frac{r_{I_b}}{r_{I_p} \Delta r} \right) \rho_0 + \delta_{j, j_0} \frac{\zeta}{\Delta z} \right. \\
& \quad \left. + \frac{\Delta t_n}{V_{i, j, m}} \left((1 - \nu) + \delta_{j, j_0} \frac{\zeta}{\Delta z} \right) \left(A_{I_p - \frac{1}{2}, j, m} + B_{I_p, j, m - \frac{1}{2}} + B_{I_p, j, m + \frac{1}{2}} \right) \right. \\
& \quad \left. + \frac{\rho_0}{\Delta r} \left\{ \left(A_{I_b, j - \frac{1}{2}, m} + A_{I_b, j + \frac{1}{2}, m} \right) \left(\frac{D_{wr} r_{I_b}}{\Delta r r_{I_p}} \right) + A_{I_b, j, m - \frac{1}{2}} + A_{I_b, j, m + \frac{1}{2}} \right\} \right], \tag{3.73c}
\end{aligned}$$

$$D = \left(\frac{\Delta t_n S_{\text{ex}}}{\text{Denominator of } \tilde{C}} \right) \left(\frac{r_{I_b}}{r_{I_p} \Delta r} \right) \rho_0, \tag{3.73d}$$

$$E = \left(\frac{\Delta t_n S_{\text{cG}}}{\text{Denominator of } \tilde{C}} \right) \left(\frac{r_{I_b}}{r_{I_p} \Delta r} \right) \rho_0, \tag{3.73e}$$

Newton Method for (3.68), (3.72)

For $j = 1, 2, \dots, J_p$, $m = 1, 2, \dots, M_p$, and $k = 1, 2, \dots$

$$\begin{aligned}
W_{I_p, j, m}^{n+1; 0} &= W_{I_p, j, m}^n \\
W_{I_p, j, m}^{n+1; k+1} &= W_{I_p, j, m}^{n+1; k} - \frac{G(W_{I_p, j, m}^{n+1; k})}{G'(W_{I_p, j, m}^{n+1; k})}, \quad k = 1, 2, \dots \tag{3.74}
\end{aligned}$$

where

$$G(w) = w - E g_2(A + B f_1(w)) + D g_1(w) - C, \tag{3.75a}$$

$$G'(w) = 1 - B E g_2'(A + B f_1(w)) f_1'(w) + D g_1'(w), \tag{3.75b}$$

with

$$f_1(w) = \frac{1}{1 + (\gamma w)^{m_{\text{Ca}}}}, \quad f_1'(w) = -\frac{\gamma m_{\text{Ca}} (\gamma w)^{m_{\text{Ca}} - 1}}{(1 + (\gamma w)^{m_{\text{Ca}}})^2}, \tag{3.76a}$$

$$g_1(w) = \frac{w}{1+w}, \quad g_1'(w) = \frac{1}{(1+w)^2}, \quad (3.76b)$$

$$g_2(u) = \frac{u^{m_{cG}}}{1+u^{m_{cG}}}, \quad g_2'(u) = \frac{m_{cG} u^{m_{cG}-1}}{(1+u^{m_{cG}})^2}. \quad (3.76c)$$

Split Explicit-Implicit Scheme

Splitting the case for $i = I_p + 1$ separately, we get the following numerical schemes.

1. **Internal Nodes:** for $i = 1, 2, \dots, I_p$, $j = 1, 2, \dots, J_p$, and $m = 1, 2, \dots, M_p$.

$$W_{i,j,m}^{n+1} = W_{i,j,m}^n + \frac{\Delta t_n}{V_{i,j,m}} \left[(A\Phi)_{i-\frac{1}{2},j,m}^{w;n} + (A\Phi)_{i+\frac{1}{2},j,m}^{w;n} + (A\Phi)_{i,j,m-\frac{1}{2}}^{w;n} + (A\Phi)_{i,j,m+\frac{1}{2}}^{w;n} \right], \quad (3.77a)$$

$$U_{i,j,m}^{n+1} = \left[U_{i,j,m}^n + \frac{\Delta t_n}{V_{i,j,m}} \left[(A\Phi)_{i-\frac{1}{2},j,m}^{u;n} + (A\Phi)_{i+\frac{1}{2},j,m}^{u;n} + (A\Phi)_{i,j,m-\frac{1}{2}}^{u;n} + (A\Phi)_{i,j,m+\frac{1}{2}}^{u;n} \right] + \Delta t_n [S_{\min} + S_1 f_1(W_{i,j,m}^{n+1})] \right] / \left[1 + \Delta t_n \left(S_2 + \left(\frac{\zeta \delta_{j,j_0}}{(1-\nu) \Delta z + \zeta \delta_{j,j_0}} \right) S_0 P \right) \right], \quad (3.77b)$$

2. **Lateral Boundary Nodes:** for $j = 1, 2, \dots, J_p$, and $m = 1, 2, \dots, M_p$.

$$U_{I_b,j,m}^{n+1} = \frac{1}{1+D_1} \left\{ U_{I_b,j,m}^n + D_1 U_{I_p,j,m}^{n+1} + \frac{\Delta t_n}{A_{I_b,j,m}} \left[(\beta\Psi)_{I_b,j-\frac{1}{2},m}^{u;n} + (\beta\Psi)_{I_b,j+\frac{1}{2},m}^{u;n} + (\beta\Psi)_{I_b,j,m-\frac{1}{2}}^{u;n} + (\beta\Psi)_{I_b,j,m+\frac{1}{2}}^{u;n} \right] \right\}, \quad (3.78a)$$

$$W_{I_b,j,m}^{n+1} = \frac{C}{Q}, \quad Q = \frac{1}{2} \left(B + \text{sign}(B) \sqrt{B^2 + 4AC} \right), \quad (3.78b)$$

where

$$D_1 = \frac{\Delta t_n}{\rho_o} \left(\frac{D_{ur}}{r_{I_b} - r_{I_p}} \right) \left((1-\nu) + \delta_{j,j_0} \frac{\zeta}{\Delta z} \right), \quad (3.79a)$$

$$D_2 = \frac{\Delta t_n}{\rho_o} \left(\frac{D_{wr}}{r_{I_b} - r_{I_p}} \right) \left((1 - \nu) + \delta_{j,j_0} \frac{\zeta}{\Delta z} \right), \quad (3.79b)$$

$$A = 1 + D_2, \quad (3.79c)$$

$$C = W_{I_b,j,m}^n + \frac{\Delta t_n}{A_{I_b,j,m}} \left[(\beta\Psi)_{I_b,j-\frac{1}{2},m}^{w;n} + (\beta\Psi)_{I_b,j+\frac{1}{2},m}^{w;n} + (\beta\Psi)_{I_b,j,m-\frac{1}{2}}^{w;n} + (\beta\Psi)_{I_b,j,m+\frac{1}{2}}^{w;n} \right] + D_2 W_{I_p,j,m}^{n+1} + \Delta t_n S_{cG} g_2 (U_{I_b,j,m}^{n+1}), \quad (3.79d)$$

$$B = A + \Delta t_n S_{ex} - C. \quad (3.79e)$$

3.3 Stability

Explicit schemes are very simple and convenient from the implementation point of view. However a price is paid by the restriction in time step size to ensure the numerical stability of the scheme. There are various ways to analyse the stability of numerical methods: von Neumann analysis, M matrix method, Positive-coefficient rule. We apply the latter, which ensures positivity of the scheme (Discrete maximum Principle). We rewrite equation (3.29a) in the form

$$U_{i,j}^{n+1} = A_{i,j}^u U_{i-1,j}^n + A_{i+1,j}^u U_{i+1,j}^n + (1 - C_{i,j}^u) U_{i,j}^n + B_{i,j}^u U_{i,j-1}^n + B_{i,j+1}^u U_{i,j+1}^n, \\ n = 1, 2, \dots, N_{\max}, \quad i = 1, 2, \dots, I_p, \quad j = 1, 2, \dots, J_{\max}, \quad (3.80)$$

where

$$A_{i,j}^u = \frac{\Delta t_n}{V_{i,j}} \frac{A_{i-1/2,j}}{(r_i - r_{i-1})} D_{ur}, \quad \text{for } i = 1, 2, \dots, I_p + 1, \quad j = 1, 2, \dots, J_{\max}, \quad (3.81a)$$

$$B_{i,j}^u = \frac{\Delta t_n}{V_{i,j}} \frac{A_{i,j-1/2}}{(z_j - z_{j-1})} D_{uz}, \quad \text{for } i = 1, 2, \dots, I_p, \quad j = 1, 2, \dots, J_{\max} + 1, \quad (3.81b)$$

$$C_{i,j}^u = A_{i,j}^u + A_{i+1,j}^u + B_{i,j}^u + B_{i,j+1}^u, \quad \text{for } i = 1, 2, \dots, I_p, \quad j = 1, 2, \dots, J_{\max}. \quad (3.81c)$$

To ensure positive coefficients in (3.80), we need $C_{i,j}^u \leq 1$, which requires

$$\Delta t_n \leq \frac{0.5}{D_{ur}/\Delta r^2 + D_{uz}/\Delta z^2}. \quad (3.82)$$

Similarly from (3.29a), we get

$$\Delta t_n \leq \frac{0.5}{D_{wr}/\Delta r^2 + D_{wz}/\Delta z^2}. \quad (3.83)$$

Therefore the explicit time step size Δt_{expl} satisfying the Courant-Friedrichs-Lewy (CFL) stability condition for (3.29a), (3.29b) is

$$\Delta t_{\text{expl}} \leq \frac{0.5}{\min \left\{ (D_{ur}/\Delta r^2 + D_{uz}/\Delta z^2), (D_{wr}/\Delta r^2 + D_{wz}/\Delta z^2) \right\}}, \quad (3.84)$$

where

$$\Delta r = \min \left(\frac{R_{\text{disc}}}{I_m}, \frac{R_{\text{rod}} - R_{\text{disc}}}{I_f} \right), \quad \Delta z = \min \left(\frac{\epsilon}{J_m}, \frac{\delta}{2J_f} \right), \quad (3.85a)$$

$$D_{ur} = \frac{\tilde{t}}{\tilde{r}^2} D_{\text{cG}}, \quad D_{uz} = \frac{\tilde{t}}{\tilde{z}^2} D_{\text{cG}}, \quad D_{wr} = \frac{\tilde{t}}{\tilde{r}^2} D_{\text{Ca}}, \quad D_{wz} = \frac{\tilde{t}}{\tilde{z}^2} D_{\text{Ca}}. \quad (3.85b)$$

Using (3.85a), (3.85a) and with $D_{\text{max}} = \max(D_{\text{cG}}, D_{\text{Ca}})$, condition (3.84) takes the form

$$\Delta t_{\text{expl}} \leq \frac{1}{2\tilde{t}D_{\text{max}}} \left(\min \left(\frac{R_{\text{disc}}}{I_m}, \frac{R_{\text{rod}} - R_{\text{disc}}}{I_f} \right)^2 + \min \left(\frac{\epsilon}{J_m}, \frac{\delta}{2J_f} \right)^2 \right).$$

Thus the explicit time-step satisfying the CFL condition is independent of the choice of the the length scales - \tilde{r} and \tilde{z} . This shows that the total number of time steps will be the same for any choice of the scalings. Note that it is the larger of the diffusivities that restricts the time-step.

The CFL restriction for (3.48a) - (3.55) requires:

$$\Delta t_{\text{expl}} < \min \left\{ \frac{\frac{1}{2}}{\frac{D_{ur}}{\Delta r^2} + \frac{D_{u\theta}}{(r_1 \Delta \theta)^2}}, \frac{\frac{1}{2}}{\frac{D_{wr}}{\Delta r^2} + \frac{D_{w\theta}}{(r_1 \Delta \theta)^2}}, \frac{\frac{1}{2}}{\frac{D_{uz}}{\Delta z^2} + \frac{D_{u\theta}}{(r_1 \Delta \theta)^2}}, \frac{\frac{1}{2}}{\frac{D_{wz}}{\Delta z^2} + \frac{D_{w\theta}}{(r_1 \Delta \theta)^2}} \right\}.$$

3.4 Convergence

Consider the general form of the model problem as the following system

$$\frac{\partial u^{(l)}}{\partial t} - D^{(l)} \nabla^2 u^{(l)} = f^{(l)}(x, t, \mathbf{u}), \quad x \in \Omega, t > 0, \quad (3.86a)$$

$$\frac{\partial u^{(l)}}{\partial \nu} + \beta^{(l)} u^{(l)} = g^{(l)}(x, t), \quad x \in \partial\Omega, t > 0, \quad (3.86b)$$

$$u^{(l)}(x, 0) = \psi^{(l)}(x), \quad x \in \Omega, l = 1, 2, \quad (3.86c)$$

where Ω is a bounded domain in \mathbb{R}^3 with boundary $\partial\Omega$, $\frac{\partial}{\partial \nu}$ denotes the outward normal derivative on $\partial\Omega$. It is assumed that the coefficients $D^{(l)} > 0$ in $\Omega \times (0, T]$ for any finite $T > 0$, and $\beta^{(l)} \equiv \beta^{(l)}(x, t)$ are continuous nonnegative on $\partial\Omega \times (0, T]$. It is also assumed that the functions $f^{(l)}$, $g^{(l)}$ and $\psi^{(l)}$ are continuous in their respective domains and $f^{(l)}(\cdot, \mathbf{u})$ is in general nonlinear w.r.to the components of \mathbf{u} .

Numerical analysis of the system of parabolic partial differential equations with nonlinear boundary conditions can be found in [32], [41] etc. Here we follow [41] and quote the convergence theorem to support our computational work. It can be easily verified that our model problems satisfy all the hypothesis of the theorem 3.4.1.

3.4.1 The Finite Difference System

Let $i = (i_1, i_2, i_3)$ be a multiple index with $i_\nu = 1, 2, \dots, M_\nu$ and let $\mathbf{x}_i = (x_{i_1}, x_{i_2}, x_{i_3})$ be a mesh point in $\bar{\Omega}$, where for each $\nu = 1, 2, 3$, M_ν is the total number of mesh points (including possible boundary points) in the x_ν -direction. Denote by \mathcal{M}_p and \mathcal{N}_p the set of mesh points on $\bar{\Omega}$ and $\bar{\Omega} \times (0, T]$ respectively. We assume that the domain $\bar{\Omega}$ is connected. Let $M = M_1 M_2 M_3$ be the total number of mesh points in \mathcal{M}_p . For all $i = 1, \dots, M$, define $u_{i,n}^{(l)} = u^{(l)}(\mathbf{x}_i, t_n)$, $\mathbf{u}_{i,n} = \mathbf{u}(\mathbf{x}_i, t_n)$, $g_{i,n}^{(l)} = g^{(l)}(\mathbf{x}_i, t_n)$,

$\psi_i^{(l)} = \psi^{(l)}(x_i)$, $f_{i,n}^{(l)}(\mathbf{u}_{i,n}) = f^{(l)}(\mathbf{x}_i, t_n, \mathbf{u}(\mathbf{x}_i, t_n))$, ($l = 1, 2$). Let $k_n = t_n - t_{n-1}$ be the time increment and h_ν the spatial increment in x_ν -direction. For each $l = 1, 2$, $n = 1, 2, \dots$, we define vectors $U_n^{(l)} = (u_{1,n}^{(l)}, \dots, u_{M,n}^{(l)})'$, $\mathbf{U}_n = (U_n^{(1)}, U_n^{(2)})'$, $\mathcal{F}^{(l)}(\mathbf{U}_n) = (f_{1,n}^{(l)}(\mathbf{U}_n), \dots, f_{M,n}^{(l)}(\mathbf{U}_n))'$, $\psi^{(l)} = (\psi_1^{(l)}, \dots, \psi_M^{(l)})'$, where $(\cdot)'$ denotes the transpose of a row vector.

Then the discretized form of the system (3.86) with Backward Euler in time stepping takes the form

$$(I + k_n A_n^{(l)}) U_n^{(l)} = U_{n-1}^{(l)} + k_n F^{(l)}(\mathbf{U}_n) + G_n^{(l)}, \quad (3.87a)$$

$$U_0^{(l)} = \psi^{(l)}, \quad l = 1, 2, \quad (3.87b)$$

where $A_n^{(l)}$ is an $M \times M$ matrix which is associated with the PDEs and the L.H.S. of the BCs, and $G_n^{(l)}$ is a vector arising from the boundary function $(g_{1,n}^{(l)}, \dots, g_{M,n}^{(l)})$.

Let $q = 2M$ and define

$$\chi^q = \{U = (U^{(1)}, U^{(2)})', U^{(l)} \in \mathbb{R}^M, l = 1, 2\}.$$

Definition 3.4.1. *Two vectors $\bar{\mathbf{U}}_n \equiv (\bar{U}_n^{(1)}, \bar{U}_n^{(2)})'$, $\mathbf{U}_n \equiv (U_n^{(1)}, U_n^{(2)})'$ in χ^q are called upper and lower solutions of (3.91) if $\mathbf{U}_n \leq \bar{\mathbf{U}}_n$ and*

$$(I + k_n A_n^{(l)}) \bar{U}_n^{(l)} \geq \bar{U}_{n-1}^{(l)} + k_n F^{(l)}(\bar{\mathbf{U}}_n) + G_n^{(l)}, \quad (3.88a)$$

$$(I + k_n A_n^{(l)}) U_n^{(l)} \leq U_{n-1}^{(l)} + k_n F^{(l)}(\mathbf{U}_n) + G_n^{(l)}, \quad (3.88b)$$

$$\bar{U}_0^{(l)} \geq \psi^{(l)} \geq U_0^{(l)} \quad l = 1, 2, \quad (3.88c)$$

In the above definition, inequalities between the vectors are always component-wise.

For a given pair of coupled upper and lower solutions $\bar{\mathbf{U}}_n, \underline{\mathbf{U}}_n$ we set

$$\begin{aligned} \langle \underline{\mathbf{U}}_n, \bar{\mathbf{U}}_n \rangle &\equiv \{ \mathbf{U}_n \in \mathcal{X}^q : \underline{\mathbf{U}}_n \leq \mathbf{U}_n \leq \bar{\mathbf{U}}_n \}, \\ \langle \underline{U}_n^{(l)}, \bar{U}_n^{(l)} \rangle &\equiv \left\{ U_n^{(l)} \in \mathcal{X}^q : \underline{U}_n^{(l)} \leq U_n^{(l)} \leq \bar{U}_n^{(l)} \right\}, \end{aligned}$$

and make the following hypothesis on $A_n^{(l)}$ and $F^{(l)}(\mathbf{U}_n)$

(H1) For each $l = 1, 2$ and $n = 1, 2, \dots$ the matrix $A_n^{(l)} \equiv \left(a_n^{(l)} \right)_{ij}$ is *irreducible*, and

$$\left(a_n^{(l)} \right)_{ii} > 0, \left(a_n^{(l)} \right)_{ij} \leq 0 \text{ for } j \neq i \text{ and}$$

$$\sum_{j=1}^M \left(a_n^{(l)} \right)_{ij} \geq 0 \quad \text{for all } i = 1, 2, \dots, M. \quad (3.89)$$

(H2) The vector function $\mathcal{F}(\mathbf{U}_n) = (F^{(1)}(\mathbf{U}_n), F^{(2)}(\mathbf{U}_n))$ is a C^1 -function and possesses a quasimonotone property in $J \equiv \langle \underline{\mathbf{U}}_n, \bar{\mathbf{U}}_n \rangle$.

Note: The hypothesis (H1) implies that $A_n^{(l)}$ is an M matrix and its smallest eigen value $\mu_n^{(l)}$ is real and nonnegative, and if $k_n > 0$ then $(I + k_n A_n^{(l)})^{-1}$ exists and is a positive matrix [19]. In fact, if the strict inequality in (3.89) holds for at least one i , then $\mu_n^{(l)} > 0$ and $(A_n^{(l)})^{-1}$ exists and is a positive matrix. The connectedness assumption on the $\bar{\Omega}$ ensures that $A_n^{(l)}$ is *irreducible*.

3.4.2 Construction of Monotone Iterative Scheme

Let $\gamma_{i,n}^{(l)}$ be any nonnegative function on \mathcal{N}_p satisfying

$$\gamma_{i,n}^{(l)} \geq \max \left\{ -\frac{\partial f^{(l)}(x_i, t_n, \mathbf{U}_n)}{\partial u^{(l)}} : \underline{\mathbf{U}}_n \leq \mathbf{U}_n \leq \bar{\mathbf{U}}_n, l = 1, 2 \right\}. \quad (3.90)$$

Define the matrices $\mathcal{A}_n^{(l)} \equiv I + k_n (A_n^{(l)} + \Gamma_n^{(l)})$, $\Gamma_n^{(l)} \equiv \text{diag} (\gamma_{1,n}^{(l)}, \dots, \gamma_{M,n}^{(l)})$. Then the system (3.91) can be written as

$$\mathcal{A}_n^{(l)} U_n^{(l)} = U_{n-1}^{(l)} + k_n (\Gamma_n^{(l)} U_n^{(l)} + F^{(l)}(\mathbf{U}_n)) + G_n^{(l)}, \quad (3.91a)$$

$$U_0^{(l)} = \psi^{(l)}, \quad l = 1, 2. \quad (3.91b)$$

Consider the following Picard type iterative scheme,

$$\mathcal{A}_n^{(l)} (\bar{U}_n^{(l)})^{(m)} = \left(\bar{U}_{n-1}^{(l)} \right)^{(m)} + k_n \left(\Gamma_n^{(l)} (\bar{U}_n^{(l)})^{(m)} + F^{(l)}((\bar{\mathbf{U}}_n))^{(m)} \right) + G_n^{(l)}, \quad (3.92a)$$

$$\mathcal{A}_n^{(l)} (\underline{U}_n^{(l)})^{(m)} = \left(\underline{U}_{n-1}^{(l)} \right)^{(m)} + k_n \left(\Gamma_n^{(l)} (\underline{U}_n^{(l)})^{(m)} + F^{(l)}((\underline{\mathbf{U}}_n))^{(m)} \right) + G_n^{(l)}, \quad (3.92b)$$

$$\left(\bar{U}_0^{(l)} \right)^{(m)} = \left(\underline{U}_0^{(l)} \right)^{(m)} = \psi^{(l)}, \quad l = 1, 2, \quad m = 1, 2, \dots, \quad (3.92c)$$

where $\left(\bar{U}_n^{(l)} \right)^{(0)} = \bar{U}_n^{(l)}$, $\left(\underline{U}_n^{(l)} \right)^{(0)} = \underline{U}_n^{(l)}$.

In the above iteration process, n is fixed and the iteration is with respect to m starting from $m = 1$. Since $\left(\mathcal{A}_n^{(l)} \right)^{-1}$ exists and for each m right hand side of (3.92) is known, the maximal and minimal sequences $\left\{ \bar{U}_n^{(m)} \right\}$, $\left\{ \underline{U}_n^{(m)} \right\}$ are well defined and can be computed by solving a linear algebraic system.

3.4.3 Convergence of Finite Difference Solutions

In [41], the sequences of iterations (3.92) are shown to converge monotonically to a unique solution of the system (3.91). Then the monotone convergence of the maximal and minimal sequences for the system by the Picard iteration process (3.92) is used to prove the convergence of the finite difference solution of (3.91) to the continuous solution of (3.86) as the mesh size decreases to zero.

Theorem 3.4.1. [41, p. 400] *Let $((\bar{\mathbf{u}}(\mathbf{x}_i, t), (\underline{\mathbf{u}}(\mathbf{x}_i, t))$ and $(\bar{\mathbf{u}}_{i,n}, \underline{\mathbf{u}}_{i,n})$ be coupled upper and lower solutions of (3.86) and (3.91) respectively, and let $\bar{\mathbf{u}}(\mathbf{x}_i, t) = \bar{\mathbf{u}}_{i,n}$, $\underline{\mathbf{u}}(\mathbf{x}_i, t) = \underline{\mathbf{u}}_{i,n}$ in a fixed discretized domain \mathcal{N}_p^* . Assume that $\beta^{(l)}(\mathbf{x}_i, t) \not\equiv 0$ and hypothesis (H1), (H2) hold. Then the solution $\underline{\mathbf{u}}_{i,n}$ converges to the solution $\bar{\mathbf{u}}(\mathbf{x}_i, t)$ on \mathcal{N}_p^* as $k + |h| \rightarrow 0$, where $k = \max(k_n)$ and $h = |h_1| + |h_2| + |h_3|$.*

Grid Convergence

In the simulations reported here, we employ a fairly fine grid consisting of: $I_m = 64$ nodes in $[0, R_{\text{disc}}]$; $I_f = 4$ nodes in $[R_{\text{disc}}, R_{\text{rod}}]$ along the disc radius; $J_f = 1$ node below the disc, $J_m = 2$ nodes along the height of each disc, and $J_f = 1$ node above the disc. Thus, each disc unit is discretized into $64+4 \times 4+4 = 272$ control volumes, resulting in $272 \times 800 = 217600$ control volumes for a typical rod with $N_{\text{disc}} = 800$ discs. Finer grids were tested, with no discernible effect (to at least 3 significant digits).

For the homogenized problem in simpler geometry, we have also applied the spatially adaptive mesh. The grid convergence tests shows that we could get the satisfactory qualitative solutions with much less computational efforts.

3.5 Parallelization via Domain Decomposition

The problem involves very intensive computations. We parallelize the scheme for distributed memory clusters of processors or heterogeneous networked computers. Since there is no functional parallelism in solving the partial differential equations, the natural data parallelization via domain decomposition method has been used. The idea is to decompose the spatial domain into sections and assign a section to each processor. Here a section consists of a group of disc units (see Fig 3.1). The parallel implementation was done using the MPI (Message Passing Interface) library. We followed the master/slaves paradigm generated in SIMD (Single Instruction Multiple Data) mode, where one processor acts as a master and the rest as slaves. The master loads I/O, distributes tasks to the slaves, controls and synchronizes the slaves whereas the slaves all solve the same problem but on their own segment of the mesh, exchange

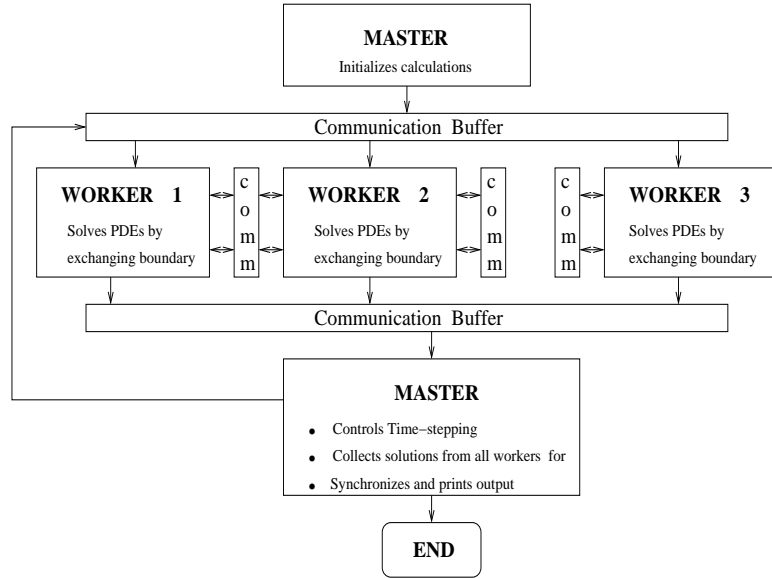


Figure 3.2: Parallel implementation scheme

boundary values among their neighbors and send their output to the master. The parallel implementation scheme is shown in Fig. 3.2.

3.5.1 Speedup

For a given problem and a parallel computer with N_P processors, the speedup is defined as

$$S = T_S/T_P, \tag{3.93}$$

where T_S is the wallclock time required to solve the given problem by the best available sequential algorithm on one processor and T_P is the wallclock time required to solve the problem by a parallel algorithm on N_P processors. Another commonly used definition for speedup is

$$S = T_1/T_P, \tag{3.94}$$

where T_1 and T_P are the wallclock times used by the same parallel algorithm to solve the given problem on one and N_P processors, respectively. Since we followed master/workers (SIMD) paradigm for the parallel implementation of the codes, which requires at least two processors (one master and one worker) to run the code, we make the convention that N_P refers to the number of worker processors.

In order to get consistent speedup measures, one has to have an exclusive access to the parallel computer being used. Otherwise, depending on the system load, the times T_1 and T_P will be different for different runs if the computer is shared by many users. The speedup S of a parallel algorithm running on a parallel computer measures the reduction of the computing time originally used by the sequential algorithm on one processor for solving the same problem. A speedup of $S = 10$ means the solution can be obtained with multiple processors in 1/10 of the original time required by a single processor computer. It is noteworthy that the speedups calculated from the above two formulae (3.93), (3.94) are usually different because T_S and T_1 are usually different. To take advantage of multiple processors on a parallel computer, we have to reconstruct the sequential algorithm developed for a single processor computer and schedule as many computations in parallel as possible. Because of this, we usually have $T_1 \geq T_S$ in general. The numerical complexity of a parallel algorithm is usually higher than that of the sequential algorithm for the same problem. As long as the reduction of computing time by using multiple processors is more than what is needed to counterbalance the increase of computing time due to the higher numerical complexity of the parallel algorithm, it is worthwhile using parallel computers so solutions can be calculated faster.

3.5.2 Efficiency

The efficiency of a parallel algorithm running on a parallel computer with N_P processors is defined as

$$e = S/N_P, \quad (3.95)$$

where S is the speedup. The efficiency e measures the effective utilization of all processors by a parallel algorithm, or the portion of time a processor is doing useful work for solving the given problem during the algorithm execution. The higher the efficiency, the better a parallel computer is utilized by a parallel algorithm. In an ideal case, if the algorithm is perfectly parallelizable, one would expect a N_P -fold speedup if N_P processors are used, or in other words, the problem can be solved in $1/N_P$ of the original time required by one processor. In this case, the efficiency will be $e = S/N_P = N_P/N_P = 1$, which means all processors are busy all the time in the execution doing useful work for solving the given problem. In general the speedup S is less than N_P due to the parallel overhead, higher numerical complexity, synchronizations, and nonparallelizable part of the problem. Thus, we generally get $e < 1$.

3.5.3 Runtime Tests

To estimate the parallel speed-up we have measured the execution time T_P necessary for performing a fixed computation on different machines. The parallel performance results (speedup S and the corresponding efficiency e) are given in Tables 3.1 - 3.3 . These results are based on the wall clock time of a computation on runs for a fixed grid size ($I_p = 6$, $I_f = 4$, $J_p = 4$, $J_f = 2$ which means $(6 + 4) \times (4 + 4) = 80$ nodes per disc unit) with 100, 200 and 400 discs, and total simulation time $t_{\max} = 1$ sec.

Table 3.1: Speedup and Efficiency on colt with 100 discs

machine	N_P	CPU (sec)	time (hr:min)	S	e
colt	1	16243.0	5 : 22	—	—
colt	5	3507	1 : 34	4.631	0.926
colt	10	2008	1 : 20	8.089	0.808

Table 3.2: Speedup and Efficiency on various machines with 200 discs

machine	N_P	CPU (sec)	time (hr:min)	S	e
cheetah	1	32486	9 : 02	—	—
colt	1	40278	11 : 12	—	—
eagle	1	73714	20 : 21	—	—
cheetah	5	7014	1 : 57	4.631	0.926
colt	5	9437	2 : 37	4.268	0.853
eagle	5	18057	5 : 00	4.082	0.816
cheetah	10	4016	1 : 07	8.089	0.808
colt	10	6806	1 : 53	5.918	0.591
eagle	10	12975	3 : 36	5.681	0.568

Table 3.3: Speedup and Efficiency on various machines with 400 discs

machine	N_P	CPU (sec)	time (hr:min)	S	e
cheetah	1	63668	17 : 42	—	—
colt	1	78424	21 : 47	—	—
cheetah	5	13233	3 : 41	4.811	0.962
colt	5	18239	5 : 04	4.299	0.859
cheetah	10	7161	1 : 59	8.890	0.889
colt	10	10729	2 : 59	7.309	0.730
cheetah	20	4131	1 : 09	15.412	0.770
colt	20	6930	1 : 55	11.316	0.566
colt	40	5201	1 : 26	15.078	0.377

Each run executes 12049753 time-steps.

The serial version of the code tested took 5 hr : 25 min on colt for the 1 sec run on the same grid with 100 discs which extrapolates \approx 11 hrs for 200 discs, \approx 22 hrs for 400 discs and \approx 44 hrs for 800 discs. Note that a typical salamander photoreceptor rod has about 800 discs. Thus parallelization is necessary. With 10 processors on colt, the 100 disc simulation took 1 hr : 20 min, exhibiting a speedup of 8 and efficiency 0.8, as shown in Table 3.1. The speedup of colt on the 100, 200 and 400 disc problem is depicted graphically in Fig. 3.3.

Specifications of the Machines and Compilers

- colt.ccs.ornl.gov 64 nodes (256 cpus) and falcon.ccs.ornl.gov 256 nodes (1024 cpus) Compaq AlphaServer SC, 4 SMP CPUs per node, 2GB RAM per node: ES40 processor: 21264a (ev67), 667 MHz, 64KB I-cache, 64KB D-cache, 8MB L2 cache, f90 Compaq Fortran Compiler X5.4A-1684-46B5P
Compiled with: f90 -fast -O5 -tune ev67 -lfmpi -lmpi -lelan
- eagle.ccs.ornl.gov IBM SP 184 4-way Winterhawk II nodes, 4 SMP CPUs per node, 2GB RAM, CPU: Power3-II processor, 375 MHz, 8MB L2 cache, XL Fortran Compiler 7.1.1.2,
Compiled with: mpixlf -O4 -qnoipa
- cheetah.ccs.ornl.gov IBM pSeries System (p690) 27 "Regatta" nodes, each with 32 processors on 16 chips CPU: 1.3 GHz Power4 processor, 64 KB L1 cache, 32 KB D-cache, 1.5 MB L2 cache estimated computational power 4.5 TeraFLOP/s, XL Fortran Compiler version 7.1.1.3
Compiled with: mpixlf-r -g -O4 -qnoipa run from GPFS area

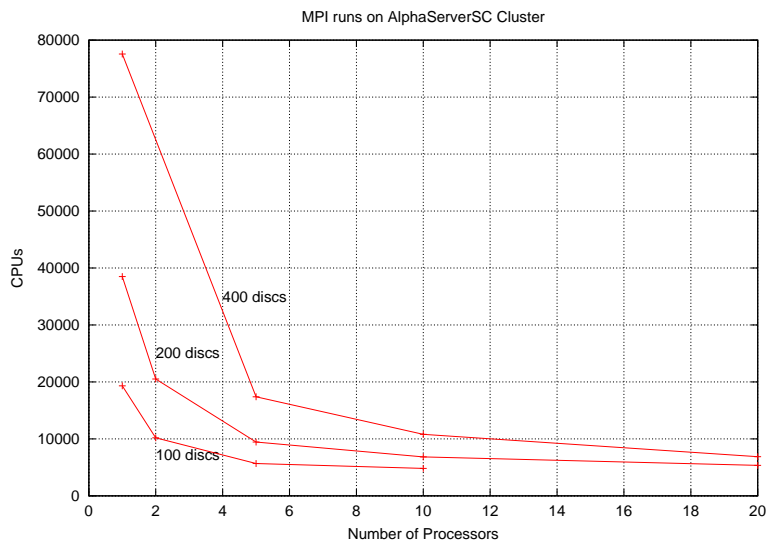
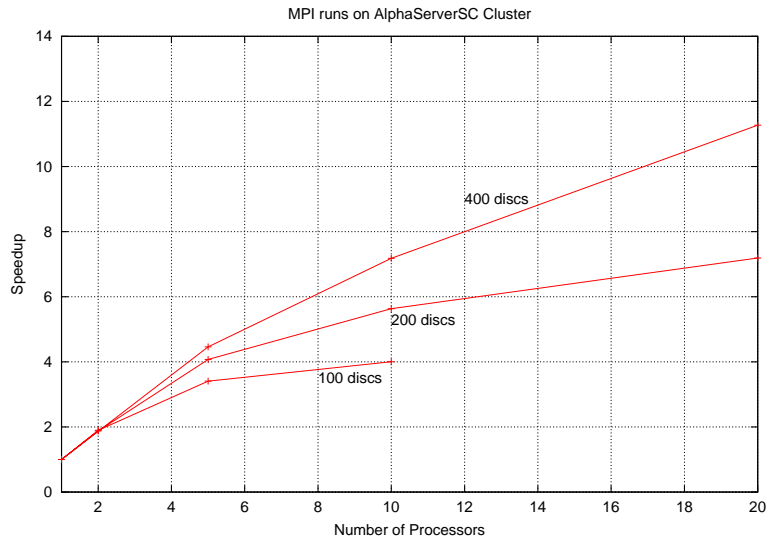


Figure 3.3: Speedup and CPU time (on colt) for 100, 200 and 400 discs.

Chapter 4

Numerical Simulations

The numerical simulations are based on the Computational Models developed in Chapter 3. In phototransduction (where the receiving cell is the photoreceptor, the signal is light, its receptor is rhodopsin and the second messengers are cGMP and Ca^{2+}), we are interested in the study of the cellular response at the photoreceptor's plasma membrane, i.e., a change in current at the photoreceptor's plasma membrane, which changes the cell's electric output and leads to a signal being sent to the brain. The choice of parameters is discussed in detail in §4.1.1, and it is a very serious problem, as there is no general agreement on the values of many of them in the literature. To validate the Mathematical/Computational models, we will compare the numerical results with experimental ones in §4.2.

The simulations can be used to conduct computational experiments for interpretation of available biological data, comparison of model predictions with measurements, determination of sensitivity of output on various model parameters, and design further biological experiments. It can also be used for determining physical parameter values that are difficult, nonfeasible, or impossible to measure directly.

4.1 Choosing Parameters and Scales

4.1.1 Parameters

To simulate a real experiment, we must provide the necessary parameters to the computer program. The definitions of the variables and parameters used in the model are shown in Table 4.1. The parameter values (for **salamander**) used in the simulation, mostly obtained from [44, 35, 34] as described below, are listed in Table 4.1.

There is no general agreement between the various literature values for these constants. We obtained some of the parameters from the literature, some by matching terms in our model and the bulk model of [35, 44], and some by testing many combinations of parameters attempting to match the peak response and the time at which it occurs with experimental data.

Rate Constants

Here we describe in detail how some of the parameter values were obtained by matching with those in the bulk ODE model of [35], hereafter named NLP for brevity.

The z -flux in (2.8a) expresses the cGMP flow rate per unit area of disc surface. Integrating (2.8a) over all the disc surfaces we obtain the total flow rate in the entire rod outer segment. For the case of uniform concentrations (as assumed in NLP) the total flow rate is

$$\alpha d \sigma_{\text{disc}} - k_{\text{hyd}} [\text{PDE}]_s [\text{cG}] \sigma_{\text{disc}} - \delta_{i0} k_{\text{hyd}}^* [\text{PDE}^*]_s [\text{cG}] \sigma_{\text{active}} \quad (4.1)$$

In the last term of (4.1), the activated disc area, σ_{active} , appears since it operates only on (one face of) activated disc(s). The corresponding quantity in [35,

Table 4.1: Parameters of the model (for salamander rod)

Symbol	Units [†]	Range of values	Used in Simulation	Reference [‡]
α_{\max}	μMs^{-1}	40-50	50	PL; NLP
$\alpha_{\min}/\alpha_{\max}$	-	0. - 0.02	0.02	PL; NLP
β_{dark}	s^{-1}	-	1	PL; NLP
B_{Ca}	-	10 - 50	20	PL; NLP; [34]
B_{cG}	-	1 - 2	2	PL
$[\text{cG}]_{\text{dark}}$	μM	2 - 4	3	PL; NLP
$[\text{Ca}]_{\text{dark}}$	μM	0.4 - 0.7	0.65	PL; NLP
d	μm	-	0.007	§2.2
D_{Ca}	$\mu\text{m}^2 \text{s}^{-1}$	15	15	[33]
D_{cG}	$\mu\text{m}^2 \text{s}^{-1}$	50 - 196	60	[22, 37]
δ, ϵ	μm	0.01 - 0.014	0.014	PL
f_{Ca}	-	0.1 - 0.2	0.17	PL; NLP
\mathcal{F}	C mol^{-1}	96500	96500	PL; NLP
H	μm	20 - 28	22.4	PL
J_{dark}	pA	-	66	§3.3
$j_{\text{ex}}^{\text{sat}}$	pA	17 - 20	17	PL
$j_{\text{cG}}^{\text{max}}$	pA	70 - 7000	7000	NLP
k_{E}	s^{-1}	0.58-0.76	0.67	[34]
k_{hyd}	$\mu\text{M}^{-1} \text{s}^{-1}$	-	0.4214	§4.1
k_{hyd}^*	$\mu\text{M}^{-1} \text{s}^{-1}$	-	1.827×10^{-20}	§4.1
$k_{\text{cat}}/K_{\text{m}}$	$\mu\text{M}^{-1} \text{s}^{-1}$	440	440	PL; NLP
k_{R}	s^{-1}	1.69 - 3.48	2.56	[34]
K_{cyc}	μM	0.10 - 0.23	0.135	PL; NLP
K_{cG}	μM	13 - 32	32	PL; NLP
K_{ex}	μM	1.5, 1.6	1.5	PL; NLP
m_{cG}	-	2	2	PL
m_{cyc}	-	2 - 3	2	PL; NLP; [23]
ν_{RE}	s^{-1}	150, 220	675	PL; NLP; §4.1
N_{AV}	mol^{-1}	602×10^{21}	602×10^{21}	-
N_{disc}	-	~ 1000	800	PL; NLP
$[\text{PDE}]_s$	$\# \mu\text{m}^{-2}$	100	100	PL; [18]
R_{disc}	μm	5.5	5.5	PL
R_{rod}	μm	5.515	5.515	PL
σ_1	μm^2	95	95	PL
Σ_{rod}	μm^2	-	776	PL
t_{RGE}	ms	10 - 30	15	PL; NLP; [34]
V_{cyto}	μm^3	1000	1076	PL

[†]The symbol # stands for number of molecules, and a dash “-” signifies dimensionless quantity.

[‡]The symbols “PL” and “NLP” are abbreviations for [44] and [35] respectively.

equation (A3), p. 819] is

$$(\alpha - \beta [\text{cG}]) V_{\text{cyto}}, \quad \text{where } \beta = \beta_{\text{dark}} + \beta_{\text{sub}} E^* \quad (4.2)$$

is the rate constant of cGMP hydrolysis, β_{dark} is the rate constant in darkness and β_{sub} is the rate constant per E^* subunit. From (4.2), the total flow rate of NLP is

$$\alpha V_{\text{cyto}} - \beta_{\text{dark}} [\text{cG}] V_{\text{cyto}} - \beta_{\text{sub}} E^* [\text{cG}] V_{\text{cyto}}. \quad (4.3)$$

Note that $V_{\text{cyto}} = d \sigma_{\text{disc}}$. Comparing the corresponding terms of (4.1) and (4.3), we see that the first terms match. From the second term:

$$\begin{aligned} k_{\text{hyd}} [\text{PDE}]_s \sigma_{\text{disc}} &= \beta_{\text{dark}} V_{\text{cyto}} && [\mu\text{m}^3 \text{s}^{-1}] \\ \implies k_{\text{hyd}} &= d \beta_{\text{dark}} / [\text{PDE}]_s && [\text{molecules}^{-1} \mu\text{m}^3 \text{s}^{-1}] \end{aligned} \quad (4.4)$$

From the third term:

$$k_{\text{hyd}}^* = \beta_{\text{sub}} V_{\text{cyto}} \quad [\text{molecules}^{-1} \mu\text{m}^3 \text{s}^{-1}], \quad (4.5)$$

$$\text{and } [\text{PDE}^*]_s = \frac{E^*}{\sigma_{i0}} \quad [\text{molecules } \mu\text{m}^{-2}]. \quad (4.6)$$

The expression for β_{sub} from [NLP] is

$$\beta_{\text{sub}} = \frac{\frac{1}{2} k_{\text{cat}} / K_m}{V_{\text{cyto}} N_{\text{Av}} B_{\text{cG}}}, \quad (4.7)$$

where k_{cat} / K_m is hydrolytic efficacy of fully-activated PDE dimer and N_{Av} is Avogadro's number.

Using the values of the parameters from the Table 4.1, we obtain the following matching parameters:

$$\begin{aligned} \alpha_{\text{max}} &= 50 \mu\text{Ms}^{-1}, \quad \alpha_{\text{min}} = 1 \mu\text{Ms}^{-1}, \\ k_{\text{hyd}} &= \beta_{\text{dark}} d / [\text{PDE}]_s = \frac{(1)(0.007)}{100} = 7 \times 10^{-5} \text{ molecules}^{-1} \mu\text{m}^3 \text{s}^{-1}, \end{aligned}$$

$$k_{\text{hyd}}^* = \beta_{\text{sub}} V_{\text{cyto}} = \frac{\frac{1}{2} k_{\text{cat}}/K_m}{N_{\text{Av}} B_{\text{cG}}} = \frac{(\frac{1}{2})(440)}{(602 \times 10^{21}) (2)} = \frac{110}{602} \text{ molecules}^{-1} \mu\text{m}^3 \text{s}^{-1}.$$

The factor 602 in the value of k_{hyd}^* comes from unit conversion:

$$1 \mu\text{M} = 1 \times 10^{-6} \text{ mol L}^{-1} = 1 \times 10^{-21} \text{ mol } \mu\text{m}^{-3} = 602 \text{ molecules } \mu\text{m}^{-3}.$$

Diffusion Coefficients

The effective longitudinal diffusion coefficient D_x of cGMP, which is measured in experiments, [22, 24, 18, 37], can be related to the the cytoplasmic diffusion coefficient D_{cG} , by the following relation ([37, 4]),

$$D_x = (F_A/F_V) D_{\text{cG}}, \quad (4.8)$$

where the ratio (F_A/F_V) of the effective cross-sectional area to the effective volume available for longitudinal diffusion is a geometric factor giving a measure of tortuosity, the physical hinderance to longitudinal diffusion arising from the disc stack. Work in [37] has estimated $F_A \approx 0.014$, $F_V \approx 0.5$, so $F_A/F_V \approx 0.028$ (accounting for “incisures” of discs), and deduced that the effective longitudinal coefficient D_x is 1.4 - 5.5 $\mu\text{m}^2 \text{s}^{-1}$. Hence the diffusion coefficient for cGMP is estimated to be in the range

$$D_{\text{cG}} = (F_V/F_A) D_x \approx 50 - 196 \mu\text{m}^2 \text{s}^{-1}. \quad (4.9)$$

On the other hand, [22] reports a range 30 - 60 $\mu\text{m}^2 \text{s}^{-1}$. We tested both a low-end value, 60, and a high-end value, 190, and found that $D_{\text{cG}} = 60 \mu\text{m}^2 \text{s}^{-1}$ produces a response that agrees better (§5) with the experimental data of [45].

The diffusion coefficient of calcium in cytosol, $D_{\text{Ca}} = 15 \mu\text{m}^2 \text{s}^{-1}$, is taken from the recent work of [33]. This value accounts for buffering effects on calcium.

4.1.2 Dark Steady-State

In the absence of light the system admits a uniform steady state, $u = u_0$ and $w = w_0$ for some positive constants u_0 and w_0 - thus our initial condition is this dark equilibrium state. The steady state solution u_0, w_0 of (2.33), (2.34) making all boundary fluxes $F_{ur} = F_{wr} = F_{uz} = F_{wz} = 0$ satisfies the following relations

$$\begin{cases} g_1(w_0) - C_{\text{ratio}} g_2(u_0) = 0, \\ C_{\text{min}} + C_1 f_1(w_0) - C_2 u_0 = 0. \end{cases} \quad (4.10)$$

Using the definition of the functions f_1, g_1, g_2 from (2.35) and dividing by C_2 , (4.10) take the form

$$\begin{cases} 1 + \frac{1}{u_0^{m_{cG}}} = C_{\text{ratio}} \left(1 + \frac{1}{w_0}\right) = 0, \\ u_0 = \frac{C_{\text{min}}}{C_2} + \left(\frac{1}{1 + (\gamma w_0)^{m_{Ca}}}\right). \end{cases} \quad (4.11)$$

Eliminating u , we solve the equation

$$\left(\frac{C_{\text{min}}}{C_2} + \frac{C_1}{C_2} \left(\frac{1}{1 + (\gamma w_0)^{m_{Ca}}}\right)\right)^{-m_{cG}} = C_{\text{ratio}} \left(1 + \frac{1}{w_0}\right) - 1, \quad (4.12)$$

for $w_0 > 0$ with the Bisection Method and then obtain u_0 from the second equation. Note that, since only ratios of the constants C_{min}, C_1 and C_2 appear, the roots u_0, w_0 of (4.10) are scale independent.

$$\text{L.H.S.}|_{w_0=0} = \left(\frac{C_{\text{min}}}{C_2} + \frac{C_1}{C_2}\right)^{-m_{cG}}, \quad (4.13)$$

$$\text{L.H.S.}|_{w_0=\infty} = \left(\frac{C_{\text{min}}}{C_2}\right)^{-m_{cG}}. \quad (4.14)$$

Thus there exists a root $w_0 > 0$ of (4.12), if

$$(C_2/C_{\text{min}})^{m_{cG}} > C_{\text{ratio}} - 1. \quad (4.15)$$

Using the definitions of C_{\min} , C_{ratio} and C_2 from (2.36), the condition (4.15) takes the form

$$\alpha_{\min} < \frac{1}{d} \tilde{u} k_{\text{hyd}} [\text{PDE}]_s (C_{\text{ratio}} - 1)^{-1/m_{\text{cG}}}. \quad (4.16)$$

Substituting the values of the parameters ($\delta = 0.014 \mu\text{m}$, $\tilde{u} = K_{\text{cG}} = 32 \mu\text{M}$, $k_{\text{hyd}} = 7 \times 10^{-5} \text{ molecules}^{-1} \mu\text{m}^3 \text{ s}^{-1}$, $[\text{PDE}]_s = 100 \text{ molecules} \mu\text{m}^{-2}$, $C_{\text{ratio}} = 35$, and $m_{\text{cG}} = 2$), we get the upper bound for α_{\min} necessary for existence of a uniform steady-state

$$\alpha_{\min} \leq 5.49. \quad (4.17)$$

The [NLP] value for α_{\min} is 1 which satisfies (4.17). It is clear from (4.15) that for $\alpha_{\min} = 0$ ($C_{\min} = 0$, $C_{\text{ratio}} = 35$, $C_2 > 0$, $m_{\text{cG}} = 2$) the uniform steady-state can always be obtained. With the [NLP] values we find the steady-state $[\text{cG}]_{\text{dark}} = 2.91 \mu\text{M}$, $[\text{Ca}]_{\text{dark}} = 0.60 \mu\text{M}$. This is slightly less than the [NLP] dark values of 3, 0.64. By taking $K_{\text{cyc}} = 0.165$, we find the more agreeable values of 2.99, 0.65 .

The highest sensitivity of the root u_0 , w_0 was noticed on K_{cyc} , then on k_{hyd} , then on m_{Ca} , and then on m_{cG} .

4.1.3 PDE Activation - Setting the Light Source

Activation via a Gaussian

We want the entire disc to be activated within a certain time interval $[0, T]$. Since three standard deviations (s.d.) contains 99% of the gaussian in equation (2.20), we want $3 \text{ s.d.} \approx R_{\text{disc}}$ at time T . The gaussian in (2.20) has standard deviation $\text{s.d.} = \sqrt{4D_{\text{a}}(t - t_{\text{on}})}$, hence $D_{\text{a}} = R_{\text{disc}}^2 / (36T) \mu\text{m}^2 \text{ s}^{-1}$. Thus, for $T = 1 \text{ sec}$, $D_{\text{a}} \approx 1 \mu\text{m}^2 \text{ s}^{-1}$, for $T = 0.1 \text{ sec}$, $D_{\text{a}} \approx 8 \mu\text{m}^2 \text{ s}^{-1}$.

One photon is expected to activate about 1000 molecules of PDE* (1 photon $\longrightarrow 1 R^* \longrightarrow 10^2 - 10^3 T^* \longrightarrow 10^2 - 10^3 \text{ PDE}^*$, see [25, 18]). Thus, a flash delivering

Φ photoisomerizations to the rod is expected to activate about 1000 Φ molecules of PDE. Each activated disc contains $\sigma_1 \cdot [\text{PDE}]_s$ molecules, therefore the number of activated discs is

$$N_{\text{active}} = \text{Integer} \{1000 \Phi / (\sigma_1 \cdot [\text{PDE}]_s)\} + 1. \quad (4.18)$$

Distributing the 1000 Φ equally among the N_{active} discs, we get the number of PDE* molecules on each activated disc as

$$P_0 = 1000 \Phi / N_{\text{active}}. \quad (4.19)$$

Activation via a Lumped Model

The number of PDE* molecules in the entire rod obtained from (2.22) or (2.25b) is distributed uniformly to a specified number N_{active} of activated discs. For example, the function $E^*(t)$ in (2.22) has maximum

$$E_{\text{max}}^* = \Phi \cdot \left(\frac{\nu_{\text{RE}}}{k_{\text{E}}}\right) \left(\frac{k_{\text{R}}}{k_{\text{E}}} - 1\right) \left(\frac{k_{\text{E}}}{k_{\text{R}}}\right) \frac{1}{1 - k_{\text{E}}/k_{\text{R}}}, \quad (4.20)$$

which is the maximum number of PDE* molecules in the entire rod outer segment.

The number from $E^*(t)$ in (2.25b) is given by

$$\begin{aligned} E_{\text{max}}^* = & I \cdot \frac{\nu_{\text{RE}}}{k_{\text{E}} k_{\text{R}} (k_{\text{R}} - k_{\text{E}})} [k_{\text{R}} (1 - e^{-k_{\text{E}} \Delta t_{\text{flash}}}) - k_{\text{E}} (1 - e^{-k_{\text{R}} \Delta t_{\text{flash}}})] \\ & - I \cdot \frac{\nu_{\text{RE}}}{k_{\text{E}} k_{\text{R}} (k_{\text{R}} - k_{\text{E}})} \left[k_{\text{E}} (1 - e^{-k_{\text{R}} \Delta t_{\text{flash}}}) \left(\frac{k_{\text{R}}}{k_{\text{E}}} - 1\right) \left(\frac{k_{\text{E}}}{k_{\text{R}}}\right) \frac{1}{1 - k_{\text{E}}/k_{\text{R}}} \right]. \end{aligned} \quad (4.21)$$

Since there are $\sigma_1 \cdot [\text{PDE}]_s$ available PDE molecules on each activated disc, we must have

$$N_{\text{active}} \geq \text{Integer} \{E_{\text{max}}^* / (\sigma_1 \cdot [\text{PDE}]_s)\} + 1. \quad (4.22)$$

Then, at any time t , the surface density of activated PDE molecules is given by (2.6). For the rate constants from [35] ($\nu_{RE} = 220 \text{ s}^{-1}$, $k_E = 0.625 \text{ s}^{-1}$, $k_R = 2.857 \text{ s}^{-1}$) and $\Phi = 1$, we get $E_{\max}^* \approx 50$. Thus a single photoisomerization ($\Phi = 1$), activates a single disc (partially) and by (2.6) the maximum surface density of PDE* on the face of the activated disc is $[\text{PDE}^*]_{s,\max} = E_{\max}^*/(\sigma_1 \cdot N_{\text{active}}) \approx 0.53 \text{ molecules } \mu\text{m}^{-2}$. A simulation with these rate constants produced a very low response. Increasing ν_{RE} to 500 s^{-1} , the response increased to 0.8% at time 800 ms, which agrees with [45]; however, the peak of the response in the simulation occurs later (at 930 ms) than in the experiment ($\sim 800 \text{ ms}$). A set of rate constants that produces good agreement with Rieke's experiment were found to be $\nu_{RE} = 675 \text{ s}^{-1}$, $k_E = 0.67 \text{ s}^{-1}$, $k_R = 2.56 \text{ s}^{-1}$ (when $D_{cG} = 60 \mu\text{m}^2 \text{ s}^{-1}$ and $B_{Ca} = 20$). These correspond to the average values of time constants ($1/k_E = \tau_E = 1.9 \text{ s}$, $1/k_R = \tau_R = 0.48 \text{ s}$) given in Table IV of [34], but ν_{RE} is three times larger. Taking $D_{cG} = 190 \mu\text{m}^2 \text{ s}^{-1}$ (the high end value in (4.9), $\nu_{RE} = 360 \text{ s}^{-1}$ would suffice, but then again the peak response occurs late. Thus we use $D_{cG} = 60 \mu\text{m}^2 \text{ s}^{-1}$ and $\nu_{RE} = 675 \text{ s}^{-1}$ in the simulations.

Histories of activated rhodopsin, $R^*(t)$, and PDE molecules, $E^*(t)$, as predicted from (2.24) and (2.25) are shown in Fig 4.1 .

The value of activation rate ν_{RE} depends strongly on diffusion coefficients. The spatially resolved model (with finite diffusion coefficients), being diffusion-limited, responds slower, and thus requires a higher activation rate in order to produce the same response as the bulk model (which assumes infinite diffusivities). Clearly, the issue of determining a consistent set of parameters is paramount.

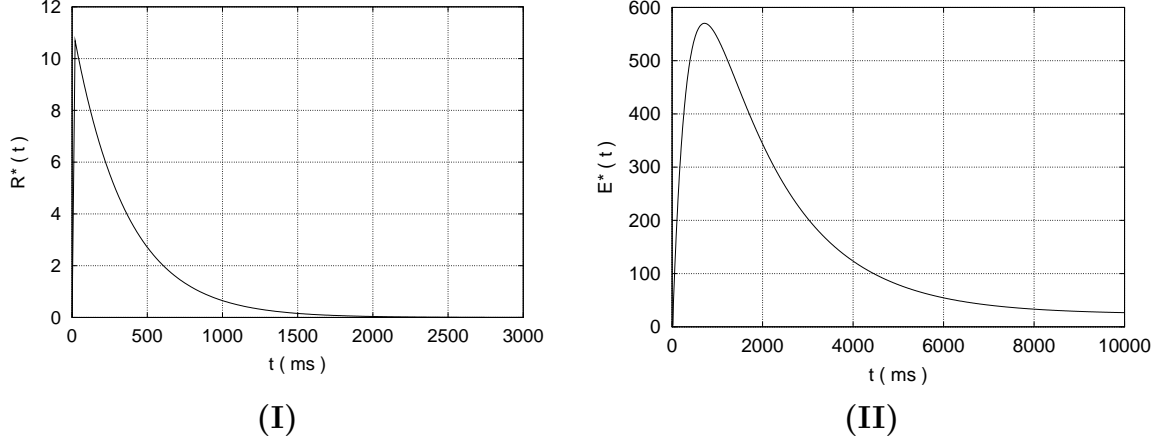


Figure 4.1: Activated rhodopsin and PDE molecules versus time. **(I)** $R^*(t)$ from (2.24a) and (2.25a). **(II)** $E^*(t)$ from (2.24b) and (2.25b).

4.1.4 Choice of Time and Space Scales

We noted in §3.3 that the number of computational time-steps for the problem is independent of the scalings. However, numerically some terms in the PDEs have very low sensitivity to some other terms, especially the w -flux from the lateral boundary in equation (2.14d). With the natural choice of rescalings, we confronted serious numerical problems of subtractive cancellations as illustrated in the following example.

Introducing the dimensionless variables- $u = \frac{[\text{cG}]}{\tilde{u}}$, $w = \frac{[\text{Ca}]}{\tilde{w}}$, $\rho = \frac{r}{\tilde{r}}$, $\tilde{u} = K_{\text{cG}}$, $\tilde{w} = K_{\text{ex}}$, and with arbitrary lengths (\tilde{r}, \tilde{z}) and time (\tilde{t}) scales, equation (2.14d) can be rewritten as

$$\begin{aligned}
 -D_{\text{Ca}} \frac{\tilde{w}}{\tilde{r}} \frac{\partial w}{\partial \rho} &= \frac{1}{\tilde{r} \tilde{z} \Sigma B_{\text{Ca}} \mathcal{F}} j_{\text{ex}}^{\text{sat}} \left(\frac{w}{1+w} \right) \\
 &\quad - \frac{\tilde{1}}{\tilde{r} \tilde{z} \Sigma B_{\text{Ca}} \mathcal{F}} \frac{1}{2} f_{\text{Ca}} j_{\text{cG}}^{\text{max}} \left(\frac{u^{m_{\text{cG}}}}{1+u^{m_{\text{cG}}}} \right), \quad (4.23)
 \end{aligned}$$

where $\Sigma = \frac{\Sigma_{\text{rod}}}{\tilde{r} \tilde{z}} = 2\pi \frac{R_{\text{rod}}}{\tilde{r}} \frac{H}{\tilde{z}}$ is the (dimensionless) lateral surface area of the outer rod segment. To make D_{Ca} dimensionless, we multiply both sides of (4.23) by $\tilde{t}/(\tilde{r} \tilde{w})$.

Thus

$$-\frac{\tilde{t}}{\tilde{r}^2} D_{\text{Ca}} \frac{\partial w}{\partial \rho} = \frac{\tilde{t}}{\tilde{r}^2 \tilde{z} \tilde{w} \Sigma B_{\text{Ca}} \mathcal{F}} \left[j_{\text{ex}}^{\text{sat}} \left(\frac{w}{1+w} \right) - \frac{1}{2} f_{\text{Ca}} j_{\text{cG}}^{\text{max}} \left(\frac{u^{m_{\text{cG}}}}{1+u^{m_{\text{cG}}}} \right) \right]. \quad (4.24)$$

Writing $\rho \rightarrow r$, $\frac{\tilde{t}}{\tilde{r}^2} D_{\text{Ca}} := D_{wr}$ = the radial diffusivity of [Ca], and $-D_{wr} \frac{\partial w}{\partial r} =: F_{wr}$ = r -component of the w -Flux, (4.24) takes the form

$$F_{wr} = C_{\text{ex}} [g_1(w) - C_{\text{ratio}} g_2(u)] \quad \text{on } \partial\Omega, \quad (4.25)$$

where

$$C_{\text{ex}} = \frac{10^{-9} \tilde{t}}{\tilde{r}^2 \tilde{z} \tilde{w} \Sigma B_{\text{Ca}} \mathcal{F}} j_{\text{ex}}^{\text{sat}}, \quad C_{\text{ratio}} = \frac{1}{2} f_{\text{Ca}} \frac{j_{\text{cG}}^{\text{max}}}{j_{\text{ex}}^{\text{sat}}}, \quad (4.26)$$

and all the symbols have their usual meanings. The numerical value 10^{-9} in C_{ex} results from unit conversions ($1 \text{ L} = 10^{15} \mu\text{m}^3$ and $1 \text{ pA} = 10^{-12} \text{ A} = 10^{-12} \text{ C s}^{-1}$).

The discretized version of (4.25) is of the form

$$w = w_0 + a_0 - b_0 \left(\frac{w}{1+w} \right), \quad (4.27)$$

where, for $i = I := I_p + I_f$, and $j = 1, \dots, N_{\text{disc}}(J_p + 2J_f)$,

$$w = W_{I+\frac{1}{2},j}^{n+1}, \quad (4.28)$$

$$w_0 = W_{I,j}^{n+1}, \quad (4.29)$$

$$a_0 = C_{\text{ex}} C_{\text{ratio}} (r_{I+1/2} - r_I) g_2(U_{I+\frac{1}{2},j}^{n+1}) / D_{wr}, \quad (4.30)$$

$$b_0 = C_{\text{ex}} (r_{I+1/2} - r_I) / D_{wr}. \quad (4.31)$$

With the natural scales $\tilde{r} = R_{\text{rod}}$, $\tilde{z} = H_i$ = height of a disc unit, $\tilde{t} = \tilde{z}^2/D$, where $D = \max(D_{\text{cG}}, D_{\text{Ca}})$ and the set of parameter values in Table 4.1, we get $a_0 \approx 10^{-18}$,

$b_0 \approx 10^{-18}$. Since $\frac{w}{1+w} \approx 1$, the term $a_0 - b_0 \left(\frac{w}{1+w} \right)$ in (4.27) is negligible compared to w_0 , resulting in $w \approx w_0$.

But this would mean no boundary update of the concentration of [Ca] and no effect of [cG] concentration in the diffusion (i.e., no coupling effect), which is completely against the physics of the problem on which the mathematical model is based. The effect of the term F_{wr} , the radial w -flux from the lateral boundary of the Rod, cannot be neglected for physical reasons. As such, we need to rescale the problem in some different way.

To overcome the subtractive cancellations as observed in (4.27), we choose the lengths and time scales so as to make the coefficient $C_{\text{ex}} = 1$. With this choice of scales, equation (2.14d) takes the form of (2.34c). The lengths and time scales for the different models discussed in §2.7 are listed below.

- Full Model

$$\begin{aligned} \Lambda_1 &= (10^{-9} \Sigma_{\text{rod}} \tilde{w} B_{\text{Ca}} \mathcal{F}) / j_{\text{ex}}^{\text{sat}}, \\ \tilde{r} &= A \times \Lambda_1, \quad \tilde{z} = B \times \Lambda_1, \quad \tilde{t} = \tilde{r} \times \Lambda_1. \end{aligned} \tag{4.32}$$

- Longitudinal Model

$$\begin{aligned} \Lambda_2 &= (10^{-9} V_{\text{cyto}} \tilde{w} B_{\text{Ca}} \mathcal{F}) / j_{\text{ex}}^{\text{sat}}, \\ \tilde{t} &= \Lambda_2, \quad \tilde{z} = (B \times \Lambda_2)^{\frac{1}{2}}. \end{aligned} \tag{4.33}$$

- Homogenized Model

$$\begin{aligned} \Lambda_3 &= (10^{-9} R_o \Sigma_{\text{disc}} \tilde{w} B_{\text{Ca}} \mathcal{F}) / j_{\text{ex}}^{\text{sat}}, \\ \tilde{t} &= \Lambda_3, \quad \tilde{r} = (A \times \Lambda_3)^{\frac{1}{2}}, \quad \tilde{z} = (B \times \Lambda_3)^{\frac{1}{2}}. \end{aligned} \tag{4.34}$$

A and B in (4.32) - (4.34) are any positive numbers. In our computation, we are using, typically, $A = B = 1000$. For the set of parameter values in Table 4.1, the numerical value of the constant C_{ratio} in (2.34c) is 35 and a_0 and b_0 from (4.27) become manageable.

4.2 Validation of the Models

In the next Chapter we present a simulation using the axisymmetric full model described in Chapter 2, as well as validation of the other computational models based on the bulk model, the one-dimensional longitudinal model, and the homogenized limit problem. Here we describe the setting and setup used in the simulations.

4.2.1 Experiment to be Simulated

Photoreceptors can respond to a wide range of light intensities, from a single photon to millions of photons. Work in [6, 7] was the first to identify responses to single photons in toad rods and measured 5% suppression of the dark circulating current.

The single photon response mechanism, on which we focus here, constitutes a fundamental building block of phototransduction. Experiments are difficult to carry out for very dim flashes and few experimental data exist in the literature concerning single photon response ([20, 6, 7, 26, 30, 18]), none of which is for salamander. On the other hand, **salamander** is the best studied rod outer segment, for which the most complete set of physiological parameters is available [44]. Even in this case, a consistent set of parameters has not been determined, a task to which mathematical models can contribute. Numerical simulations, as described here, can be used to test predictions resulting from a specific set of parameters against experimental data.

We present numerical simulations of phototransduction in vertebrate rod cells, specifically of the single photon response in a dark-adapted salamander rod outer segment, for which experimental data about the peak of the response were kindly provided to us by Fred Rieke (personal communication, Nov.2002).

4.2.2 Simulations

Visual transduction in vertebrate photoreceptors involves a diffusible internal transmitter which links photon absorption at disc membranes to a conductance decrease at the plasma membrane of the outer segment. We are primarily interested in the cellular response at the photoreceptor's plasma membrane, i.e., the reduction in current at the plasma membrane induced by light.

The numerical solution of the partial differential equations (2.33) - (2.34) gives the evolution of the spatial distribution of [cG] and [Ca] in the cytosol. The local circulating current $J(z, t)$ at any height z at any time t is obtained from (2.5) using the boundary values of [cG] and [Ca] at that z and t . The current $J(t)$ across the entire plasma membrane at time t is the mean value of $J(z, t)$ over Σ_{rod} . At $t = 0$, $J(z, 0) \equiv J(0) =: J_{\text{dark}}$, so both the local and total currents can be normalized by J_{dark} . Results are presented in terms of the response $J_{\text{dark}} - J$, and the normalized response $1 - J/J_{\text{dark}}$ for either local or total J .

To quantify the longitudinal spread, we count the number of discs for which response is more than 0.1% of the dark value. The reason for choosing such a low cutoff becomes apparent in view of the shape of the spatial z -profiles (Figs. 5.3, 5.4(I)) and it is further discussed in §5.3.

Chapter 5

Results and Discussion

5.1 Single Photon Response

Simulations were performed for a typical **salamander rod** photoreceptor rod with 800 discs. In the simulation reported here, out of 800 discs only the 400th disc is activated with a single photon ($\Phi = 1$ photoisomerization). The initial state is the dark steady-state determined in §4.1.2. For the PDE-activation step, the **lumped method** described in §2.5.2, §4.1.3 was employed. At desired intervals of time, values of the concentrations $[cG]$, $[Ca]$, and of total current $J = J_{cG} + J_{ex}$ at selected locations and profiles of concentration and current along the axial and radial directions are produced. Dark values are used for normalizations.

In the simulations (with the full model) reported here, we employ a fairly fine grid consisting of: 64 nodes in $[0, R_{disc}]$; 4 nodes in $[R_{disc}, R_{rod}]$ along the disc radius; 1 node below the disc, 2 nodes along the height of each disc, and 1 node above the disc. Thus, each disc unit is discretized into $64+4 \times 4+4 = 272$ control volumes, resulting in $272 \times 800 = 217600$ control volumes for the rod with $N_{disc} = 800$ discs.

We employ explicit-implicit time-stepping, with time-steps sufficiently small to ensure numerical stability of the scheme (see §3.3 for the CFL restriction). Computations were performed on the IBM pSeries cluster at Oak Ridge National Laboratory. A typical 1000 ms simulation of the Full Model for a rod with 800 discs, with such a grid using 21 processors, takes about 8 hours.

With the parameters of the model chosen as described in §4.1.1 and listed in Table 4.1, our simulations show that a single photoisomerization has considerable effect on both transversal and longitudinal diffusion of the second messengers cGMP and Ca^{2+} , and thus also on current.

We have verified, in the single photon case, that the location of activation site does not affect the suppression of total current nor the longitudinal spread of the current from the activation site, as long as the activated disc is not too close (~ 25 discs) to the end of the rod outer segment.

5.1.1 Results from the Full Model

Some of the important results obtained from the simulations for the single photon response from the Full model are shown in Figures 5.1 - 5.5 and are summarized below.

1. The peak amplitude of the response, $J_{\text{dark}} - J$, is about 0.53 pA, with $J_{\text{dark}} = 65.97$ pA, which amounts to 0.8% suppression in the dark standing current. It occurs at time 820 ms after light activation, see Fig. 5.1 (I).
2. The suppression of dark current results from depletion of cGMP and Ca^{2+} , see Fig. 5.2. [cG] depletes $\sim 10\%$ at time 760 ms, whereas [Ca] depletes more, $\sim 15\%$, but later, at 1020 ms.

3. Longitudinal profiles of normalized local response $1 - J(z)/J_{\text{dark}}$ are shown in Fig. 5.4 (I), with $J(z)$ the current at z . The maximal spread is ~ 172 discs at time 1000 ms; this amounts to a spread of $4.8 \mu\text{m}$, so 21.5% of the $22.4 \mu\text{m}$ rod length. After the start of recovery, the spread starts receding. Spread results reported in the literature for other species are discussed in §5.3.
4. The shapes of the cGMP z -profiles are almost identical to those of current, whereas the calcium z -profiles are more rounded, see Fig. 5.3 and Fig. 5.4 (I). [cG] spreads up to 150 discs ($\sim 4.2 \mu\text{m}$, .i.e., $\sim 19\%$ of the rod outer segment length) at time 1000 ms. [Ca] spreads up to 178 discs ($\sim 5 \mu\text{m}$, i.e., 22%).
5. The variation of the concentrations [cG] and [Ca] in the radial direction is shown in Fig. 5.5 and Fig. 5.4 (II). During activation, the radial profiles of [cG] become steeper with time, indicating that radial diffusion (especially below the activated disc) is not negligible, contrary to what has been assumed in several works ([18, 30, 22, 26, 44]). As recovery proceeds, the radial profiles regress and flatten out.
6. The radial profiles of [cG] in the cytosol just above and just below the activated disc are quite different in shape, Fig. 5.5, whereas those of [Ca] are identical, Fig. 5.4 (II). This is expected from the fact that cGMP is hydrolyzed by PDE* only on the lower surface of the activated disc, whereas Ca^{2+} does not interact with the discs.
7. Activating any single disc farther away than ~ 25 discs from the ends of the rod outer segment produces identical behavior (except, of course, with z -profiles shifted at the activation site).

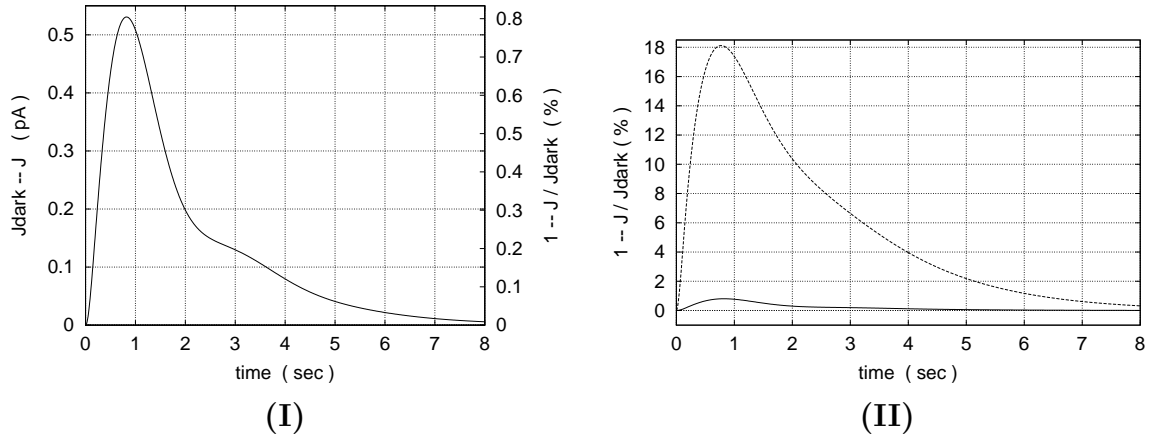


Figure 5.1: Single photon response from the full model: histories of response and normalized response. **(I)** Response $J_{\text{dark}} - J$ (left scale) and normalized response $1 - J/J_{\text{dark}}$ (right scale) versus time. The plot shows that the peak amplitude of response is 0.53 pA which amounts to 0.8% suppression in the dark standing current of 65.97 pA. The peak occurs at time 820 ms after activation. **(II)** Upper curve: local response at the activated (400th) disc unit only, normalized by J_{dark} . Lower curve: normalized response of the entire rod (same curve as in **(I)**, shown at larger scale for comparison). The maximum reduction in local current (across the surface of the plasma membrane corresponding to the activated disc unit) is 18% (occurring at time 820 ms), whereas in total current only 0.8% (at time 820 ms).

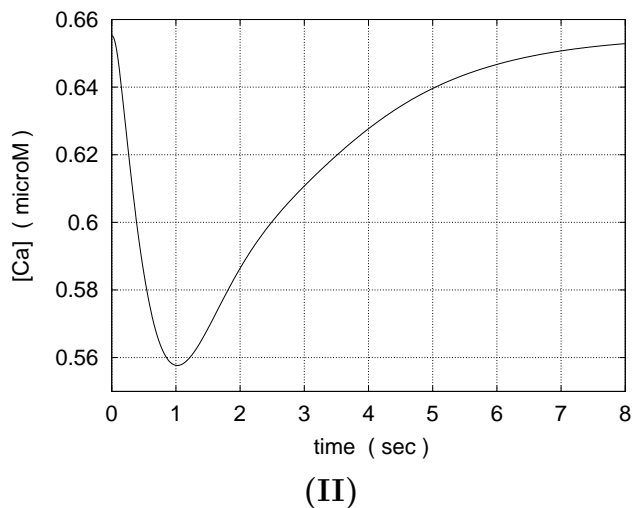
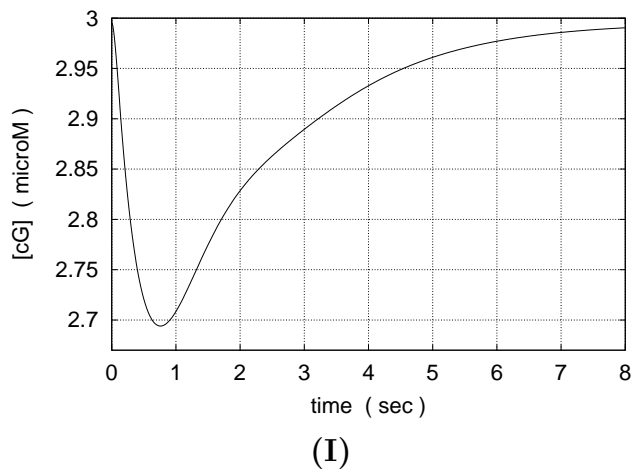


Figure 5.2: Single photon response from the full model: histories of concentrations of cGMP and Ca^{2+} at a fixed location in the cytosol in the vicinity of the activated disc. The initial concentrations $[\text{cG}]_{\text{dark}}$ and $[\text{Ca}]_{\text{dark}}$ are respectively 3 and $0.65 \mu\text{M}$. (I) $[\text{cG}]$ versus time. The cGMP concentration is depleted $\sim 11\%$ at time 760 ms. (II) $[\text{Ca}]$ versus time. The calcium concentration is depleted $\sim 15\%$ at time 1020 ms.

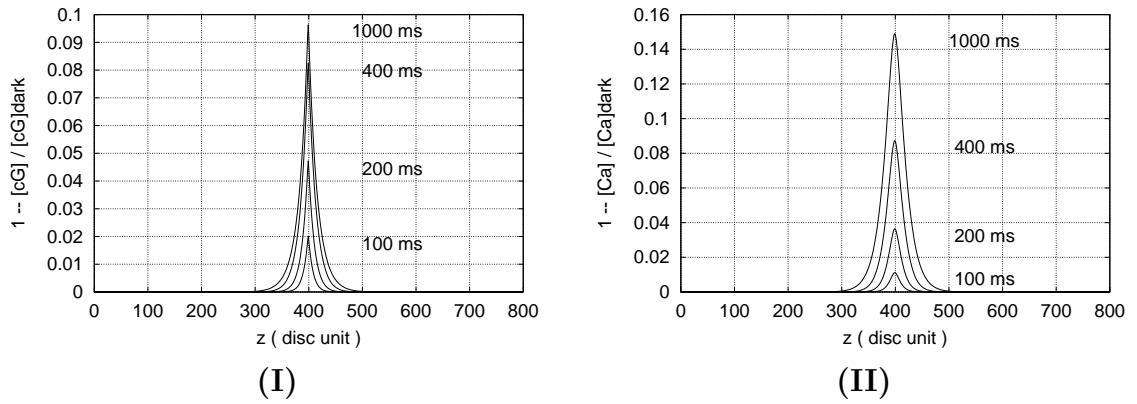


Figure 5.3: Single photon response from the full model: z -profiles of the depletion of relative concentrations at various times. The normalizing factors $[cG]_{\text{dark}}$ and $[Ca]_{\text{dark}}$ are respectively 3 and $0.65 \mu\text{M}$. **(I)** The depletion $1 - [cG]/[cG]_{\text{dark}}$ versus location z , at times 100, 200, 400 and 1000 ms. The maximal spread is ~ 150 disc units ($\sim 4.2 \mu\text{m}$), occurring at 1000 ms. **(II)** The depletion $1 - [Ca]/[Ca]_{\text{dark}}$ versus disc unit at times 100, 200, 400 and 1000 ms. The maximal spread is ~ 178 disc units ($\sim 5 \mu\text{m}$) occurring at 1000 ms. Calcium profiles are more rounded at their peaks.

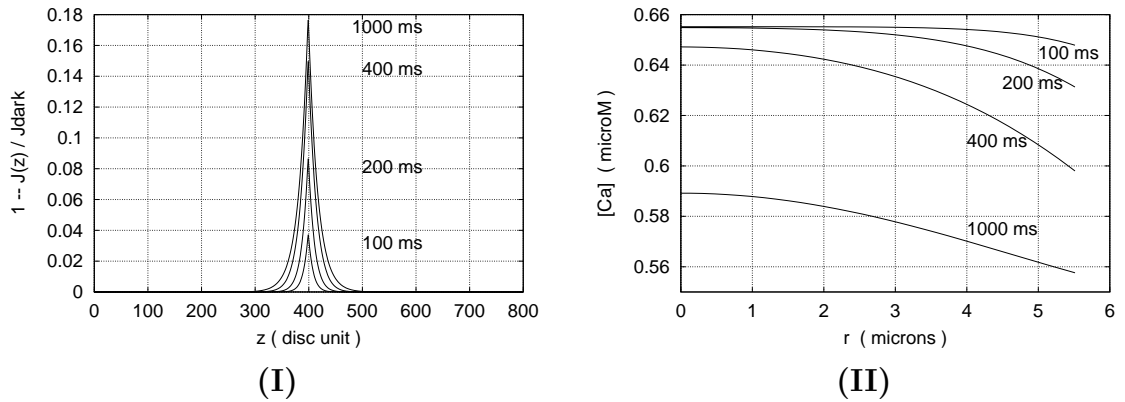


Figure 5.4: Single photon response from the full model: z -profiles of local relative response and r -profiles of Ca^{2+} concentration at various times. **(I)** Local relative response $1 - J(z)/J_{\text{dark}}$ versus disc unit at times 100, 200, 400 and 1000 ms. The normalizing dark current J_{dark} is 65.97 pA. The longitudinal spread of the response is about 172 disc units, which amounts to $4.8 \mu\text{m}$. **(II)** $[\text{Ca}]$ (μM) versus radial distance r (μm) at times 100, 200, 400 and 1000 ms (from top to bottom). The r -profiles of $[\text{Ca}]$ above and below the activated disc are identical.

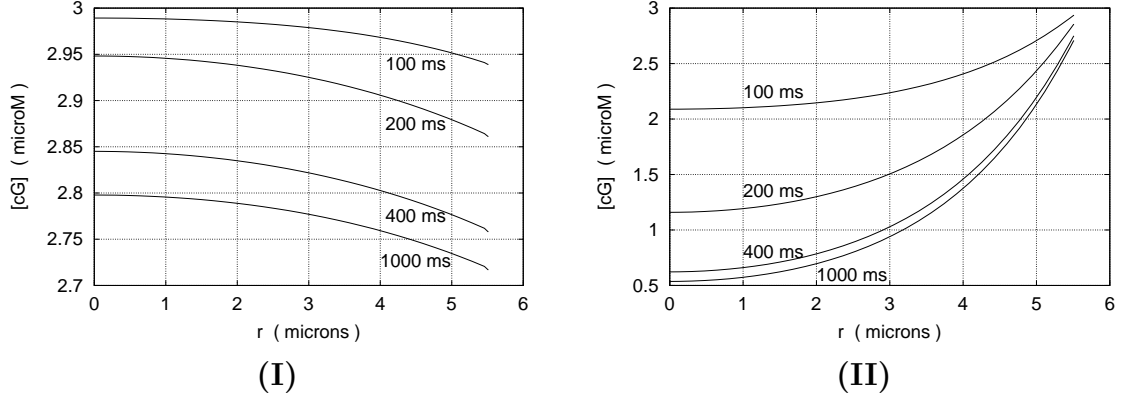


Figure 5.5: Single photon response from the full model: radial profiles of cGMP concentration: $[cG]$ (μM) versus r (μm) at times 100, 200, 400 and 1000 ms (from top to bottom). (I) Above the activated disc. (II) Below the activated disc. Note the difference in the vertical scales.

5.1.2 Results from Other Models

We also simulated the single photon response with the bulk, longitudinal and homogenized models (Chapter 2) on the same data set (Table 4.1) and activation (§??) as that of the full model. For the one-dimensional longitudinal model, we employed explicit-implicit time stepping. For the homogenized limit problem, we tried both explicit-implicit and fully implicit time stepping, on the schemes based on the partial differential equations and on the weak form.

Qualitatively, all the models gave very similar results, but quantitative results do not always agree. To get the same peak response from ordinary differential equation model, longitudinal model and the full model, the activation rate ν_{RE} needs to be adjusted, as discussed below. The various parameters for the ordinary differential equation model, longitudinal model and the full model need to be adjusted to get

identical results. This is to be expected, since the ordinary differential equation model assumes infinite diffusivities, the longitudinal is diffusion limited in the axial direction only, and the full model is fully diffusion limited.

Bulk Model

The bulk model (§2.5.2) simulation, shown in Fig. 5.6., produces almost twice as high a response as that from the full model. Lowering the activation rate ν_{RE} from 675 s^{-1} to 355 s^{-1} yields the 0.8% peak response of the full model.

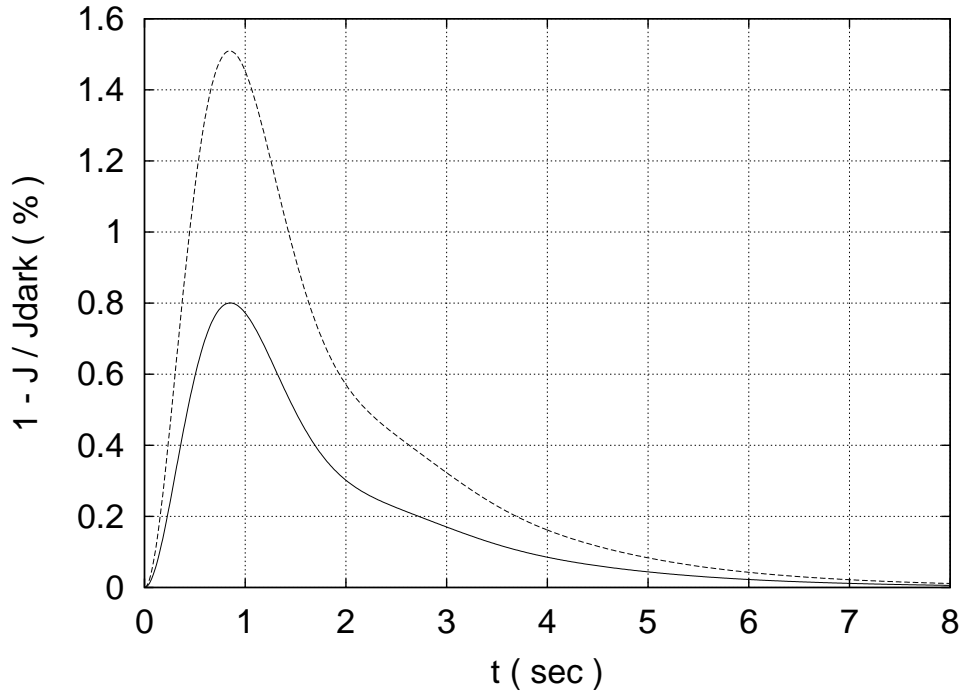


Figure 5.6: Bulk model simulation: normalized response versus time; upper curve with $\nu_{RE} = 675\text{ s}^{-1}$ and lower curve with $\nu_{RE} = 355\text{ s}^{-1}$.

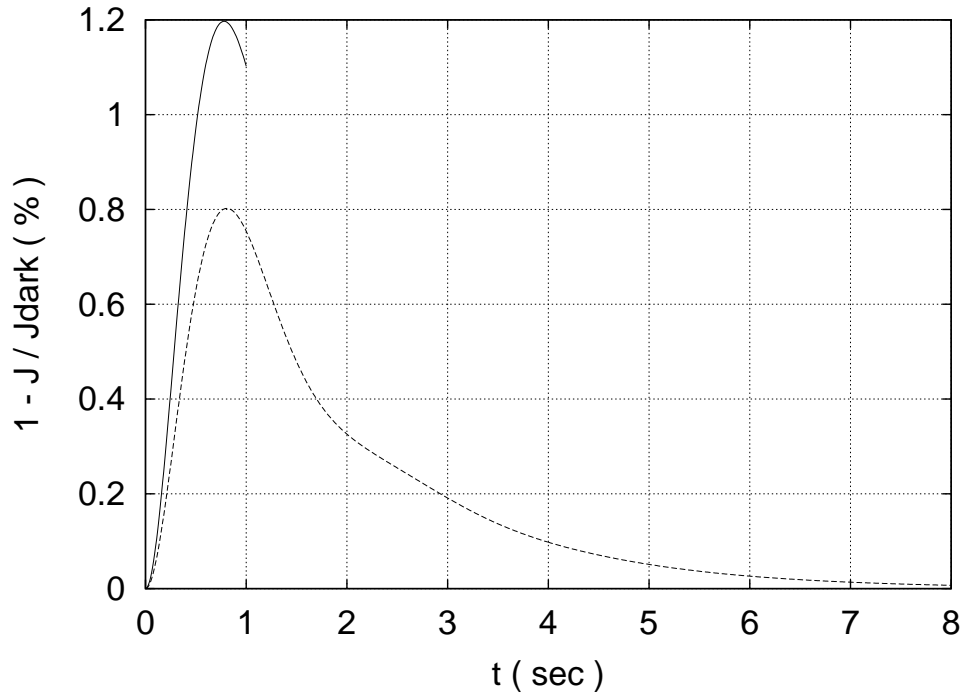


Figure 5.7: Longitudinal model simulation: normalized response versus time; upper curve with $\nu_{RE} = 675 s^{-1}$ and lower curve with $\nu_{RE} = 412.5 s^{-1}$.

One-dimensional Longitudinal Model

The results obtained from the one dimensional longitudinal model (§2.7.2) are presented in Fig. 5.7. When ν_{RE} from $675 s^{-1}$, the peak response is 1.2%, which drops to 0.8% with $412.5 s^{-1}$.

Homogenized Model

The results obtained from the weak form of the homogenized model (§2.7.4) are compared with the results of the full model in Fig. 5.8 and Fig. 5.9. There is fairly good agreement in both their response and spread. The schemes based on the

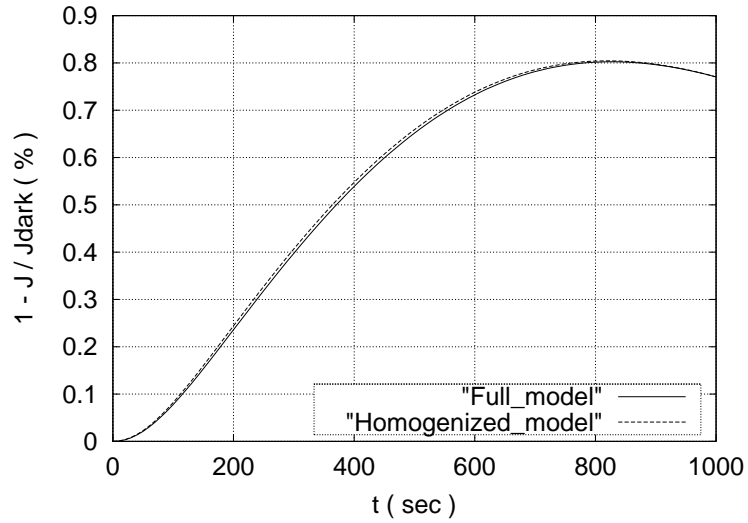


Figure 5.8: Normalized response from homogenized model and full model. The normalizing dark current J_{dark} is 65.97 pA.

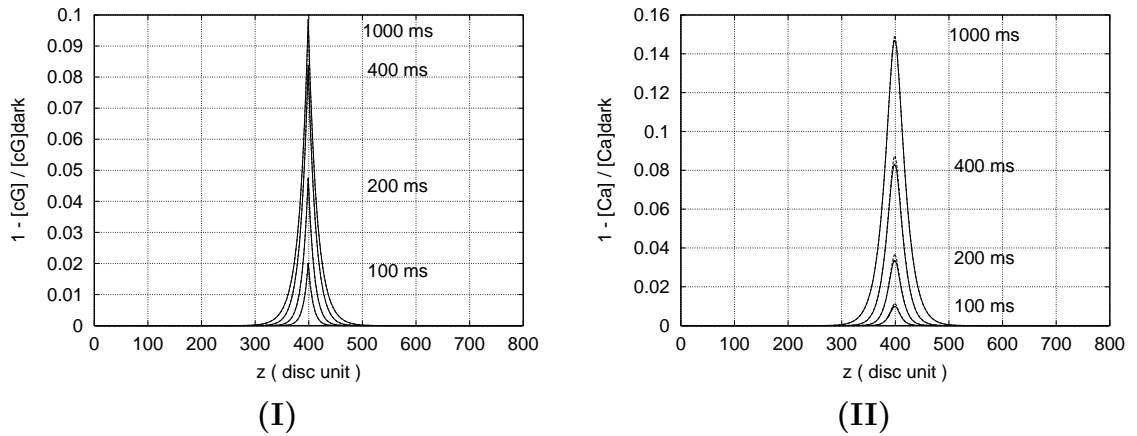


Figure 5.9: Longitudinal spread of cGMP and Ca^{2+} concentrations from homogenized model and full model, at times 100, 200, 400 and 1000 ms. dotted line: the homogenized model and solid line: the full model. **(I)** The depletion $1 - [\text{cG}]/[\text{cG}]_{\text{dark}}$ versus location z . **(II)** The depletion $1 - [\text{Ca}]/[\text{Ca}]_{\text{dark}}$ versus location z .

strong (partial differential equations) form of the homogenized model did not produce as agreeable results as from the weak scheme. Comparison of the results from all the models with adjusted activation parameter values are shown in Fig. 5.10, Fig. 5.11 and Fig. 5.12 .

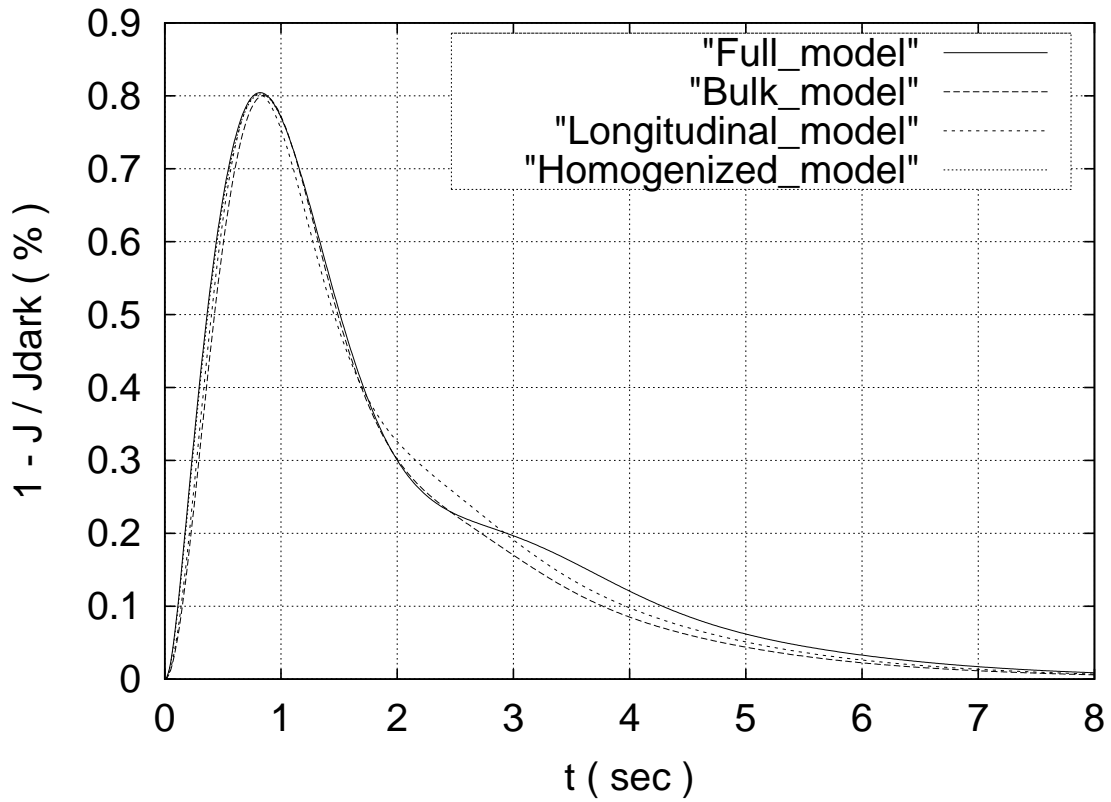


Figure 5.10: Histories of the normalized response from all models. The activation parameter $\nu_{RE} = 355 \text{ s}^{-1}$ in the bulk model, 412.5 s^{-1} in the longitudinal model and 675 s^{-1} in the full model and the homogenized model.

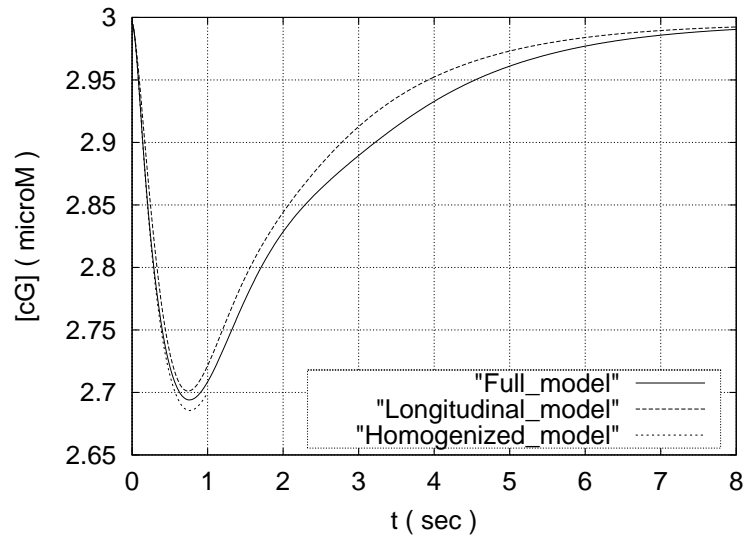


Figure 5.11: Histories of cGMP concentration (at activated disc) from all models. The activation parameter $\nu_{RE} = 355 \text{ s}^{-1}$ in the bulk model, 412.5 s^{-1} in the longitudinal model and 675 s^{-1} in the full model and the homogenized model.

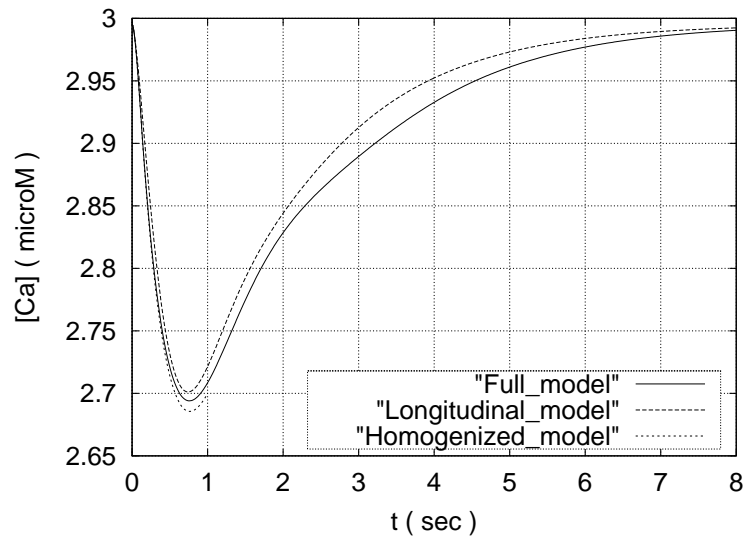


Figure 5.12: Histories of Ca^{2+} concentration (at activated disc) from all models. The activation parameter $\nu_{RE} = 355 \text{ s}^{-1}$ in the bulk model, 412.5 s^{-1} in the longitudinal model and 675 s^{-1} in the full model and the homogenized model.

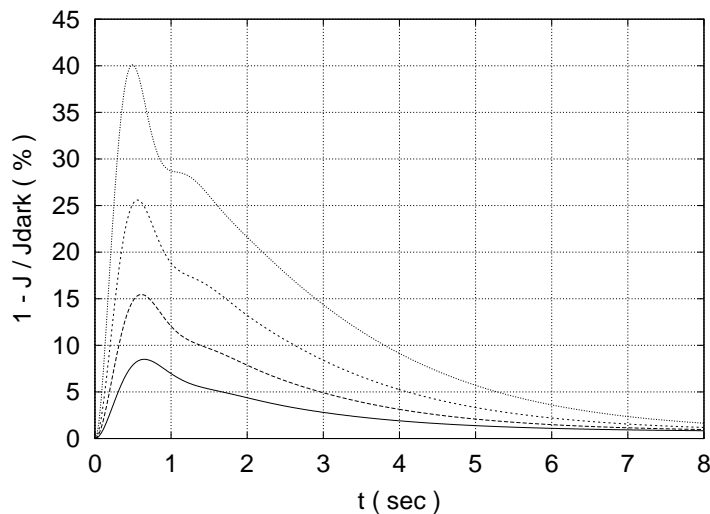


Figure 5.13: Bulk model simulations reproducing Fig. 10, p.234 of Pugh-Lamb [44]. Normalized response $1 - J/J_{\text{dark}}$ versus time for $\Phi = 11, 23, 45$ & 94 isomerizations.

5.2 Higher Intensity Stimulus

The results for higher intensity stimulus obtained from the bulk model described in §2.5.2 are presented in Fig. 5.13. The data for Fig. 5.13 are from [44, Fig. 9, p.229] ($R_{\text{disc}} = 5.485 \mu\text{m}$, $R_{\text{rod}} = 5.5 \mu\text{m}$, $\epsilon = 0.01375$, $\delta = 0.006875$, $\alpha_{\text{max}} = 40 \mu\text{Ms}^{-1}$, $\alpha_{\text{min}} = 0 \mu\text{Ms}^{-1}$, $B_{\text{Ca}} = 17.5$, $k_{\text{hyd}}^* = .428 \text{ molecules}^{-1} \mu\text{m}^3\text{s}^{-1}$, $k_E = 0.588 \text{ s}^{-1}$, $k_R = 2.857 \text{ s}^{-1}$, $\nu_{RE} = 220 \text{ s}^{-1}$). Fig. 5.14 and Fig. 5.15 show numerical simulations (with the full model) where we observe a change in the suppression of current with different arrangements of activation sites. Activating adjacent discs produces considerably lower response than activating discs far apart from each other. The simulation with $\Phi = 52$ photoisomerizations, activating seven discs (discs # 397 - 403) produces the peak response of only 5.5%, whereas activating (disc # 100, 200, 300, 400, 500, 600, 700) the peak response increases to 14.5%. This phenomenon is difficult to test experimentally, and we do not know its physical significance.

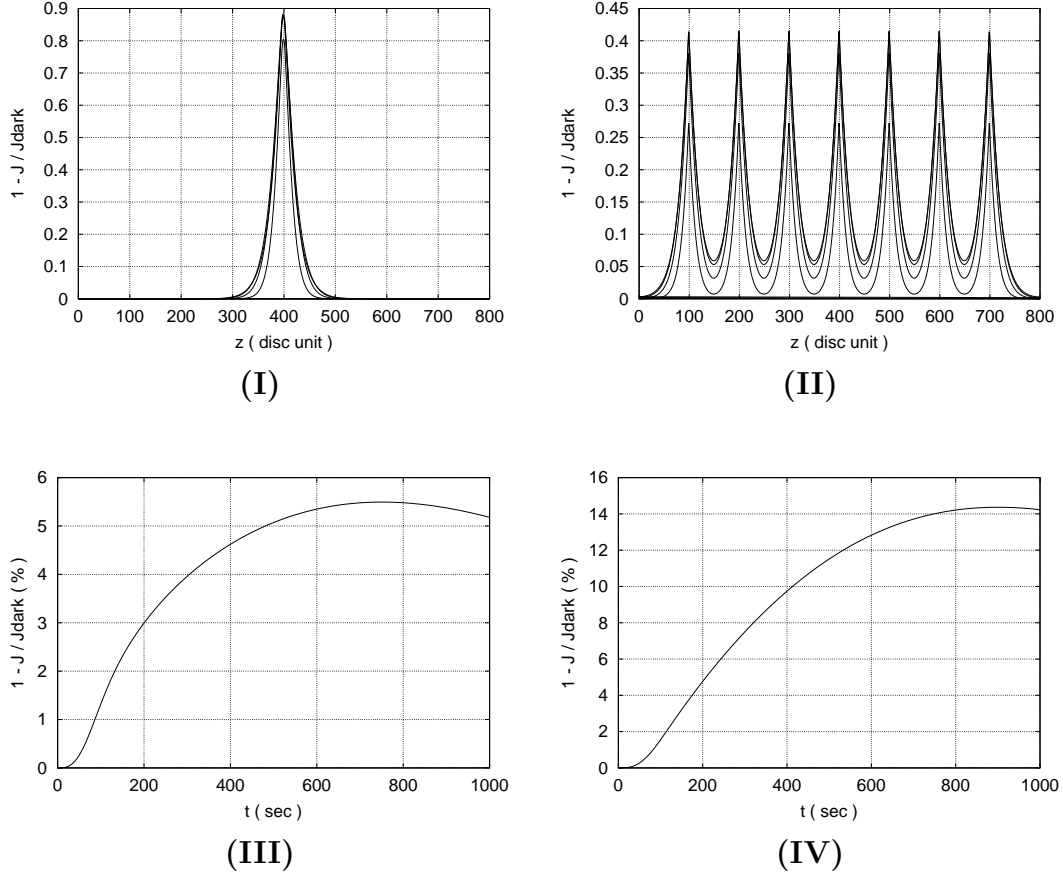


Figure 5.14: Longitudinal spread and histories of normalized responses with different arrangement of activation sites for $\Phi = 52$ photoisomerizations. Seven discs are activated: around the center of the rod (discs # 397 - 403) in **(I)** and **(III)**; 100 discs apart from each other (disc # 100, 200, 300, 400, 500, 600, 700) in **(II)** and **(IV)**. **(I)** & **(II)**: Longitudinal spread of (local) relative responses $1 - J(z)/J_{\text{dark}}$. **(III)** & **(IV)**: Normalized responses $1 - J/J_{\text{dark}}$ versus time. The suppression of the circulating current varies with the arrangements of the activated discs.

5.3 Conclusions

The only experimental data for single photon response in **salamander** rod, available to us were about the peak response from [45]. To match his $\sim 0.8\%$ reduction in standing dark current at ~ 800 ms, we adjusted certain activation parameters (see §4.1.3). All other parameters were chosen (see §4) consistent with [35, 44, 34] and listed in Table 4.1. With these parameters, we obtained 0.53 pA (0.8%) reduction at 800 ms of the 65.97 pA dark current.

The longitudinal spread of the response seems to vary considerably from species to species, see Table 5.1. The peak response of 0.53 pA we obtained for **salamander** rods is below the range 0.7 - 1.7 pA reported in [7, p. 631] for a single photon activation in **toad** rods. In that paper, 5% suppression of the (30 pA) dark current was measured. From this, it is somehow inferred ([26, 37]) that the change in [cG] effected by a single isomerization must spread longitudinally over at least the corresponding fractional length of the outer segment. In [26] it was deduced (from 1 pA peak reduction of 30 pA dark current) that each photoisomerization affects at least $1/30$ ($\sim 2 \mu\text{m}$ or 3%) of the **toad** rod. In Gecko gecko **lizard** rods, [18] obtained $7.6 \mu\text{m}$ spread which is 11% of the $70 \mu\text{m}$ rod length. In **rat** rods, [20] have estimated the spread of activation to be about $12 \mu\text{m}$, so 60% of the **rat** rod ($20 \mu\text{m}$ length).

Table 5.1: Spread of single photon response in various species

Species	ROS length (μm)	Spread (μm)	Spread (%)	Reference
lizard	70	7.6	11%	[18]
rat	12	60	20%	[20]
salamander	22.4	4.8	21.5%	this simulation
toad	60	2	3%	[6]

From the numerical simulation, we obtained $4.8\ \mu\text{m}$ longitudinal spread of the response in **salamander**, which amounts to 21.5% of ROS length ($22.4\ \mu\text{m}$). This spread appears to be much greater than that inferred by [26], [37] from Baylor’s experiment in **toad** rods and much smaller than that of [20] in **rat** rods. However, the spread results are not directly comparable, as they pertain to different animals, they are often indirectly deduced, and the notion of “spread” is vague and ill-defined. The cutoff we used for determining the maximal spread (0.001 of the dark value) is probably more strict than that of others, but realistic in view of the shape of the profiles. For example, a cutoff of 0.003 would produce $\sim 3\ \mu\text{m}$ spread, 22% narrower than from the 0.001 cutoff.

Since all the above mentioned results were obtained for different settings, it is not possible to compare them minutely. What we can conclude is that our simulation results also lie in the range of published literature values and show a good match to the general trend of the available experimental data. Given a set of parameters, our model can be used to determine the spatial and temporal variation of the concentrations of the second messengers cGMP and Ca^{2+} and of the resulting electrical response, providing detailed information that may be difficult to obtain experimentally. Thus, the simulations will be helpful for interpretation of available biological data, comparison of model predictions with measurements, determination of parameter values as well as sensitivity of output on various model parameters, and to design further biological experiments. The basic mechanisms of phototransduction are fundamentally similar to all other signal transduction by G protein coupled receptors encountered in olfaction and taste, hormonal signal transduction, chemotaxis and neurotransmitter signal transduction in brain. Computer simulations of the phototransduction will also provide experience needed to model multiple similar signal

transduction pathways that interact and cross-talk in cellular physiology.

5.4 Further Directions

With appropriate modifications, this model should be extendable to understand light and dark adaptation in rods, and a similar analysis should be possible on vertebrate cones which mediate color vision. In the future, we intend to develop computational models for transduction in cones and also to explore the coupling of cones and rods. We hope the model, after testing with various different species, may be very useful in developing a “virtual retina” which will help medical biologists to diagnose retinal degeneration diseases and other visual defects.

Bibliography

- [1] Alexiades, V. (2001) Lecture Notes on Numerical Methods for Conservation Laws. University of Tennessee, Knoxville.
- [2] Alikakos, N.D. (1981) Regularity and asymptotic behavior for the second order parabolic equation with nonlinear boundary conditions. *J. diff Eqns*, **39**, pp. 311-344.
- [3] Amann, H. (1988) Parabolic evolution equations and nonlinear boundary conditions. *J. diff Eqns*, **72**, pp. 201-269.
- [4] Andreucci, D., Bisegna, P., Caruso, G., Hamm, H.E. & DiBenedetto, E. (2003) Mathematical Model of the Spatio-Temporal Dynamics of Second Messengers in Visual Transduction. *Biophysical J.*, to appear.
- [5] Andreucci, D., Bisegna, P., & DiBenedetto, E., (2003) Homogenization and Concentrated Capacity for a Problem in Visual Transduction. *Annali di Mat. Pura et Appl.* to appear.
- [6] Baylor, D.A., Lamb, T.D. & Yau, K.-W. (1979a) The Membrane Current of Single Rod Outer Segments. *J. Physiol.*, **288**, pp. 589-611.
- [7] Baylor, D.A., Lamb, T.D. & Yau, K.-W. (1979b) Responses of Retinal Rods to Single Photons. *J. Physiol.*, **288**, pp. 613-634.
- [8] Baylor, D.A. (1996) How photons start vision, *Proc. Natl. Acad. Sci. USA*, **93**, pp. 560-565.
- [9] Bhalla, U.S. & Iyengar, R. (1999) Emergent Properties of Networks of Biological Signaling Pathways. *Science*, **283**, pp. 381-387.

- [10] Burns, M.C. & Baylor, D.A. (2001) Activation, deactivation, and adaptation in vertebrate photoreceptor cells. *Annual Rev. Neurosci.*, **24**, pp. 779-805.
- [11] Snir, M., Steve W., Steven, H., David, W., & Dongarra, J. (1996) MPI: The Complete Reference. The MIT Press.
- [12] Dongarra J. (2002) Lecture Notes and Slides on Scientific parallel Computing. University of Tennessee, Knoxville.
- [13] Eymard, R., Gaouet, T. & Herbin, R. (2000) *Finite Volume Methods*, Handbook for Numerical Analysis, Ph. Ciarlet J.L. Lions eds, North Holland, pp. 715-1022.
- [14] Eymard, R., Gaouet, T., Hilhorst, D. & Slimane, Y. (1999) Finite volumes and nonlinear diffusion equations.
- [15] Fain, G.L., Matthews H.R., Cornwall, M.C. & Kutalos, Y. (2001) Adaptation in Vertebrate Photoreceptors. *Physiol. Rev.*, vol. 81, No. 1, pp. 117-151.
- [16] Forti, S., Menini, A., Rispoli, G., & Torre, V. (1989) Kinetics of phototransduction in retinal rods of newt (*Triturus cristatus*). *J. Physiol. (Lond.)*, **419**, pp. 265 - 295.
- [17] Fosdick, L. & Jessup, E. (1995) An Overview of scientific Computing. High performance Scientific Computing, University of Colorado at Boulder.
- [18] Gray-Keller, M., Denk, W., Shraim, B., & Detwiler, P.B. (1999) Longitudinal Spread of Second Messenger Signals in Isolated Rod Outer Segments of Lizards. *J. Physiol.*, **519**, pp. 679-692.
- [19] Grossmann, ch. & Ross, H. -G. (1994) Numerik partieller Differentialgleichungen. B. G. Teubner Stuttgart.

- [20] Hagins, W.A., Penn, R.D. & Yoshikami, S. (1970) Dark current and Photocurrent in retinal rods. *J. Physiol.* **10**, pp. 380-412.
- [21] Halloy, C. & Wei, C. (March 19-20, 2003) Lecture Notes on Parallel Programming with MPI on the IBM SP System at ORNL. Joint Institute for Computational Science, ORNL.
- [22] Koutalos, Y., Nakatani, K., & Yau, K.-W. (1995) Cyclic GMP Diffusion Coefficient in Rod Photoreceptors Outer Segments. *Biophysical J.*, **68**, pp. 373-382.
- [23] Koutalos, Y., Nakatani, K. & Yau, K.-W. (1996) Regulation of Sensitivity in Vertebrate Rod Photoreceptors by Calcium. *TINS*, **19**, pp. 73-81.
- [24] Koutalos, Y. & Nakatani, K. (1999) Calcium Diffusion Coefficients in Rod Photoreceptors Outer Segments. *Biophysical J.*, **76**, A242.
- [25] Kurahashi, T. & Gold, G.H. (1990) Ionic Channels Mediating Sensory Transduction. In *Introduction to Cellular Signal transduction*, Birkhaeser, Boston, pp. 215-234.
- [26] Lamb, T.D., McNaughton, P. A. & Yau, K.-W. (1981) Spatial Spread of Activation and Background Desensitization in Toad Rod Outer Segment. *J. Physiol.*, **318**, pp. 463-496.
- [27] Lamb, T.D. & Pugh, E.N. (1992) A Quantitative Account of the Activation steps involved in Phototransduction in Amphibian Photoreceptors. *J. Physiol.* **449**, pp. 719-758.
- [28] Lamb, T.D. & Pugh, E.N. (1993) Amplification and Kinetics of the Activation Steps in Phototransduction. *Biochemica et Biophysica Acta*, **1141**, pp. 111-149.

- [29] Lamb, T.D. (1996) Gain and Kinetics of activation in the G-Protein cascade of phototransduction. *Proc. Natl. Acad. Sci. USA*, **93**, pp. 566-570.
- [30] Leskov, I.B., Klenchin, V.A., Handy, J.W., Whitelock, G.G., Govardovskii, V.I., Bownds, M.D., Lamb, T.D., Pugh, E.N. & Arshavsky, V.Y. (2000) The Gain of Rod Phototransduction: Reconciliation of Biochemical and Electrophysical Measurements. *Neuron*, **27**, pp. 525-537.
- [31] Liebman, P.A., Parker, K.R., Dratz, E.A. (1987) The molecular mechanism of visual excitation and its relation to the structure and composition of the rod outer segment. *Ann. Rev. Physiol.*, **49**, pp. 765-791.
- [32] Luskin, M. (1979) A Galerkin method for nonlinear parabolic equations with nonlinear boundary conditions. *Siam J. Numer. anal.*, Vol. 16, No. 2.
- [33] Nakatani, K., Chen, C. & Koutalos, Y. (2002) Calcium Diffusion Coefficient in Rod Photoreceptor Outer segments. *Biophysical J.*, **82**, pp. 728-739.
- [34] Nikonov, S., Engheta, N. & Pugh, E.N. Jr. (1998) Kinetics of Recovery of the Dark-adapted Salamander Rod Photoresponse. *J. Gen. Physiol.*, **111**, pp. 7-37.
- [35] Nikonov, S., Lamb, T.D. & Pugh, E.N. Jr. (2000) The Role of Steady Phosphodiesterase Activity in the Kinetics and Sensitivity of the Light-Adapted Salamander Rod Photoresponse. *J. Gen. Physiol.*, **116**, pp. 795-824.
- [36] Nikonov, S., Lamb, T.D., Pugh, E.N. Jr. (2001) Photoreceptor Sensitivity and Kinetics in Light Adaptation. *J. Gen. Physiol.*, **117**, pp. 365-366.

- [37] Olson, A. & Pugh, E.N. Jr. (1993) Diffusion coefficient of cyclic GMP in Salamander Rod outer segments estimated with two fluorescent probes. *Biophysical J.*, **65**, pp. 1335-1352.
- [38] Pao, C.V. (1981) Reaction Diffusion equations with nonlinear Boundary Conditions. *Nonlinear Analysis, Theory, Methods & Applications*, Vol. 5, No. 10, pp. 1077-1094.
- [39] Pao, C.V. (1992) *Nonlinear Parabolic and Elliptic Equations*. Plenum Press, New York.
- [40] Pao, C.V. (1990) Numerical Methods for coupled systems of nonlinear parabolic boundary-value problems. *J. Math. Anal. Appl.*, 151, pp. 581-608.
- [41] Pao, C.V. (1999) Numerical Analysis of coupled systems of Nonlinear Parabolic Equations. *Siam J. Numer. Anal.*, Vol. 36, No. 2, pp. 393-416.
- [42] Pawson, T. & Scott, J.D. (1997) Signaling through scaffold, anchoring, and adaptor proteins. *Science* **278**(5346), pp. 2075-80.
- [43] Press, W.H., Flannery, B.P., Teukolsky, S.A. & Vetterling, W.T. (1986) *Numerical Recipes*. Cambridge University Press.
- [44] Pugh, E.N. Jr. & Lamb, T.D. (2000) Phototransduction in Vertebrate Rods and Cones: Molecular Mechanisms of Amplification, Recovery and Light adaptation. In *Molecular Mechanism in Visual Transduction*, edited by D.G. Stavenga, W.J. Degrip & E.N. Pugh Jr, Elsevier, Amsterdam, pp. 183-255.
- [45] Rieke, F., Department of Physiology and Biophysics, University of Washington, Seattle Washington, *personal communication*.

- [46] Ronghua, Li., Zhongying, C. & Wei, W. (2000) Generalized Difference Methods for Differential Equations - Numerical Analysis of Finite Volume Methods. Marcel Decker, Inc.
- [47] Ruan, W. (1990) Bounded Solutions for Reaction-Diffusion Systems with Nonlinear Boundary Conditions. *Nonlinear Analysis, Theory, Methods & Applications*, Vol. 14, No. 12, pp. 1051-1077.
- [48] Schnapf, J.L. & Baylor, D.A. (1987) How Photoreceptor Cells Respond to Light. *Scientific American*, **256**, pp. 40-47.
- [49] Wald, G. (1968) The Molecular Basis of Visual Excitation. *Nature*, **219**, pp. 200-207.
- [50] Yang, T. (1999) Parallel Numerical Computations with Applications. Kluwer Academic Publishers.
- [51] Zhu, J. (1994) Solving partial differential equations in parallel computers. World Scientific, Singapur.

Vita

Harihar Khanal was born in Tansen, Palpa, Nepal on July 16, 1963. He obtained his first masters degree in Mathematics from Tribhuvan University, Nepal in 1989 and second masters degree in Industrial Mathematics from University of Kaiserslautern, Germany in 1996. Harihar Khanal married Tika Kumari Paudel in 1997. He was blessed with first son Tika Hari Khanal in 1998 and second son Prashant Khanal in 2000. He joined Tribhuwan University as an Assistant Professor in Mathematics in 1989 and was tennured in 1997. In August 1998, he entered The University of Tennessee, Knoxville to pursue the Doctorate of Philosophy in Mathematics. The doctoral degree was received in August 2003 under the supervision of Professor Vasilios Alexiades. He accepted a tennured track Assistant Professor position starting from August 2003 in the Department of Mathematics at Embry-Riddle Aeronautical University, Daytona Beach, Florida.